Optimization of resonant all-dielectric nanoparticles for optical manipulation and light management

Nils ODEBO LÄNK

Department of Physics
Chalmers University of Technology
Göteborg, Sweden, 2019

ii

OPTIMIZATION OF RESONANT ALL-DIELECTRIC NANOPARTICLES FOR OPTICAL MANIPULATION AND LIGHT MANAGEMENT
Nils ODEBO LÄNK

Division of Bionanophotonics
Department of Physics
Chalmers University of Technology
SE-412 96 Göteborg
Sweden
Telephone: +46 (0)31 - 772 10 00

Prevailing contact e-mail: nils.odebo.lank@gmail.com

Cover:
(Top-left) Silicon metasurface that exhibits near perfect absorption in a total internal reflection geometry. (Top-right) Silicon metasurface on a mirror. The reflection from the metasurface destructively interferes with the reflection from the mirror, enabling enhanced absorption. (Bottom-left) A quasi porous silicon nanoparticle, illustrating the enhanced near-fields in the pores. (Bottom-right) Illustration of a focused laser beam able to confine a silicon particle in 3D with optical forces.

CHALMERS UNIVERSITY OF TECHNOLOGY

Optimization of resonant all-dielectric nanoparticles for optical manipulation and light management
Nils ODEBO LÄNK

Department of Physics

Thesis for the degree of Doctor of Philosophy

Abstract

The resonant interaction between light and matter lies at the heart of nanophotonics research. In particular, nanoparticles that possess optical resonances in the visible spectral range have been avidly studied and employed for various technical and biological applications in the last two decades.

While the most commonly employed nanoparticles are metallic ones with localized plasmonic resonances, these particles suffer from inevitable optical losses and parasitic photothermal heating.

Recently, through the advent of new fabrication techniques, all-dielectric nanoparticles with high refractive index have arisen as a competitive alternative both as colloidal nanoparticles and as building blocks in metasurfaces. These particles present low-loss geometric resonances of electric and magnetic character with Q-factors comparable to plasmonic nanoparticles. Importantly, the various multipolar responses excited in these particles can be engineered to interact and give rise to highly directional scattering or light confinement.

This thesis focuses on the design, modelling and optimization of resonant all-dielectric nanoparticles for nanophotonic applications through electrodynamics simulations such as finite-difference time-domain and various analytical or semi-analytical models.

It is demonstrated that highly specific design of metasurfaces with silicon nanoantennas can yield close to 100% optical absorption at specific light wavelengths. The effect is a result of complete destructive interference between different multipolar excitations and can be achieved despite the low intrinsic losses of silicon.

Further, this effect is exploited to propose a novel solar harvesting device using nanostructured amorphous silicon with theoretically predicted efficiencies that approach state-of-the-art thin film solar cells.

Owing to their significant interaction with light and generally low losses, resonant all-dielectric particles are promising candidates for nanoscopic handles in biological systems. This thesis therefore focuses partly on optical forces and manipulation of silicon nanoparticles. The zero-backscattering Kerker condition is investigated as an avenue to decrease radiation pressure in an optical trap. Moreover, a comparison to more conventional nanoparticle materials for optical tweezers such as gold and polystyrene is made, including photothermal effects.

Lastly, the interaction of porous silicon nanoantennas with subwavelength emitters or absorbers is studied and the influence of porosity, pore size, and pore placement is elucidated.

KEYWORDS: silicon; nanophotonics; all-dielectric; metasurfaces; optical forces; perfect absorption; FDTD

List of publications

The thesis is based on the work presented in the following papers:

I **Large-scale silicon nanophotonic metasurfaces with polarization independent near perfect absorption**
Nils Odebo Länk, Ruggero Verre, Peter Johansson & Mikael Käll
Nano Letters **17** (5), 3054 – 3060 (2017).

II **Metasurfaces and colloidal suspensions composed of 3D chiral Si nanoresonators**
Ruggero Verre, Lei Shao, Nils Odebo Länk, Pawel Karpinski, Andrew B. Yankovich, Tomasz J. Antosiewicz, Eva Olsson & Mikael Käll
Advanced materials **29**, 1701352 (2017).

III **Directional scattering and multipolar contributions to optical forces on silicon nanoparticles in focused laser beams**
Nils Odebo Länk, Peter Johansson & Mikael Käll
Optics Express **26** (22), 29074 – 29085 (2018).

IV **Electromagnetic energy distribution in resonant quasi porous silicon nanostructures**
Nils Odebo Länk, Mikael Käll & Tomasz J. Antosiewicz
Submitted manuscript

V **Solar harvesting based on all-dielectric perfect absorbing metasurfaces**
Robin Vismara, Nils Odebo Länk, Ruggero Verre, Mikael Käll, Olindo Isabella & Miro Zeman
Submitted manuscript

VI **Thermal effects and trap stability for nanoparticle spheres in an optical trap**
Nils Odebo Länk, Peter Johansson & Mikael Käll
In manuscript

Declaration of author contributions

I   I performed the optical experiments, the simulations and developed the analytical model. I also wrote the first draft of the paper.

II   I performed the electrodynamics simulations, participated in the interpretation of data and participated in writing the paper.

III   I made all calculations, simulations and data analysis and wrote the first draft of the paper.

IV   I designed and performed all simulations and data analysis and wrote the first draft of the paper.

V   I performed the simulations of the idealized array as well as the multipole decompositions. I also wrote the first draft of the paper together with Robin Vismara.

VI   I performed the optical force simulations, the data analysis and wrote the first draft of the paper.

Additional papers, not included in the thesis

The following papers were produced during the thesis period:

VII   **Directional light extinction and emission in a metasurface of tilted plasmonic nanopillars**
Ruggero Verre, Mikael Svedendahl, Nils Odebo Länk,
Zhong-Jian Yang, Gülis Zengin, Tomasz J. Antosiewicz
& Mikael Käll
Nano Letters **16** (1), 98 – 104 (2015).

VIII   **Polarization conversion-based molecular sensing using anisotropic plasmonic metasurfaces**
Ruggero Verre, Nicolò Maccaferri, Karsten Fleischer,
Mikael Svedendahl, Nils Odebo Länk, Alexandre Dmitriev
Paolo Vavassori, Igor V. Shvets & Mikael Käll
Nanoscale **8** (20), 10576 – 10581 (2016).

IX   **Probing photothermal effects on optically trapped gold nanorods by simultaneous plasmon spectroscopy and Brownian dynamics analysis**
Daniel Andrén, Lei Shao, Nils Odebo Länk, Srdjan S. Aćimović,
Peter Johansson & Mikael Käll
ACS Nano **11** (10), 10053 – 10061 (2017).

X   **Photothermal DNA release from laser-tweezed individual gold nanomotors driven by photon angular momentum**
Hana Šípová, Lei Shao, Nils Odebo Länk,
Daniel Andrén & Mikael Käll
ACS Photonics **5** (6), 2168 – 2175 (2018).

XI   **Antenna-enhanced fluorescence correlation spectroscopy resolves calcium-mediated lipid–lipid interactions**
Stephan Block, Srdjan S. Aćimović, Nils Odebo Länk,
Mikael Käll & Fredrik Höök
ACS Nano **12** (4), 3272 – 3279 (2018).

XII   **Large-scale fabrication of shaped high index dielectric nanoparticles on a substrate and in solution**
Ruggero Verre, Nils Odebo Länk, Daniel Andén
Hana Šípová & Mikael Käll
Advanced Optical Materials **6** (7), 1701253 (2018).

XIII   **Surface interactions of gold nanoparticles optically trapped against an interface**
Daniel Andrén, Nils Odebo Länk, Hana Šípová-Jungová,
Steven Jones, Peter Johansson & Mikael Käll
Submitted manuscript

$\hookrightarrow$

Acknowledgements

I would first like to acknowledge the extensive support of my supervisor Professor Mikael Käll. For the opportunity to even be here and the guidance throughout my stay. Specifically, for always keeping your door open and for being patient and pedagogical.

Thank you immensely to my co-supervisor Professor Peter Johansson, for the great theoretical support. It seems that whatever the question is, you have some notes and/or some Fortran code on the subject. Your extensive knowledge and your way of seeing things has influenced me. Thank you for always taking the time to answer my questions.

Ruggero Verre, for the huge support in our shared projects. It is easy to get swept away with your enthusiasm and grand visions. I tend to get stuck on details, and your ability to see the bigger picture has been very helpful. Moreover, you have always been positive and energetic and I really appreciate that.

Tomasz Antosiewicz, not only have you helped me through our shared project, you have always been extremely helpful to me in my other projects. Specifically, you were always willing to share your enormous expertise of the FDTD method. For all your help, support and very pleasant conversations I am very thankful!

I'm grateful also to our co-authors on the scientific projects! In particular to Robin Vismara and Olindo Isabella in Delft as well as Andy and Eva Olsson for fruitful collaborations.

Thank you to Peter Apell, for offering your support throughout my time here.

Special thanks go also to Daniel Andrén, with whom I have had extensive conversations about the life of a PhD student in Bionanophotonics.

Thanks to my office mate, Denis Baranov, for many excellent discussions and valuable input on my various undertakings.

My thanks go also to the rest of the Bionanophotonics division, both past and current! Specifically, Mikael S, Zhong-Jian and Lei, for the valuable help when I started out. And for being encouraging and making the workplace pleasant, thank you Timur, Martin, Steven, Robin, Hana, Jade, Benjamin, Srdjan, Pawel, Ankit, Battulga, Luis, Tom, Aili, Partha, Nermin, Jorge, Andreas, Michael, Adriana, Noemi, Yang, Gustav E.J., Gustav E, Kunli, Yurui, Kristof, and Gülis.

Finally, my sincerest thanks to my lovely Josefin as well as the rest of my family and friends, who have always supported me and believed in me throughout my studies. It has been a great help to know that I always have you. I promise that you will see more of me now that I'm done writing this!

Nils ODEBO LÄNK
Göteborg, April 2019

Contents

Chapter 1

Introduction to dielectric nano-optics

The interaction between light and matter is one of the most important and ubiquitous concepts throughout the natural world. Understanding and taming this interaction in various ways has led to some of the most important milestones in human development and technology.

What we typically call "light" in our everyday lives is electromagnetic radiation within a quite narrow frequency range. Radio waves and microwaves are examples of the same type of radiation but at lower frequency, while X-rays and gamma radiation are examples with higher frequency. So the importance of light-matter interactions stretches all the way from long-range communication using radio antennas to understanding how gamma radiation affects our bodies and why it can be harmful. Indeed, the reason that the particular wavelength range of $\lambda \approx 400 - 750$ nanometers (nm) is called the *visible* wavelength range is likely (at least partly) due to the interaction between light and a very special example of matter – water. At both sides of the visible spectrum, ultraviolet and infrared, water absorbs light very effectively. Since our atmosphere contains vast amounts of water, there wouldn't be much light around to see for an eye sensitive to infrared or ultraviolet light! So from a certain point of view, through evolution, we used the concepts of light-matter interaction to our advantage before we were advanced enough to know it.

As a light wave travels through space, the electromagnetic field oscillates and varies over a wavelength, λ. It is interesting to compare this *length* with a characteristic size, d, of matter the light interacts with. For atoms, d is around 10^{-10} m or 0.1 nm, which is much smaller than λ for visible light. Meanwhile, for something like bacteria which we typically consider very small in our everyday lives we have $d \approx 10^{-6}$ m or 1000 nm which is larger but comparable to λ. It is between these two sizes that this thesis takes place, visible and near-infrared light interacting with matter with characteristic sizes $d \approx 10 - 500$ nm. This is the realm of nano-optics.

The most interesting and useful phenomena arise when there is a strong interaction between light and matter, when the nanoparticle has a strong optical response. Such high optical response can be achieved when the incident light has a frequency that lies in the vicinity of an optical resonance in the particle.

Recent advances in nanotechnology and nanofabrication have allowed for the realization of tailor-made structures at the nanoscale. Through this, it has become possible to experimentally study, characterize and harness the power of resonant nanoparticles.

This thesis focuses on the properties of resonant particles made of all-dielectric materials. These particles are studied both in isolation and as part of more complex arrangements. In order to arrive to where this thesis takes place, we first embark on a brief journey through the history of nano-optics.

1.1   Metamaterials and metasurfaces

Visible light interacting with nanoparticles is in a sense analogous to radio waves interacting with antennas. Specifically, the function of an antenna is to convert propagating waves from afar into localized electric signals that can be transmitted through wires or vice-versa. In certain contexts, resonant nanoparticles are therefore referred to as "optical antennas" [1, 2]. They are able to convert visible light into enhanced near-fields as well as transmit information about local properties into the far-field.

Continuing the analogy with radio waves, it is a common practice to combine several antenna elements into an antenna array. This gives great control of the shape of the radiation pattern and one can aim the emission or reception in a specific direction. Deliberate assembly of nanoparticles into different patterns has become the focus of considerable recent research. Through various nanofabrication techniques such as electron beam lithography or colloidal lithography [3], it is possible to assemble many nanoparticles smaller than the wavelength of visible light into a desired pattern. If the inter-particle distances are also subwavelength, the resulting assembly is referred to as a "metasurface", a two-dimensional analogue of a metamaterial.

Research interest for metamaterials started in earnest around 20 years ago, with Pendry's seminal paper on perfect lensing [4]. A perfect lens, along with many other exotic optical effects, requires a material with a negative refractive index, something that is not found in any naturally occuring materials. Instead, these *meta*-materials arose with the objective to effectively introduce both a negative magnetic permeability ($\mu < 0$) and a negative electric permittivity ($\varepsilon < 0$) through an artificial magnetic response. One of the first examples was in the microwave regime with Split-Ring Resonators (SRRs) [5] which utilized a resonant effective magnetic response combined with conducting wires providing the negative ε [6].

Metamaterials and metasurfaces have since then evolved and moved from the microwave regime toward the visible frequency range. However, a smaller wavelength requires smaller elements and the fabrication is considerably more difficult at the nanoscale. Moreover, at these shorter wavelengths, the optical response of many materials is different since the energies are routinely enough to excite electronic transitions.

More recent applications and properties of metasurfaces, specifically in the visible spectral range, will be discussed further on as part of the discussion on the materials typically employed in their construction.

1.2   Plasmonics

A plasmonic excitation is an oscillation of the free conduction electrons in a metal. One typically distinguishes between different kinds of plasmonic excitation: bulk plasmons, surface plasmon polaritons (SPP) and localized surface plasmon resonances (LSPR). The SPP is a propagating charge oscillation that moves along the interface between a dielectric material and a metal, while the LSPR is confined on the surface of a metallic nanoparticle.

Nanoparticles with LSP resonances in the visible or infrared spectral range essentially act as optical antennas, in the sense that they are able to confine the radiation into subwavelength regions [1]. Due to reciprocity, this naturally also works

in reverse, the optical antenna can transmit information about its immediate sub-wavelength environment. These functionalities offer a plethora opportunities to engineer light-matter interactions at the nanoscale, and the field of plasmonics has been a very active area of research for the last few decades [7–10].

Localized surface plasmons couple extremely well to light. In fact, their interaction cross sections (scattering and absorption) can greatly exceed their geometrical cross sections. Moreover, the spectral location of these resonances is greatly dependent on their specific geometric shape and size of the nanoparticles [11] as well as the properties of their immediate surroundings. The spectral location of the resonance naturally affects the colour of the scattered light and colloidal solutions of noble metal nanoparticles typically have beautiful and vibrant colours, something that was utilized in the making stained glass windows for medieval churches. The sensitivity of the resonance to the particle surroundings has found applications in sensing based on refractive index changes [12–15]. The enhanced near-fields can give rise to Surface-Enhanced Raman Scattering (SERS) even down to the single molecule detection limit [16, 17] as well as improved solar cells, a review of which can be found in Ref. [18].

Owing to the strong optical response, enhanced near-fields and sensitivity to their proximity, plasmonic nanoparticles have been extensively employed in the design of metasurfaces. Examples include advanced light management techniques such as focusing [19], bending [20] and polarization control [21, 22] as well as optical holography [23]. Other than directly altering the properties of light, plasmonic metasurfaces offer great opportunities in sensing of refractive index changes [24] or using Surface-enhanced Raman Spectroscopy [25]. This brief introduction naturally only brushes the surface of this mature and still active research field. Many prominent researchers in the field recently contributed to an in-depth review and roadmap of modern plasmonics [10].

1.3 High refractive index dielectric nanoparticles

The concept of using optically small particles with high refractive index also arose in the context of metamaterials with negative effective material parameters, $\mu_{\text{eff}}, \varepsilon_{\text{eff}} < 0$ [26–28]. Again, some of the first experimental examples came for applications with frequencies in the GHz range [29]. The interest was sparked because particles with high refractive index exhibit a resonant response of both electric and magnetic character, something that was described in the early 1900s by Mie [30]. Moreover, that an effective magnetic material response could be obtained through embedding such particles in a host matrix was known already in the middle of the last century [31]. However, with the contemporary interest for metamaterials with negative optical parameters, the topic experienced a resurgence. Following immense progress in nanofabrication, the concept moved upwards in frequency around a decade ago, via the infrared [32], to when the first experimental demonstrations appeared in the visible spectral range appeared around 2012 [33].

It was realized with the help of Mie theory that certain semiconductor materials, and in particular silicon, have a refractive index high enough for this strong magnetic response to appear in the visible and near-infrared [34, 35]. The scattering properties of crystalline silicon spheres calculated with Mie theory is shown in Figure 1.1 (see Chapter 2 for a detailed discussion on the Mie solution and how these results were calculated).
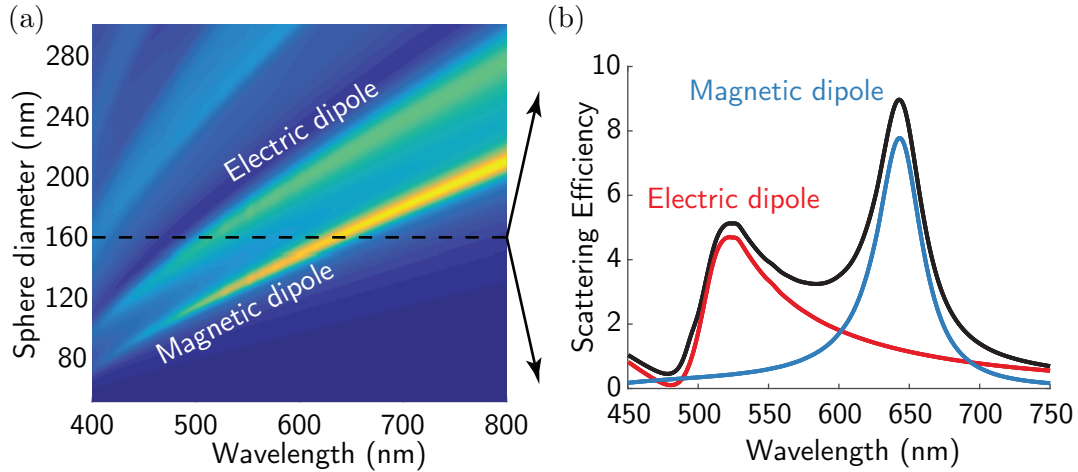
FIGURE 1.1: **Optical response of silicon nanospheres. (a)** The scattering efficiency of silicon spheres in the visible spectral range as a function of sphere diameter, showing the spectrally tunable electric and magnetic dipole response. **(b)** Scattering spectrum for a selected silicon sphere with diameter $D = 160$ nm

The localized plasmonic resonances discussed earlier are a consequence of the restoring forces experienced by the conduction electrons in the metal. In contrast, these Mie resonances in high index dielectric particles should be thought of as geometric in nature. An analogy can be made with a Fabry-Perót cavity where an eigenmode appears when the light wavelength is some multiple of the optical path length in the cavity. Similarly, the lowest order Mie resonance, the magnetic dipole, occurs approximately when the condition $\lambda_0/n \approx D$ is fulfilled, where λ_0 is the light wavelength in vacuum, n is the refractive index of the particle and D is its diameter. The refractive index of silicon in the visible wavelength range is around $n = 3.5 - 4$ [36], which puts the lowest order resonances at particle diameters around 4 times smaller than the wavelength. The magnetic dipole has its origin in circulating displacement currents that get excited in the particle, resembling a magnetic dipole current source. Importantly, by appropriately choosing the size of the nanoparticle, one can thus tune the spectral position of the electric and magnetic response for a specific application.

Besides nanospheres, the most studied geometric shape of resonant high-index nanoantennas is cylindrical disks. For practical applications, this is probably the design that is most commonly employed. Especially in the design of metasurfaces, the relative ease in fabricating nanodisks lithographically makes them an attractive choice. From the perspective of optical characterization, however, nanodisks present a larger challenge due to the absence of an exact analytical solution to the scattering problem, such as Mie theory for spheres. Instead, numerical approaches such as finite-difference time-domain (FDTD) (Chapter 3) need to be used. Compared to plasmonic resonators however, these geometrical resonances are much less sensitive to the exact geometric shape of the nanoparticle and much of the understanding from the spherical particles can transferred to nanodisks.

The optical response for silicon nanodisks calculated with FDTD are shown in Figure 1.2. The disks are illuminated with an x-polarized plane wave along z. One of the most important contrasts is that for spherical particles, the electric and magnetic dipoles are always spectrally separated. However, their relative spectral position can be tuned by changing the aspect ratio of a nanodisk [37] or spheroid [38]
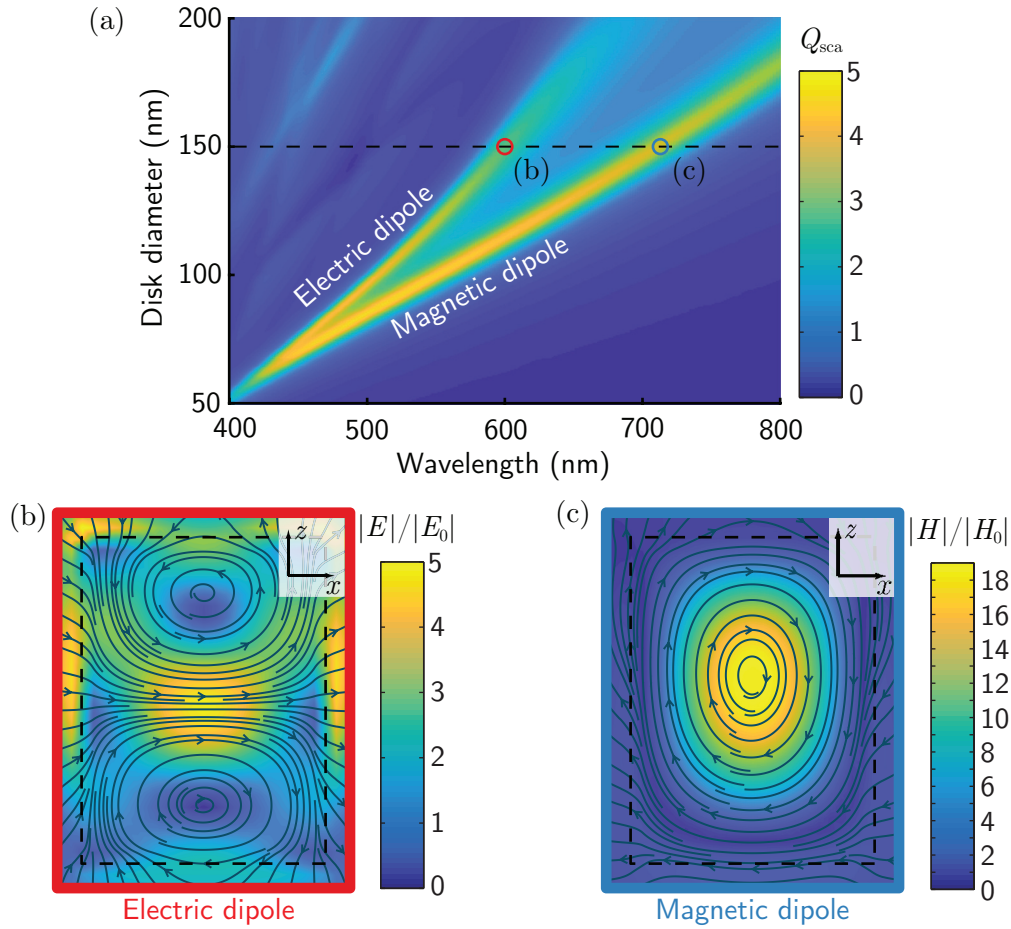
FIGURE 1.2: **Optical response and near-fields for silicon nanopil-
lars illuminated from the bottom with x-polarized light. (a)** The
scattering efficiency of silicon pillars with a constant height $h = 200$
nm as a function of disk diameter. **(b), (c)** The near-fields and electric
field lines in the xz-plane at the electric and magnetic dipole res-
onances of a selected diameter of $D = 150$ nm. The electric field
enhancement is shown in (b) while (c) displays the magnetic field
enhancement.

and they can be engineered to overlap (see Figure 1.2(a)). The near-fields at the elec-
tric and magnetic dipole resonances for a nanodisk with a diameter $D = 150$ nm and
height $h = 200$ nm are displayed in Figure 1.2(b), (c). The electric field lines can aid
in revealing the underlying nature of the modes. The electric dipole resonance has
a concentrated dipolar excitation in the x-direction at the center, parallel to the po-
larization of the incident wave. We also note that, at these resonances peaks, the
plane wave couples to more than one multipolar mode, as the electric dipole also
shows signs of a magnetic quadrupole excitation. At the magnetic dipole resonance,
circulating currents are excited and give rise to a magnetic dipole moment in the y-
direction. This is also accompanied by a substantial enhancement of the magnetic
field. Detailed information of the nature of the fields can be obtained through a
multipole decomposition, which will be discussed in Chapter 2.

A central theme in the research of all-dielectric nanophotonics is the interference
and interplay between the different multipolar modes excited in the nanoparticles.
The effects of magnetic excitations interacting with electric ones was investigated
quite early on, in particular by Kerker *et al.* in the 1980's [39]. However, it took a

long while from those studies for fabrication and applications to catch up, and it was experimentally shown during this decade that these effects can become prominent in high refractive index dielectric spheres, both in the microwave [40] and visible [41, 42] regimes. In particular, as will be discussed and shown in more technical detail in Chapter 2, when an electric dipole and a magnetic dipole of equal magnitude and phase are overlapped, the back-scattering is completely cancelled. This is due to perfect destructive interference in the scattering in the backward direction. When electric and magnetic excitations fulfil this, the "first Kerker condition" is said to be fulfilled. A second Kerker condition also exists, and is related to forward scattering (Chapter 2).

In diffraction theory, it is common to phrase problems in terms of the Huygens principle (or Huygens-Fresnel principle). It essentially states that every point on a wavefront can be viewed as a secondary source of spherical waves. By geometrically mapping out the interference between these sources, the diffraction patterns from apertures and gratings can be easily obtained [43].

A particle fulfilling the first Kerker condition is typically called a Huygens' source for this reason, it is a source of secondary waves in the forward direction. An array of such sources would be non-reflective since all back-scattering is cancelled. These arrays are referred to as a Huygens' metasurfaces and they have been the subject of a lot of recent interest. The main reason for this interest is the prospect of being able to manufacture flat and thin optical elements [44]. By proper engineering of the phase of each meta-atom, the surface will re-radiate the incident beam in a highly specific manner [45, 46]. Fabrication of such metasurfaces is possible using for instance high index dielectric nanodisks [47]. It should be mentioned that these Huygens' metasurfaces are special cases of the more general phase gradient metasurface with its associated generalized laws of reflection and refraction [48], which can be either transmissive or reflective. Moreover, these metasurfaces have been demonstrated using either all-dielectric [49] or plasmonic [20] constituent elements. A recent review on phase gradient metasurfaces can be found in Ref. [50].

The Kerker conditions are manifestations of destructive and constructive interference originally tied to electric and magnetic dipolar excitations. However, such effects are not limited to dipoles. For instance, all electric multipoles have symmetric radiation while all magnetic have anti-symmetric and more general designs can be envisioned [51]. Moreover, the excitation geometry can be made more complex [52] and one can move from single particles to metasurfaces or particle aggregates. Considerations like these have been dubbed Generalized Kerker Conditions and the subject has recently been reviewed [53].

A specific example of a generalized Kerker condition is studied in **Paper I**. The system is a metasurface of silicon nanopillars on top of a glass substrate. When the metasurface is illuminated from the glass side in a total internal reflection geometry, the interference between the electric and magnetic dipolar excitations can give rise to complete suppression of the reflected signal. Since there is no transmission, this results in total absorption at that specific wavelength and incident angle. It is shown in Paper I and discussed in Chapter 4 that this condition of perfect absorption is closely related to the first Kerker condition, where $\alpha_e = \alpha_m$.

The focus of the majority of research on all-dielectric nanoparticles and metasurfaces has been on the dipolar excitations and their interaction. However, the excitation of higher multipole orders can offer additional functionalities due to more complex radiation patterns and typically higher Q-factors. However, compared to the lower order dipolar modes, fabrication and experimental realization of higher order multipoles is more challenging owing to their increased sensitivity to optical

losses and geometric shape of the particle. In fact, the scattering spectra of silicon spheres shown in in Figure 1.1 show almost no indication of higher order resonances. This is due to the absorption losses in silicon becoming relevant at shorter wavelengths.

The research in high refractive index nano-optics has exploded in recent years, and more and more applications and remarkable functionalities appear with an impressive pace. Many innovations are driven by previous experience in plasmonic nano-optics. Compared to metallic nanoparticles with plasmonic response, one of the main advantages with all-dielectric nanoresonators is their reduced Ohmic loss. However, it should be noted that at the higher order multipolar resonances, in particular of magnetic character, the absorption and heating can be significant [54]. Some select examples of recent innovations in all-dielectric nanophotonics include the previously mentioned flat optics [55–58], beam steering [59, 60], holography [61] and even subwavelength imaging [62]. Very recently, information storage using silicon nanostructures was suggested [63].

As discussed above, sensing at the nanoscale has long been driven and dominated by metallic elements with plasmonic response. Even though the spectral position of the Mie resonances in all-dielectric structures is not nearly as sensitive to the surrounding refractive index, sensing can be performed with some tricks [64–67].

Silicon is perhaps the most widely used high refractive index material in the visible range. This is due partly to the low optical losses of crystalline silicon, and partly due to its abundance and the immense experience in various fabrication techniques from the semiconductor electronics industry. However, the choice of material is sometimes limited by the application at hand and many alternatives exist including GaAs, TiO_2 and GaP, to name a few. A recent review on materials in the context of all-dielectric nanophotonics can be found in Ref. [68]. Enormous progress in the research of plasmonic nanoparticles was driven by the ability for large-scale fabrication of colloidal solutions of nanospheres, nanorods etc. Many applications of high-index dielectric nanoparticles require facile and high-throughput fabrication methods for colloidal solutions of e.g. silicon nanoparticles. Commonly employed methods such as dewetting [69] and laser ablation [70] typically result in a particle size dispersion. **Paper II** demonstrates a flexible fabrication method for metasurfaces and, with an additional fabrication step, mono-disperse colloidal suspensions of silicon nanoparticles with tailored geometric shapes and chiral response.

A plethora of applications and interesting functionalities have been reported, and this introduction is far from comprehensive. Rather, focus was devoted to the applications most relevant to the work that this thesis based on. The reader interested in a wider perspective is referred to a number of reviews [67, 71–76] and naturally the references therein.

1.4 Coupling with subwavelength emitters

A central property of high refractive index dielectric nanostructures that was not explicitly mentioned in the previous section is their ability to concentrate light into subwavelength volumes. This enhancement of near-fields naturally boosts light-matter interactions, specifically the interaction of light with objects small enough to fit inside the enhanced mode volume. In particular, the enhanced electromagnetic fields are associated with a strongly enhanced photonic local density of states (or LDoS), which can in turn amplify the rate of spontaneous decay of nearby emitters.

This concept has been known since the middle of the last century, and bears the name "Purcell effect" after its inventor [77]. This effect will be discussed in a bit more detail in Chapter 6.

The excitation of the magnetic type multipolar resonances is accompanied with an enhancement of the local magnetic field (see Figure 1.2(c)). Moreover, in a classical picture, the favourable overlap between the radiation patterns of magnetic dipole emitters and the nanoantenna magnetic dipole resonance lead to an enhanced magnetic optical density of states. Following the prediction of this effect on the spontaneous emission rates of magnetic emitters [78, 79], much attention has been devoted to the "magnetic Purcell effect", a review of which can be found in Ref. [80].

Although the Purcell effect and spontaneous emission are distinctly quantum mechanical in nature, it can be shown that a purely classical electrodynamics calculation of the power dissipated by a dipole source corresponds to the spontaneous decay rate [81]. This quantum-classical analogy is discussed in more detail in Chapter 6. For spherical particles, this decay rate can be calculated analytically [82] through the use of Mie theory, while numerical methods such as FDTD are required for more complicated geometries.

As mentioned previously, a key application for resonant nanoparticles is as a nanoantenna, communicating information between near-field and far-field. In fact, this formalism of dipole-nanoparticle coupling, along with the directional emission properties of high-index dieletric nanoparticles can be harnessed for improved nanoantenna designs [83, 84].

Importantly, the spectral tunability of the resonant response of high index dielectric nanoparticles through careful choice of geometric size and shape makes it possible to target a specific application. The response can be tuned to a particular emitter with an absorption and emission band at a specific spectral location.

Similar to their plasmonic counterparts, dimers of high refractive index nanoparticles exhibit enhanced near-fields in the gap region, albeit typically much weaker [85, 86]. Perhaps the most straightforward path to experimentally probe the aforementioned coupling effects is to place emitters in close proximity to dielectric nanostructures, either single particles or composite structures like dimers. This has been achieved through various methods, including using a near-field scanning probe [87, 88], thin film deposition [89, 90] or freely diffusing flourophores [91].

In contrast to plasmonic nanoantennas, however, the majority of the enhanced electromagetic fields are confined to the interior of the high index nanoparticles (see Figure 1.2). This is a direct consequence of the geometric nature of the resonances. The interior of the particle can be engineered to be accessible to an emitter through various tricks. Two commonly used ways to accomplish this are to introduce holes to the dielectric nanoantenna, such that emitters can penetrate [76, 92] or by incorporating the emitter directly in the antenna fabrication. This second method can involve doping the antenna material with semiconductor quantum dots [93, 94] or using luminescent defects in the antenna material such as a nitrogen vacancy center in a diamond nano-antenna [95, 96].

In **Paper IV**, we propose a method similar to the first one, namely fabrication of cylindrical nanoantennas of *porous* silicon. By making the antenna permeable, the enhanced near-fields can become accessible to emitters e.g. in colloidal solution. Meanwhile, the method can benefit from rich previous experience with porous silicon fabrication and classification methods [97].

The above discussion is focused on atomic or molecular emitters as well as quantum dots and thus glosses over other important sources of emission such as excitons

in transition metal dichalcogenides (TMDCs) or in halide perovskites. Discussion about such sources of light in this context can be found in a very recent review [98].

Moreover, the introduction and this thesis work focuses on weak coupling between emitters and antennas and thus excludes from the discussion the very active research field of "strong coupling", which is associated with the emergence of new hybrid light-matter polaritonic states [99].

1.5 Optical forces

It is perhaps not obvious from our everyday lives that light carries momentum and can exert forces on matter. We certainly do not feel any pressure from our lamps. Even the small and light dust particles that are sometimes visible in a room during a particularly sunny morning do not seem to be pushed around by the sunlight. Nevertheless, the photons in the light do transfer some momentum to the particles, even though the resulting forces are negligible.[†]

However, when the matter particles are even smaller and the light is tightly focused, the situation changes. The transfer of momentum from the photons can exert significant forces on the particles, and even hinder their movement.

Nearly 50 years ago, Arthur Ashkin performed a series of experiments that demonstrated this effect for dielectric particles with sizes in the micrometer range [101]. Around fifteen years later, Ashkin proceeded to demonstrate the possibility of capturing such particles in three dimensions using a single focused laser beam [102]. Since then, optical confinement and manipulation of small objects has been an extremely valuable tool and has been given the fitting name "Optical Tweezers" and nowadays pre-built and complete optical tweezer set-ups are commercially available. In fact, Ashkin was awarded part of the 2018 Nobel prize in physics for his invention of the optical tweezer.

Applications of the method are numerous. Owing to the favourable overlap of relevant sizes and force magnitudes, optical tweezers have found a natural home in biology and biotechnology. Examples where the technique is often employed include the study of single biomolecules responsible for transport and reactions in cells [103, 104], and specifically the dynamics of DNA and RNA [105, 106].

Physicists have also made great use of the technology and some examples among many include applying it to the cooling of neutral atoms [107] (1997 Nobel prize in physics) and nanoscopic thermodynamics [108, 109].

In the middle of the 90's, it was demonstrated that metallic nanoparticles with plasmonic response could be trapped in three dimensions [110]. In particular, use of gold nanoparticles combines the flexibility of optical manipulation with the rich plasmonic properties, chemical stability and facile colloidal fabrication. As a result, the topic has since then been the subject of avid research and has recently been reviewed [111]. A few research directions among many include enhanced chemical reactions [112], photothermal heat generation and profiling [113, 114] and continued study of DNA [115].

The restoring forces needed to confine a nanoparticle are intimately linked to the strength of the optical response of the particle. At the same time, such strong optical response in metallic nanoparticles is accompanied by a pronounced photothermal heating induced by absorption. This can have serious consequences for thermally sensitive biological applications. Moreover, the environmental temperature affects

---

[†]The optical forces are negligible on the dust in the room where there is air, but they can be important for interplanetary and interstellar dust [100].
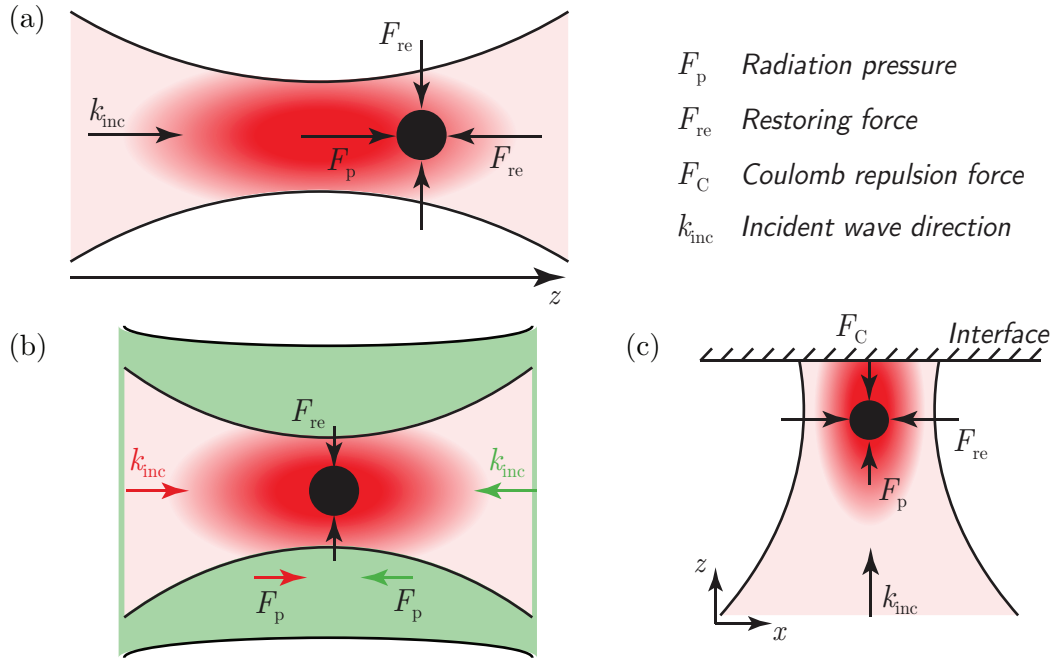
FIGURE 1.3: **Sketch of optical trapping configurations. (a)** A single-beam optical trap. The restoring forces in along the optical axis balance the radiation pressure. **(b)** Two counter-propagating beams can be used, the radiation pressure of the beams counteract one-another while the restoring forces in the lateral directions are provided by one or both. **(c)** The particle can be optically trapped against an interface, where the radiation pressure is counteracted by Coulomb repulsion from a interface with the same charge polarity as the particle.

the motion of the particle within the trap, as well as the viscous properties and even optical properties of the solution [116, 117]. As discussed above, the geometric Mie resonances in high-index dielectric structures can provide a strong optical response while keeping photothermal heating limited. Along with the interesting interplay between electric and magnetic multipolar excitations in these particles, this has made optical trapping and manipulation of high index nanoparticles an interesting topic of research and it was recently experimentally demonstrated for silicon in Ref. [118] as well as in **Paper II**. Harnessing the size-dependent optical response of these particles can provide an avenue to manufacture mono-disperse colloidal solutions of nanoparticles by optical sorting [119, 120].

In order for a three-dimensional optical trap to be able to stably confine a particle, the restoring forces have to overcome the momentum transfer in the forward direction, i.e. the radiation pressure. For resonant particle response, this is difficult to achieve since the radiation pressure forces are routinely larger than the restoring forces along the optical axis. Therefore, many experimental implementations rely on the optical restoring forces only for lateral (2D) confinement, while using other methods such as two counter-propagating beams [101] or the Coulomb repulsion from a nearby surface [121, 122] to counteract the axial radiation pressure force (see Figure 1.3).

When optical absorption is low, such as for a silicon particle at energies close to the band-gap, the optical force is given rise to only by scattering. These forces

are directly related to the rate of momentum transfer to the particle from the scattered photons and thus the direction of the scattered radiation must therefore play a central role for the induced force. In this context, the directional emission properties of high-index dielectric particles discussed above are paramount. Indeed, such effects have been considered for the radiation pressure on high-index dielectric nanoparticles illuminated by plane waves [123] and in the context of optical pulling forces and laser tractor beams [124]. In **Paper III**, we map out how the directional scattering associated with the first Kerker condition affects silicon particles in a focused laser beam. In particular, we calculate the trap stability in terms of the optical potential depth as a function of particle size for spherical and spheroidal particle shapes. Moreover, we provide insight into the multipolar contributions to the restoring forces as well as the radiation pressure.

In many of the applications discussed above, optically trapped nanoparticles have been used as nanoscopic probes. In particular, such particles can be used to measure forces and temperatures at the nanoscale. In this context, the size and material of the nanoparticle are crucial ingredients. In **Paper VI**, we make a material comparison for a few select laser wavelength relevant for optical trapping. We focus on both two- and three-dimensional trapping and take photothermal heating effects on the trap stability into account.

1.6 Outline of the thesis

After the preceding general introduction to the topics that this thesis is based on, a number of more technical chapters follow. Rather than introduce and review the topics, these chapters are intended to introduce and discuss the *methods* that were employed in the research.

Since the optical response of high-index dielectric nanoparticles routinely consists of multiple multipole orders, understanding of such systems requires tools to separate these. In Chapter 2, the multipole basis for the electromagnetic fields is introduced and various means of multipole decomposition are discussed. The interference between different multipoles, and in particular the Kerker conditions, are discussed in more detail. Moreover, an introduction is given to Mie theory, the important exact analytical solution to the spherically symmetric scattering problem.

For more complicated scattering geometries, where exact analytical solutions are absent, numerical methods are needed. The finite-difference time-domain method is a very powerful and general purpose method that has been used extensively throughout the thesis work. This method is discussed in detail in Chapter 3.

Where complete and exact analytical methods are not possible, semi-analytical approaches and approximations can nevertheless prove useful in understanding a system. One such example is the island-film theory, an effective medium-like approach to the description of metasurfaces. It is introduced and discussed in Chapter 4.

In order to understand and predict the optical confinement and trapping of nanoparticles, the calculation of optical forces is paramount. In Chapter 5, obtaining the optical force from the conservation laws of linear momentum is discussed, along with the powerful T-matrix approach for its calculation.

As mentioned in the introduction above, the enhanced near-fields associated with the resonant response of high-index dielectric nanoparticles give rise to enhanced local density of states. This can greatly affect the coupling to nearby emitters, which is discussed in Chapter 6.

Finally, some concluding remarks are given in Chapter 7. In particular, the appended papers are discussed and a brief outlook is given.

The appendices A-E contain details and derivations that were deemed to compromise the readability of the main thesis text but are nevertheless relevant enough to include.

Chapter 2

Multipole basis for electromagnetic fields

The Maxwell equations in a homogeneous medium can be rewritten into wave equations with solutions that propagate – electromagnetic radiation. Such radiation must be generated by some sort of source. Physically, it is given rise to by moving charges. For example, driving an alternating current through a thin wire will give rise to radiation with a frequency set by the frequency of the current.

The interaction of light with matter drives charge oscillations in the atoms and the matter becomes polarized. These charge oscillations then subsequently give rise to secondary radiation. In the case of atoms and very small particles (compared to the light wavelength, λ), the nature of this secondary radiation is completely electric dipole dominated. The reason is that when $\lambda \gg d$ (where d is some relevant length scale related to the particle size), the fields effectively do not vary across the dimensions of the particle and it behaves as an electric dipole.

For larger particles, as they are no longer deeply subwavelength, there can be a variation of the fields across their volume. This gives rise to more complicated charge distributions and more multipoles are needed.

In general, the electric field can be written in a series of spherical multipoles according to

$$\vec{E}(\vec{r}) = \sum_{\tau=1}^{2} \sum_{\ell=1}^{\infty} \sum_{m=-\ell}^{\ell} a_{\tau\ell m}\vec{\psi}_{\tau\ell m}^{(j)} + b_{\tau\ell m}\vec{\psi}_{\tau\ell m}^{(h)} , \qquad (2.1)$$

where $\vec{\psi}_{\tau\ell m}(kr, \theta, \varphi)$ are the vector spherical basis functions, details and definitions of which are given in Appendix A.

There is a lot to say about Equation (2.1). The total electric field is divided into a superposition of *incident* and *outgoing* waves. The incident waves are characterized by the coefficients a while the coefficents b are for the outgoing waves. As an example, for the scattering problem of a sphere illuminated by a plane wave, the incoming plane wave is encoded in $a_{\tau\ell m}$ and the scattered field in $b_{\tau\ell m}$.

The symbol τ in Equation (2.1) denotes the multipole type, $\tau = 1$ are the magnetic multipoles while $\tau = 2$ are the electric ones. In these spherical multipole series, the "quantum number" ℓ corresponds to multipole order ($\ell = 1$ for dipole, $\ell = 2$ for quadrupole etc.). A field configuration of a certain multipole order ℓ can be arranged in space in $2\ell + 1$ independent ways. In some sense, the polarization direction of the fields is encoded in the azimuthal number m. For instance, a dipole has 3 independent directions. Along the z-axis corresponds to $m = 0$ while $m = \pm 1$ are circularly polarized in-plane dipoles.

The superscript (j or h) on the basis functions indicates the choice of radial function for the fields. The incident waves need to be well-behaved at the origin, so the

choice of radial function has to be the spherical Bessel functions $j_\ell(kr)$. The scattered fields need to fulfil the boundary condition of outgoing spherical waves at infinity, so in that case the choice has to be the spherical Hankel functions $h_\ell^{(1)}(kr)$.

The specific decomposition of the fields into regular (incident) and outgoing waves in Equation (2.1) was popularized by Waterman [125]. As will be discussed in more detail in Chapter 5, the expansion coefficients $a_{\tau\ell m}$ and $b_{\tau\ell m}$ are related by the Transition matrix, namely $\vec{b} = \vec{T} \cdot \vec{a}$. It is worth mentioning another common representation, which in a sense is more fundamental, namely the the S-matrix or scattering matrix. This instead relates converging spherical waves ($h_\ell^{(2)}$ radial dependence) to diverging (outgoing) spherical waves ($h_\ell^{(1)}$ radial dependence).

Another thing worth mentioning here is the fields generated by a dipole source. In a homogeneous medium, these fields are only outgoing ($a_{\tau\ell m} = 0$) and we have $\ell = 1$. The electric field is

$$\vec{E}_{\mathrm{d}}(\vec{r}) = b_{\tau 1 m} \vec{\psi}_{\tau 1 m}^{(h)} \ . \tag{2.2}$$

It is not uncommon for confusion to arise with regards to normalization of dipole moments, especially in a homogeneous medium other than vacuum. The correct normalization for an electric *point* dipole along the z-axis is

$$b_{210} = \frac{k^3}{\sqrt{6\pi\varepsilon_0\varepsilon_r}} p_z \ , \tag{2.3}$$

where k is the wavenumber in the medium and ε_r is the relative permittivity of the medium. The derivation of this coefficent can be found in Appendix B along with expressions involving p_x, p_y and corresponding magnetic dipoles.

2.1 Mie theory

One of the most widely used and important problems in nanophotonics and optics in general is the scattering of light by an arbitrarily sized sphere, owing to the fact that it has an exact analytical solution. This scattering problem is typically referred to as Mie theory, after Gustav Mie who presented the solution in 1908 [30].

There are particularly good derivations and discussions about this problem in Bohren and Huffman [126], but in a different basis of vector spherical harmonics. Therefore I will only mention here how the solution looks in the present basis.

In this case, space is divided into two regions (Figure 2.1): the interior of the sphere (denoted region 1) and the surrounding medium (region B, for background). We call the sphere radius a and the let sphere be optically characterized by $\varepsilon = \varepsilon_0\varepsilon_1 = \varepsilon_0 n_1^2$ and $\mu = \mu_0\mu_1$. The optical properties of the surrounding medium are $\varepsilon = \varepsilon_0\varepsilon_B = \varepsilon_0 n_B^2$ and $\mu = \mu_0\mu_B$ and the origin is placed at the center of the sphere.

The fields on the outside of the sphere contain the incident wave (which is regular at the origin) as well as the scattered fields (which are outgoing spherical waves at infinity). The electric fields thus takes the general form in Eq. (2.1), namely

$$\vec{E}_B(\vec{r}) = \vec{E}_i(\vec{r}) + \vec{E}_s(\vec{r}) = \sum_{\tau\ell m} a_{\tau\ell m} \vec{\psi}_{\tau\ell m}^{(j)} + b_{\tau\ell m} \vec{\psi}_{\tau\ell m}^{(h)} \ . \tag{2.4}$$

Here, the coefficients $a_{\tau\ell m}$ encode the incident field (not necessarily a plane wave!) and $b_{\tau\ell m}$ describes the scattered multipole fields. The objective is to find these b coefficients. Given those, the fields everywhere outside the sphere are known.
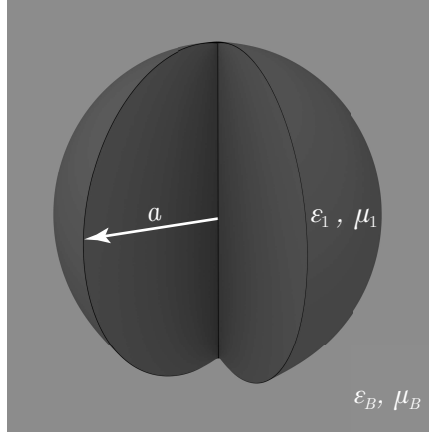
FIGURE 2.1: **Geometry of Mie scattering.** A spherical particle with radius a and *relative* optical properties ε_1, μ_1 is embedded in a homogeneous medium characterized by ε_B, μ_B.

The fields in the sphere interior can only be comprised of waves that are well-behaved at the origin, which is to say that only $\vec{\psi}^{(j)}_{\tau\ell m}$ is present. We have

$$\vec{E}_1(\vec{r}) = \sum_{\tau\ell m} A_{\tau\ell m} \vec{\psi}^{(j)}_{\tau\ell m} \,. \tag{2.5}$$

The specific form of these field expansion coefficients is constrained by the boundary conditions at the sphere surface. The boundary conditions for the tangential components of the fields are [127]

$$\hat{r} \times (\vec{E}_B - \vec{E}_1)\Big|_{r=a} = \hat{r} \times (\vec{H}_B - \vec{H}_1)\Big|_{r=a} = 0 \,, \tag{2.6}$$

where the magnetic fields in the respective regions are obtained through the Maxwell equation $\nabla \times \vec{E} = i\omega\mu\vec{H}$.

Solving for the scattered field coefficients in terms of the incident field coefficients yields

$$b_{1\ell m} = t_{1\ell}\, a_{1\ell m} \,, \tag{2.7}$$

$$b_{2\ell m} = t_{2\ell}\, a_{2\ell m} \,, \tag{2.8}$$

where $t_{\tau\ell}$ are the sphere response functions given by

$$t_{1\ell} = -\frac{\mu_1\psi_\ell(Mx)\psi'_\ell(x) - M\mu_B\psi_\ell(x)\psi'_\ell(Mx)}{\mu_1\psi_\ell(Mx)\xi'_\ell(x) - M\mu_B\xi_\ell(x)\psi'_\ell(Mx)} \,, \tag{2.9}$$

and

$$t_{2\ell} = -\frac{\mu_1\psi_\ell(x)\psi'_\ell(Mx) - M\mu_B\psi_\ell(Mx)\psi'_\ell(x)}{\mu_1\xi_\ell(x)\psi'_\ell(Mx) - M\mu_B\psi_\ell(Mx)\xi'_\ell(x)} \,, \tag{2.10}$$

where ψ_ℓ and ξ_ℓ are Riccati-Bessel and Riccati-Hankel functions, respectively (Appendix A), and we have introduced the size parameter $x = k_B a$ and the relative refractive index $M = k_1/k_B = n_1/n_B$.

We can notice, as a check, that these coefficients vanish in the limit $M = 1$, $\mu_1 = \mu_B$, i.e. in the limit where the sphere disappears. Moreover, we notice that the

sphere response is independent of m, which is a manifestation of the perfect spherical symmetry of the problem. In terms of the sometimes employed notation of "Mie coefficients" given e.g. in Bohren and Huffman [126], we have $t_{1\ell} = -b_\ell$ and $t_{2\ell} = -a_\ell$.

The most common scenario where the term Mie theory is used is the scattering of a plane wave by a sphere which will be discussed in the next section. However, we note that these equations describe a sphere's response to any field expressed in this basis.

For instance, if a scattering problem consists of multiple spheres, one can express the total field exciting sphere i as the incident field plus the scattered field from all other spheres. However, since the response of sphere i is expressed in coordinates centered around the particle, such a problem requires translation of coordinate systems. For translations and expressions of this type in the present basis, see for example [128].

Another example is the response of a sphere to a focused laser beam. This was used in Papers III and VI to calculate optical forces and the method will be discussed in Chapter 5.

Plane wave scattering

For the special case of the illumination of the sphere by a plane wave, one needs to find the expansion of a plane wave in terms of the basis functions $\vec{\psi}_{\tau\ell m}$. For completeness, these are given for a general plane wave in Appendix D, along with a few convenient special cases. For the present case of the scattering by a spherical particle, it is enough to consider a circularly polarized plane wave propagating along the z-axis, for which the a-coefficients are particularly convenient. We employ circular polarization basis vectors

$$\hat{e}_{\pm 1} = \frac{\hat{x} \mp \mathrm{i}\hat{y}}{\sqrt{2}} , \qquad \hat{e}_0 = \hat{z} , \tag{2.11}$$

and an incident plane wave with an electric field

$$\vec{E}_i = E_0 \hat{e}_+ \mathrm{e}^{\mathrm{i}kz} . \tag{2.12}$$

In this case, only $m = -1$ contributes (see Appendix D), and

$$a_{1\ell m} = \mathrm{i}^\ell \sqrt{2\pi(2\ell+1)} E_0 \, \delta_{m,-1} , \tag{2.13}$$

$$a_{2\ell m} = -\mathrm{i}^\ell \sqrt{2\pi(2\ell+1)} E_0 \, \delta_{m,-1} . \tag{2.14}$$

The power scattered by the sphere into the far field is given by (Appendix E)

$$W_s = \frac{1}{2k\mu_0\mu_B\omega} \sum_{\ell m} |b_{1\ell m}|^2 + |b_{2\ell m}|^2 , \tag{2.15}$$

and the scattering cross section can be obtained through normalization by the incident intensity. For a plane wave, the incident intensity (in W/m^2), i.e. the magnitude of the Poynting vector, is given by (e.g. [43])

$$I = \frac{c_{\mathrm{rel}}\varepsilon_0\varepsilon_r}{2}|E_0|^2 = \frac{\omega\varepsilon_0\varepsilon_r}{2k}|E_0|^2 , \tag{2.16}$$

where now k is the wavenumber in the medium. We find

$$\sigma_s = \frac{W_s}{I_i} = \frac{1}{k^2|E_0|^2} \sum_{\ell m} |b_{1\ell m}|^2 + |b_{2\ell m}|^2 \;. \tag{2.17}$$

If we insert the incident plane wave coefficients (Equations (2.13) and (2.14)) into the expressions for the b-coefficients (Equations (2.7) and (2.8)), the cross section becomes

$$\sigma_s = \frac{2\pi}{k^2} \sum_{\ell} (2\ell + 1)\Big(|t_{1\ell}|^2 + |t_{2\ell}|^2\Big) \;, \tag{2.18}$$

which is similar to the expressions found in Bohren and Huffman [126] and is probably the most suitable for numerical implementation, again keeping in mind that in that notation $t_{1\ell} = -b_\ell$ and $t_{2\ell} = -a_\ell$. Due to the spherical symmetry, this expression is valid for any incident polarization.

2.2 Interference and the Kerker conditions

As mentioned in Chapter 1, dielectric nanoparticles with high refractive index support Mie resonances of both electric and magnetic character in the visible and near infra-red spectral range. Interference between these multipolar modes can give rise to highly directional scattering [40, 45, 129].

To illustrate a couple of the most important effects of multipolar interference, we now focus our attention to dipole excitations in a particle illuminated by a plane wave. If we average the polarization of the incident wave, the differential scattering cross section can be written as [123] (with some change in normalization)

$$\frac{\mathrm{d}\sigma}{\mathrm{d}\Omega}(\theta) = \frac{k^4}{(3\pi)^2|E_0|^2}\left[\Big(|\alpha_e|^2 + |\alpha_m|^2\Big)(1 + \cos^2\theta) + 2\mathrm{Re}\{\alpha_e\alpha_m^*\}\cos\theta\right], \tag{2.19}$$

where the dipole polarizabilities are assumed to be isotropic and define the dipole moments with respect to the *incident* fields through $\vec{p} = \varepsilon_0\varepsilon_r\alpha_e\vec{E}_i$ and $\vec{m} = \alpha_m\vec{H}_i$. It is clear that interference plays a crucial role in the directionality of the scattering. Notice also that the scattering pattern is identical for pure electric and pure magnetic dipoles. Thus, in order to figure out which type of multipole is present, one needs a polarization sensitive measurement.

Looking specifically at scattering in the forward ($\theta = 0$) and backward ($\theta = 180°$) directions, we can rewrite Equation (2.19) to get

$$\frac{\mathrm{d}\sigma}{\mathrm{d}\Omega}^{F/B} = \frac{k^4}{(3\pi)^2|E_0|^2}\,|\alpha_e \pm \alpha_m|^2 \;, \tag{2.20}$$

where the plus sign is for forward scattering and minus sign for backward scattering.

Backward scattering, first Kerker condition

From Equation (2.20) it is evident that the backward scattering is completely cancelled when the electric and magnetic dipole response are exactly equal ($\alpha_e = \alpha_m$). Note that the polarizabilities are complex quantities so both real and imaginary
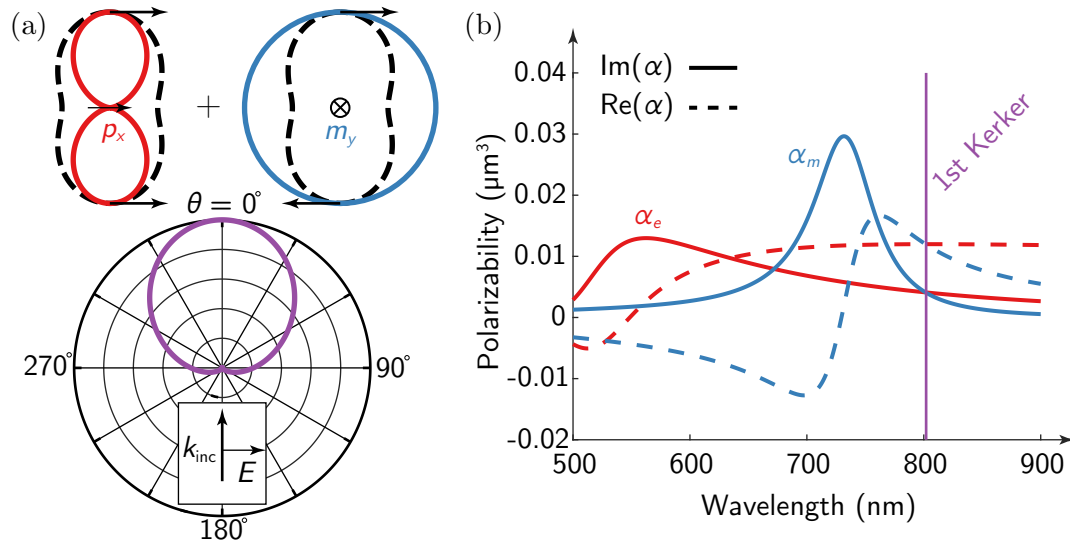
FIGURE 2.2: **The first Kerker condition. (a)** When an electric (red) and a magnetic (blue) dipole are excited simultaneously (and are perpendicular), their interference gives rise to a complete cancellation of backscattered radiation (purple). The black dashed lines show the scattering patterns for circular (or averaged) polarization. **(b)** The electric and magnetic polarizabilities for a sphere of radius $a = 100$ nm and refractive index $n = 3.5$ showing that the complex criterion $\alpha_e = \alpha_m$ can be fulfilled

parts have to match. This condition is known as the first Kerker condition, the mechanism of which is visualized in Figure 2.2.

An electric dipole excited along the x-direction has the familiar far field scattering pattern proportional to $\cos^2 \theta$, shown in red in Figure 2.2(a). Importantly, the electric field direction is symmetric in forward-backward as indicated by the black arrows at the top and bottom of the diagram. In contrast, the far field from a magnetic dipole along the y-direction (blue) has an anti-symmetric electric field distribution in the far field. The superposition of these scattering patterns gives rise to perfect constructive interference in the forward direction $\theta = 0°$ and perfect destructive interference in the backward direction $\theta = 180°$. The scattering patterns shown in black dashed curves in Figure 2.2(a) show the scattering patterns one would obtain with circular polarization or unpolarized light ($\propto 1 + \cos^2 \theta$ as in Equation (2.19)).

Figure 2.2(b) shows that this condition can be fulfilled for a subwavelength sphere ($a = 100$ nm) with a refractive index $n = 3.5$, similar to silicon in the visible to near-infrared spectral range. It is quite remarkable that both the real and imaginary parts of the polarizabilities cross at the same wavelength!

A photon that is scattered directly backwards ($\theta = 180°$) transfers the maximum possible momentum to the particle ($\Delta p = 2\hbar k$). Thus, intuitively, the backscattered radiation should be highly correlated to radiation pressure. The first Kerker condition is investigated in the context of optical forces in plane waves and focused laser beams in Paper III.

Forward scattering, second Kerker condition

The name "first Kerker condition" implies the existence of a second. Indeed, one might be tempted to try to cancel the *forward* scattering through $\alpha_e + \alpha_m = 0$. However, for passive materials, causality implies $\text{Im}(\alpha_{e/m}) > 0$ as for any response function. Thus, the imaginary parts of the two polarizabilities cannot add up to zero.

Another way to see that this is impossible is that the Optical Theorem relates the total extinction cross section to the scattering in the forward direction, so its cancellation has to imply that $\sigma_s + \sigma_a = 0$. Again, active materials can exhibit $\sigma_a < 0$ (gain) so it could in principle be achieved in such a scenario.

However, for passive materials, the condition can be approximately fulfilled (at the other crossing of $\text{Im}(\alpha_e)$, and $\text{Im}(\alpha_m)$, around $\lambda = 670$ nm in Figure 2.2(b)) and the interested reader is referred to e.g. [123, 130].

2.3   Multipole decompositions of scattered fields

What is typically experimentally measured is the extinction (in for example transmission through a metasurface or a colloidal solution) or the scattering (in e.g. a microscope with dark-field illumination). These measurements give information on the total response of the system. Similarly, the total scattering and absorption response of a nanophotonic system can easily be obtained through electromagnetic simulations such as FEM or FDTD (Chapter 3).

However, for the optimization of highly specific effects such as the directional scattering and Kerker conditions discussed in Section 2.2, one might need to know the precise nature of the resonances. This is especially important for high refractive index dielectric particles, where there are many multipolar resonances excited and they are not necessarily spectrally separated.

2.3.1   Using arbitrary external surface of integration

For an isolated particle in a homogeneous medium, it is possible to determine the multipolar nature of the scattered field through knowledge of the electric and magnetic fields on a surface enclosing the particle. Typically, this surface is chosen to be spherical [38, 127, 131] for convenience. In particular, choosing a spherical surface only requires knowledge of the radial fields $\hat{r} \cdot \vec{E}$ and $\hat{r} \cdot \vec{H}$.

However, in most electromagnetic simulation software, the fields are defined on a Cartesian grid and it can be extremely cumbersome to extract the fields on a spherical surface. Therefore, it can prove highly useful to be able to obtain the scattering coefficients from the fields on an *arbitrary* surface.

This type of multipole decomposition was used in Paper IV to analyze the multipolar response of quasi porous silicon disks. In order to maximise the coupling to local emitters/absorbers, the exact nature of the excited modes is important. These considerations are further discussed in Chapter 6.

We will use the same basis functions, $\vec{\psi}_{\tau\ell m}$, for the electromagnetic fields as in Section 2.1, the details of which are found in Appendix A. The total field outside the particle has the same general form as Equation (2.1), namely

$$\vec{E} = \vec{E}_{\text{inc}} + \vec{E}_{\text{sc}} = \sum_{\tau=1}^{2} \sum_{\ell m} a_{\tau\ell m} \vec{\psi}_{\tau\ell m}^{(j)} + b_{\tau\ell m} \vec{\psi}_{\tau\ell m}^{(h)} \ . \tag{2.21}$$
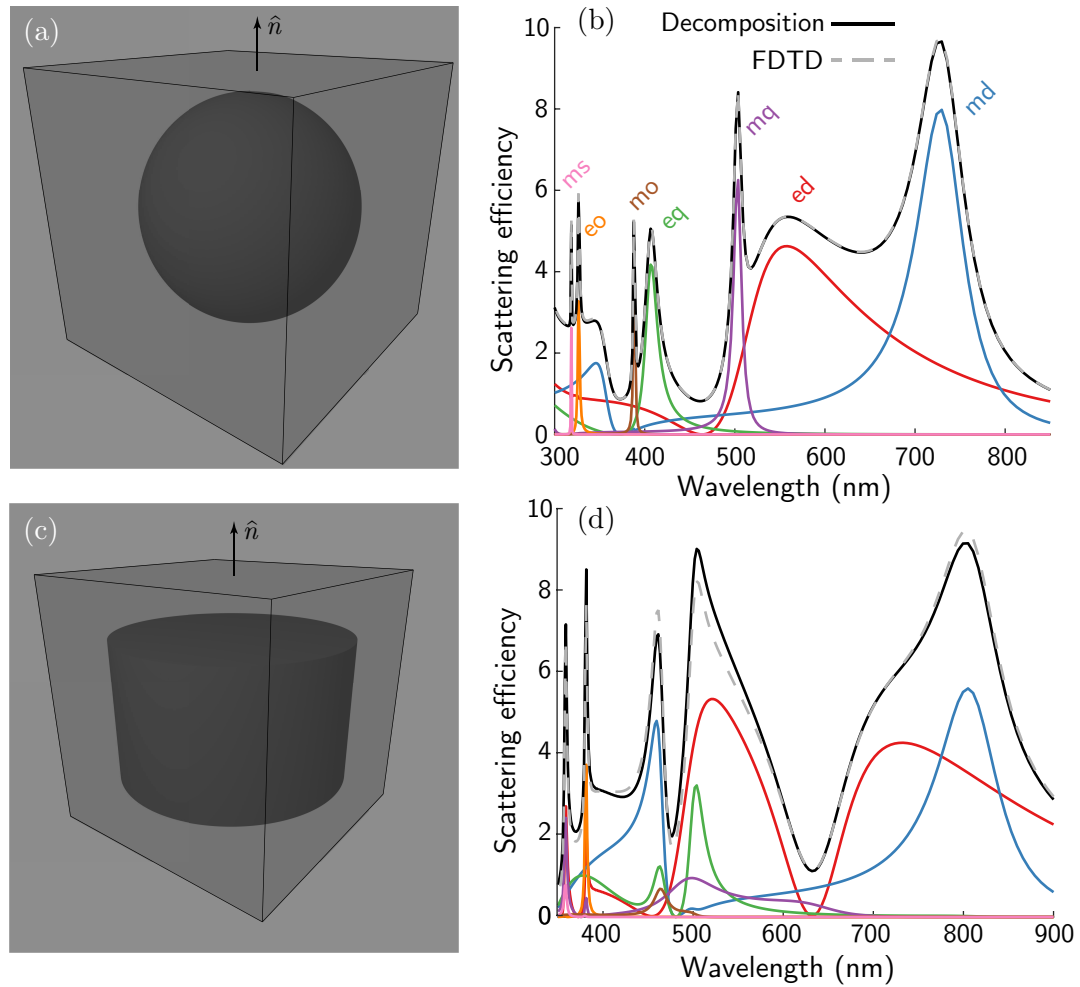
FIGURE 2.3: **Multipole decomposition of external tangential fields**
(a) A spherical particle with radius $a = 100$ nm and refractive index $n = 3.5$ is illuminated by a plane wave and the tangential fields $\hat{n} \times \vec{E}$ and $\hat{n} \times \vec{H}$ are monitored on a box enclosing the sphere. **(b)** The scattering efficiency decomposed into the spherical multipoles. The black curve shows the sum of the partial scattering amplitudes Q_ℓ while the grey dashed curve shows the total scattering from integration of the scattered field Poynting vector. **(c), (d)** The same as (a), (b) but for a disk with $R = 125$ nm and $h = 150$ nm and $n = 3.5$

Like in Mie theory, the objective is to find the scattering coefficients $b_{\tau\ell m}$. The derivation (detailed in Appendix C) follows the procedure outlined in [125], and the final result is

$$b_{1\ell m} = (-1)^m k^2 \int_S \mathrm{d}S \left[-\mathrm{i}\vec{\psi}^{(j)}_{1\ell,-m} \cdot (\hat{n} \times \vec{E}) + Z_r \vec{\psi}^{(j)}_{2\ell,-m} \cdot (\hat{n} \times \vec{H}) \right] , \qquad (2.22)$$

and

$$b_{2\ell m} = (-1)^m k^2 \int_S \mathrm{d}S \left[-\mathrm{i}\vec{\psi}^{(j)}_{2\ell,-m} \cdot (\hat{n} \times \vec{E}) + Z_r \vec{\psi}^{(j)}_{1\ell,-m} \cdot (\hat{n} \times \vec{H}) \right] , \qquad (2.23)$$

where k and $Z_r = \sqrt{\mu_0\mu_r/\varepsilon_0\varepsilon_r}$ are the wavenumber and impedance of the medium, respectively.

We make the important note that one can rewrite these integrals on the form

$$b_{\tau\ell m} = \int_S \mathrm{d}\vec{S} \cdot \vec{F} ,$$

where $\mathrm{d}\vec{S} = \hat{n}\mathrm{d}S$ and it can be shown (Appendix C) that $\nabla \cdot \vec{F} = 0$ in a region where there are no sources. Since is $\vec{F}$ divergence free, the divergence theorem tells us that we can reshape the integration surface freely, as long as the region between the new surface and the original surface contains no sources. In particular, we can deform the spherical surface into a box in Cartesian coordinates.

It can also be shown [132] that these expressions give the same result regardless of whether $\vec{E}$ and $\vec{H}$ contain incident waves or not. This can potentially also be a very useful property, since it is not guaranteed that an electromagnetic simulation software supports a straightforward separation of the scattered field and the total field. Even if it does, this guarantees that one can monitor the fields on the smallest possible surface, i.e. just shy of touching the particle surface. Depending on the simulation software and workflow, this can save computational resources such as memory. In particular if the fields are saved to disk for post-processing, it saves disk space.

An example of the application of this method is shown in Figure 2.3 for a spherical particle ($a = 100$ nm and $n = 3.5$) simulated with FDTD (Chapter 3) as well as a cylindrical particle ($R = 125$ nm, $h = 150$ nm and $n = 3.5$). Both are illuminated with a plane wave from the top.

The tangential fields are monitored on a box enclosing the particle and are decomposed into spherical multipoles according to Equations (2.22) and (2.23). The partial wave scattering efficiencies due to the ℓth multipole can be found as

$$Q^{\mathrm{m}}_\ell = \frac{1}{k^2\sigma_g|E_0|^2} \sum_m |b_{1\ell m}|^2 , \qquad Q^{\mathrm{e}}_\ell = \frac{1}{k^2\sigma_g|E_0|^2} \sum_m |b_{2\ell m}|^2 , \qquad (2.24)$$

where σ_g is the geometric cross section of the particle ($\sigma_g = \pi a^2$ for a sphere) and $|E_0|$ is the strength of the incident field. These are calculated for the chosen particles and shown in Figure 2.3(b),(d). The scattering efficiency from the multipole decomposition is compared to total scattering efficiency computed from integration of the Poynting vector of the scattered field, which is the most common way to calculate the scattering cross section of a simulated particle (this technique will be further discussed in Chapter 3).

The two simulations were run with similar meshing $\mathrm{d}x = \mathrm{d}y = \mathrm{d}z \approx 5$ nm. The results of the multipole decomposition are clearly better for the spherical particle. The sharp corners of the disk gives rise to more rapid variations of the fields and it is likely that the multipole decomposition is more sensitive to such variations than the total Poynting vector.

2.3.2 Using internal source distributions

In certain cases, it is not straightforward to obtain the fields outside a particle, but one has access to the electric fields or currents *inside* it. It can therefore be useful to be able to compute the scattering coefficients based on the source distribution. An example of this is in infinite arrays of particles where an approach similar to the previous section would fail due to the presence of sources outside a surface enclosing a unit cell.

A word of caution is in order before proceeding. Scattering coefficients that are obtained from a multipole decomposition such as this still implicitly assume a homogeneous Green's function outside the particle, i.e. that there exists a spherical surface enclosing the particle outside which there are no sources and the medium is homogeneous. This is a necessity for the fields to be written in the form of Equation (2.1). So in the case of an infinite array of particles or any complicated scattering configuration, e.g. including a mirror or substrate one needs to know the Green's function of the surrounding in order to get accurate fields. Rather, a decomposition like this answers the following question;

> *If this current distribution, $\vec{J}$, were placed in a homogeneous medium, how would it scatter and what multipole orders would that scattering contain?*

The answer to this question can be useful in understanding a system since it can give insight in to what multipolar modes of a particle get excited in a certain scattering geometry.

Such multipole decompositions are possible and can be found in Jackson's book [127], expressed in terms of volume integrals involving the induced current density

$$\vec{J}(\vec{r}) = J_r \hat{r} + J_\theta \hat{\theta} + J_\varphi \hat{\varphi} = -\mathrm{i}\omega\varepsilon_0(\varepsilon_r - 1)\vec{E}(\vec{r}) \ . \tag{2.25}$$

However, the expressions there contain spatial derivatives of the current distribution and can thus be impractical and cumbersome to implement. Fortunately, the integrals can be recast using integration by parts to obtain [131]

$$b_{1\ell m} = -\mathrm{i}k^2 Z_r O_{\ell m} \int_V \mathrm{d}^3 r \, \mathrm{e}^{-\mathrm{i}m\varphi} j_\ell(kr) \Big(\mathrm{i}\pi_{\ell m}(\theta) J_\theta(\vec{r}) + \mathrm{i}\tau_{\ell m}(\theta) J_\varphi(\vec{r}) \Big) \ , \tag{2.26}$$

and

$$b_{2\ell m} = \mathrm{i}k^2 Z_r O_{\ell m} \int_V \mathrm{d}^3 r \, \mathrm{e}^{-\mathrm{i}m\varphi} \bigg[\Big(\psi_\ell(kr) + \psi_\ell''(kr) \Big) P_\ell^m(\cos\theta) J_r(\vec{r})$$
$$+ \frac{\psi_\ell'(kr)}{kr} \Big(\tau_{\ell m}(\theta) J_\theta(\vec{r}) - \mathrm{i}\pi_{\ell m}(\theta) J_\varphi(\vec{r}) \Big) \bigg] \ , \tag{2.27}$$

where k, Z_r are the wavenumber and impedance in the medium, $\psi_\ell(x) = x j_\ell(x)$ is a Riccati-Bessel function (Appendix A) and

$$O_{\ell m} = \sqrt{\frac{2\ell + 1}{4\pi \ell(\ell + 1)} \frac{(\ell - m)!}{(\ell + m)!}} \, , \tag{2.28}$$

$$\tau_{\ell m}(\theta) = \frac{\mathrm{d}}{\mathrm{d}\theta} P_\ell^m(\cos \theta) \, , \tag{2.29}$$

$$\pi_{\ell m}(\theta) = \frac{m}{\sin \theta} P_\ell^m(\cos \theta) \, . \tag{2.30}$$

This type of multipole decomposition was used in Paper V to understand which multipoles get excited and enhanced in a periodic metasurface-on-a-mirror geometry intended for solar harvesting.

2.4 Cartesian multipole moments and toroidal moments

Up until this point, the multipole decompositions discussed have been in spherical coordinates. However, any source current distribution can also be expanded in Cartesian multipole coefficients [133]. In certain contexts, it is natural to think in terms of Cartesian multipole moments. Examples include molecules or quantum dots with a transition dipole moment or very small particles interacting with light. They will have their dipole moments along a certain axis in space.

For "optically very small" particles ($a \ll \lambda/n_p$), the interaction with incident light is completely dominated by an electric dipole response (b_{21m} is essentially the only non-zero scattering coefficient). Moreover, in this regime, the expressions for this coefficient allow some approximations since the Bessel and Hankel functions that enter in Equation (2.8) or Equations (2.26) and (2.27) have useful series expressions in this limit (both $x \ll 1$ and $Mx \ll 1$). These two approximations are important to distinguish and are thus summarized and enumerated below,

(*i*) The only relevant multipole moment excited is electric dipole, b_{21m}.

(*ii*) The Bessel and Hankel functions can be approximated to low orders in kr.

These *long wavelength* approximations of the response can provide more physical insight, provided that they are valid. One essentially replaces the particle with a point electric dipole with a polarizability, α_e. For these small particles, the cross sections and scattered electric fields are typically defined in terms of the electric dipole moment $\vec{p} = \varepsilon_0 \varepsilon_r \alpha_e \vec{E}_{\mathrm{inc}}$, which can be calculated as [127, 133]

$$\vec{p}_{\mathrm{small}} = \frac{\mathrm{i}}{\omega} \int_V \vec{J}(\vec{r}) \, \mathrm{d}^3 r \, . \tag{2.31}$$

where the induced current density is $\vec{J}(\vec{r}) = -\mathrm{i}\omega\varepsilon_0(\varepsilon_r - 1)\vec{E}(\vec{r})$.

However, when the particle is no longer "optically very small", the assumption (*ii*) above starts to worsen and one needs to take into account that the fields vary across the volume of the particle (retardation). One can rephrase the scattering coefficient in Equation (2.27) for $\ell = 1$ in terms of an electric dipole moment (compare e.g. to Equation (2.3)). If one also changes to Cartesian coordinates, one obtains the

following exact Cartesian dipole moment [134]

$$\vec{p}_{\text{exact}} = \frac{\mathrm{i}}{\omega} \int_V \mathrm{d}^3 r \, \vec{J}(\vec{r}) j_0(kr) + \frac{k^2}{2} \left[3(\vec{r} \cdot \vec{J}(\vec{r}))\vec{r} - r^2 \vec{J}(\vec{r}) \right] \frac{j_2(kr)}{(kr)^2} . \tag{2.32}$$

However, regarding this, various authors have different terminology and it can potentially become confusing. Certain authors [133] and potentially [135] and [136] would call the dipole moment in Equation (2.31) the Cartesian dipole moment. The term that is missing from Equation (2.31) is instead introduced as the electric dipole member of a new family of multipoles called Toroidal multipoles. The name toroidal stems from the current distribution of the toroidal dipole having the shape of currents flowing along the minor (poloidal) loops of a torus.

Other authors [134] (and myself included) would call (2.31) a long wavelength approximation of the electric dipole moment. In fact, for very small particles, assumption (*ii*) means that $j_0 \sim 1$ and $j_2 \sim 0$ [126, 134] and Equation (2.32) reduces to Equation (2.31).

The essential part of this dichotomy is that the electric dipole and the toroidal dipole have identical radiation patterns since they are part of the same spherical scattering coefficient.

Anapoles

Something that arises naturally if one thinks in terms of two different current distributions, electric dipole and toroidal dipole, is the possibility of a non-zero current distribution with zero radiation. Introducing, in analogy with [133, 136], the multipole moments

$$\vec{p}_c = \frac{\mathrm{i}}{\omega} \int_V \mathrm{d}^3 r \, \vec{J}(\vec{r}) , \tag{2.33}$$

and

$$\vec{T}_c = \frac{k}{10\omega} \int_V \mathrm{d}^3 r \left[(\vec{r} \cdot \vec{J}(\vec{r}))\vec{r} - 2r^2 \vec{J}(\vec{r}) \right] , \tag{2.34}$$

the total scattering with an electric dipole radiation pattern is

$$Q_{\text{sca}} = \frac{k^4}{6\pi \varepsilon_0^2 \varepsilon_r^2} |\vec{p}_c + \mathrm{i}k\vec{T}_c|^2 , \tag{2.35}$$

and it is clear that when the electric dipole moment and electric toroidal moment are out of phase and fulfil $\vec{p}_c = -\mathrm{i}k\vec{T}_c$, the scattered far field vanishes. This is called an anapole [133] and has attracted a lot of recent attention. The reason is that current distributions similar to anapoles can be excited in subwavelength disks of high refractive index [133]. While the far-field scattering is suppressed, the current distribution is non-zero and thus the internal field enhancement is large. This large field enhancement has recently been shown experimentally using Raman spectroscopy [137] and could potentially be utilized by opening a hole in the resonant nanoparticle [76].

Chapter 3

Finite-difference time-domain (FDTD) simulations

3.1 Method

The finite-difference time-domain method is a powerful technique which allows for the numerical solution of electromagnetic problems. It was introduced by Yee in 1966 [138], and a testament to its power and applicability is that this seminal paper has been cited over 10,000[†] times (as of March 2019).

The method is based on discretization of the time-dependent Maxwell equations in space and time. Knowledge of an initial boundary value (e.g. incident Electric field) allows for iteration in time with steps of δt and updating the interdependent electric and magnetic field values (see Section 3.1.1 below for an example in one dimension). This scheme is repeated until the simulation time t has reached some maximum time t_{max} or until a desired steady state has been reached in the electromagnetic fields (Section 3.2.4).

Importantly, Yee suggested a unique discretization scheme that improves the numerical stability. It is based on defining the E and H fields on separate lattices, displaced by half a spatial step. In other words, every electric field point is defined half-way between two magnetic fields points and vice-versa [138]. Moreover, the same technique was suggested for the time steps, i.e. that E is defined at times $t = m\delta t$ while H is defined at times $t = (m + {}^1\!/{}_2)\delta t$, where m is an integer. This method of constructing the spatial and temporal grids has proven to give improved numerical stability and accuracy and is at the core of most FDTD implementations [139–142].

In the work presented in this thesis, the commercially available software FDTD Solutions (Lumerical Inc., Canada) has been used for simulation of optical properties of nanostructures with high refractive index. As a result, some of the discussion in this chapter is centered around this specific software implementation and references will be made to certain settings therein.

In the software, the time-dependent Maxwell equations are solved in a simulation region in which scatterers are defined as geometrical objects with a certain dielectric function. At the edge of the simulation region, a set of boundary conditions are employed, typically either periodic or absorbing. The absorbing boundary conditions are meant to simulate a situation where the outgoing fields propagate to infinity and stop interacting with the scatterers. Different boundary conditions are discussed in Section 3.2.3.

The source field is defined in the software in terms of a temporal pulse of a certain shape and finite width. In the frequency domain, this corresponds to an

---

[†]According to Scopus. Google Scholar has close to 17,000 registered citations.

incident field containing a range of frequencies. By properly designing the incident pulse, the system response can thus be made available at a spectrum of frequencies.

Various implementations of the method other than FDTD SOLUTIONS naturally exist. Of particular note is the free and open source software package MEEP, which originated from MIT [139].

Many books have been written about the method and relevant material can be found by the curious reader [142, 143]. An informative discussion about the method and its implementation can be found in the course notes and recorded lectures from the Computational Electromagnetics course at the University of Texas at El Paso [140].

Although this thesis and appended papers deal with all-dielectric nanostructures, numerous simulations involving metallic nanoparticles with plasmonic response have also been conducted during the thesis period.

3.1.1 Example in 1D

As an illustrative example, we consider a case with a number of simplifying assumptions:

1. Linear and isotropic media, $\vec{D} = \varepsilon_0 \varepsilon_r \vec{E}$.

2. Non-magnetic media, $\mu_r = 1$.

3. The spatial variation of the optical properties is constrained to one spatial dimension (z).

4. We deal with dispersionless and lossless media, and thus assume a time-independent real permittivity ε_r and $\vec{J} = 0$.

5. We require that the fields propagate only along z, and $E_z = H_z = 0$.

Note that none of these are constraints of the FDTD method in general, just of the chosen example. The method is routinely employed in cases where some or all of these assumptions are broken. In fact, for the majority of the work in this thesis, only assumptions 1. and 2. are fulfilled.

The 3D Maxwell equations involving the curl take the following form in this simplified situation [127],

$$\nabla \times \vec{E} = -\mu_0 \frac{\partial \vec{H}}{\partial t} , \tag{3.1}$$

$$\nabla \times \vec{H} = \frac{\partial (\varepsilon_0 \varepsilon_r \vec{E})}{\partial t} . \tag{3.2}$$

The optical properties of the medium are encoded in the relative permittivity ε_r. If one writes the above equations in component form, the constraint that $E_z = H_z = 0$ has the effect that the equations decouple into two polarizations. The pairs E_x, H_y and E_y, H_x are not interdependent and they have identical wave-equations.

We can therefore focus on 1D y-polarized waves which leaves us with the following equations

$$\frac{\partial E_y}{\partial z} = \mu_0 \frac{\partial H_x}{\partial t} , \tag{3.3}$$

$$\frac{\partial H_x}{\partial z} = \varepsilon_0 \varepsilon_r \frac{\partial E_y}{\partial t} , \tag{3.4}$$

where we have used the assumption that ε_r does not vary with time. We now discretize these equations in space and time, with step size δz and δt. We introduce a Yee grid [138], so that the electric field is defined at points $n\delta z$ and at times $m\delta t$, while the magnetic field is defined at points $(n + \frac{1}{2})\delta z$ and at times $(m + \frac{1}{2})\delta t$, where m and n are integers. We drop the x and y subscripts on the fields and instead introduce the notation

$$E_n^m = E_y\big(z = n\delta z; t = m\delta t\big) \,,$$
$$H_{n+1/2}^{m+1/2} = H_x\big(z = (n + \frac{1}{2})\delta z; t = (m + \frac{1}{2})\delta t\big) \,, \tag{3.5}$$

such that the subscripts denote spatial (z) position and the superscripts denote temporal position. Approximating the derivatives in Equations (3.3) and (3.4) with finite differences results in

$$\frac{E_{n+1}^m - E_n^m}{\delta z} = \mu_0 \frac{H_{n+1/2}^{m+1/2} - H_{n+1/2}^{m-1/2}}{\delta t} \,, \tag{3.6}$$

$$\frac{H_{n+1/2}^{m+1/2} - H_{n-1/2}^{m+1/2}}{\delta z} = \varepsilon_0 \varepsilon_{r,n} \frac{E_n^{m+1} - E_n^m}{\delta t} \,. \tag{3.7}$$

From these finite differences, one can see the strength of the staggered Yee grid. For example, since the spatial derivative in the left hand side of Equation (3.6) uses the electric fields at spatial points n and $n+1$ it makes sense for the magnetic fields in the right hand side to be defined exactly in the middle of these two points – namely at $n + \frac{1}{2}$. The same principle is holds for the time derivatives and is mirrored in Equation (3.7).

In order to iterate these equations in time, they are rewritten so that the fields at the next time-step are expressed in terms of those at earlier times. This yields the following temporal update scheme,

$$H_{n+1/2}^{m+1/2} = H_{n+1/2}^{m-1/2} + \frac{\delta t}{\mu_0 \delta z} \left(E_{n+1}^m - E_n^m \right) \,, \tag{3.8}$$

$$E_n^{m+1} = E_n^m + \frac{\delta t}{\varepsilon_0 \varepsilon_{r,n} \delta z} \left(H_{n+1/2}^{m+1/2} - H_{n-1/2}^{m+1/2} \right) \,, \tag{3.9}$$

where the spatially varying optical properties are now encoded in $\varepsilon_{r,n}$. For this example, we chose 30 spatial points per vacuum wavelength and 30 temporal points per vacuum period, i.e. $\delta z = \lambda_0/30$ and $\delta t = T/30 = \delta z/c_0$.

The above 1D model was implemented using an incident field with a vacuum wavelength of $\lambda_0 = 633$ nm. We also chose to use a smooth temporal envelope to avoid components of very high frequency. We first look at a pulse with a Gaussian envelope propagating in vacuum (Figure 3.1(a)). The black line shows the electric field distribution along z at $t = 0.05$ ps while the red line is approximately 0.1 ps later. The distance in space Δz and in time Δt between the peaks of the pulse can give a measure of the propagation speed (note that Δz and Δt are not the sampling distances here). We extract

$$v = \frac{\Delta z}{\Delta t} = \frac{29.98\,\mu\text{m}}{0.1\,\text{ps}} \approx c_0 \,, \tag{3.10}$$

which is comforting.

As a second example, we introduce a vacuum-glass interface at $z = 15\,\mu$m. Figure 3.1(b) shows a pulse with $\lambda_0 = 850$ nm in black at a time before it has reached
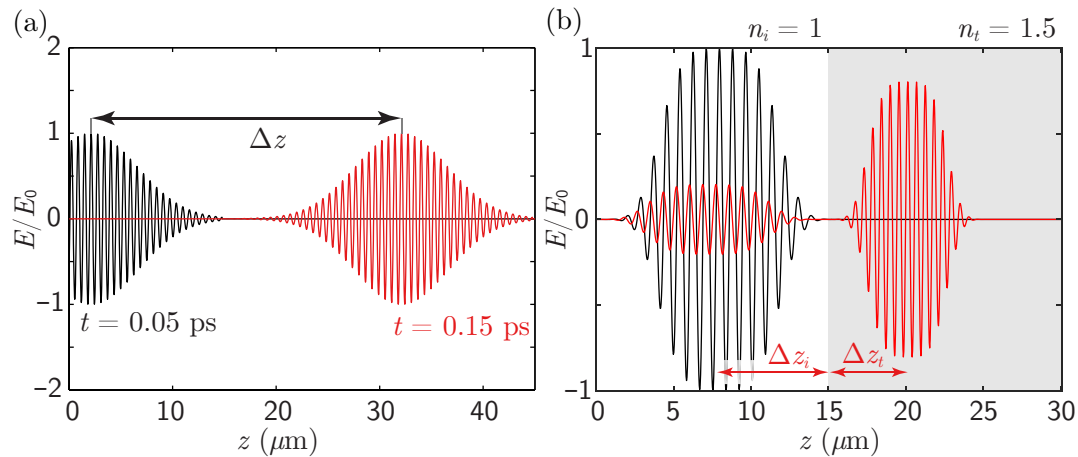
FIGURE 3.1: **One-dimensional FDTD Example (a)** A Gaussian pulse propagating in vacuum. The black line shows the E-field at $t = 0.05$ ps and the red line corresponds to the field at a time 0.1 ps later. In that time, the pulse has propagated a distance Δz. **(b)** A pulse incident on an interface between air and glass. The black line shows the pulse before it arrives at the interface and the red line shows the reflected and transmitted pulses at a later time.

the interface. The red curve shows the pulse a time after it has been divided into a reflected and a transmitted pulse. A few things can be surmised from Figure 3.1(b), which illustrate and summarize the physics involved at flat interfaces quite neatly.

- The magnitudes of reflection and transmission can be estimated from the peak values of the electric field in the reflected and transmitted pulses.

- The different light wavelengths in vacuum ($\lambda_0 = 850$ nm) and in glass ($\lambda = \lambda_0/n_t$) can be estimated from the distance between peaks in the wave packets.

- The different speed of propagation in vacuum and glass can be estimated from the difference in the distance that the reflected and transmitted pulses have traversed in the same time ($\Delta z_i \approx 7.5\,\mu$m in vacuum and $\Delta z_t \approx 5\,\mu$m in glass).

3.2   Simulation set-up

3.2.1   Material parameters

One of the most important limiting assumptions in our 1D example above is that the media were assumed to be dispersionless and lossless. All frequencies in the wave-packet propagated with the same speed and there was no attenuation.

However, at optical frequencies in particular, there is often significant material dispersion and loss and the optical properties are characterized by a frequency dependent and complex permittivity $\varepsilon(\omega)$. This frequency dependence arises from a resonant response wherein the D-field at a time t can depend on the electric field E at earlier times $t - \tau$. In other words, a temporally non-local material response. These memory effects somehow need to be implemented in the method, since without modification, an FDTD algorithm such as the 1D example above is completely local in time. There are multiple ways to implement this temporal dependence.

Without going in to detail (see e.g. [142] for detailed discussion), a pair of examples are to include an approximation of the convolution involved in calculating the D-field (PLRC-FDTD) or by introducing an auxiliary current that gets updated concurrently with the E-field (ADE-FDTD). Moreover, the material response has to be causal (it cannot respond to a pulse before it has arrived), which puts constraints on the possible forms of $\varepsilon(\omega)$. Specifically, it has to fulfill the Kramers-Kronig relations [127].

These facts have the important consequence that any experimentally measured data for wavelength dependent permittivity cannot be directly imported as it would be in a frequency domain method. Instead, it has to be modelled with causal functions.

Examples of such functions are Drude, Lorentz and Debye [141, 142], all of which are available as material options in FDTD SOLUTIONS.

However, since the sum of causal functions is also causal, what is typically done is to select a few suitable functions and fit the parameters to experimental permittivity data in a certain wavelength range. It is of course important to keep track of this fitting and make sure that it gives the desired results for the wavelengths of interest. One example encountered during this thesis work where this is of particular importance is for the material parameters of crystalline silicon at energies close to the band-gap (corresponding to $\lambda > \sim 1000$ nm). The optical absorption in this region is so low that small changes in the fitting of $\text{Im}(\varepsilon)$ can have large effects.

3.2.2 Meshing

The choice of δt and $\delta x, \delta y, \delta z$ is not a trivial matter and extensive studies have been conducted on choosing these optimally and there are requirements for numerical stability that connect δt to the spatial step sizes [138].

The choices depend greatly on the system and the phase velocities that are expected to arise. For example, the wavelength of light in a high refractive index material is shorter, so a denser spatial mesh is needed to maintain the same number of mesh points per wavelength. Additionally, in regions where the fields vary rapidly, for example near interfaces involving metals, a denser mesh is needed. One should thus be careful to give numbers as guides for selecting the mesh, and instead encourage convergence testing for each case.

In FDTD SOLUTIONS, the temporal step-size is mostly automatically selected based on the pulse characteristics and spatial mesh size. There is a "mesh accuracy" setting which will attempt to mesh the simulation region based on the optical properties of the different regions. It will for example select a denser mesh for regions with a higher refractive index. However, in many cases, it can be necessary to override this automatic meshing and select even finer meshes for certain regions. For example, in the quasi-porous silicon nanodisks studied in Paper IV, dipole sources were placed in holes in the disks. The holes had radii r that are ~ 100 times smaller than the wavelength and the near-fields were extremely important for the analysis.

3.2.3 Boundary conditions

PEC

If we had run the simulations in the above 1D example for longer times than what Figure 3.1 depicts, the pulses would be perfectly reflected off either side of the simulation region. This is due to the boundary imposing that the electric fields vanish. Physically, this would correspond to an interface where free charges *perfectly* screen

the electric field, preventing it from penetrating. This is why this boundary condition has earned the name Perfect Electric Conductor (PEC).

PEC boundary conditions are easy to implement and understand and they can sometimes be useful to describe a physical system. For example, in the microwave regime, a PEC boundary corresponds to where the system is terminated to ground. At optical frequencies, the realm of this thesis, the closest analogy to a PEC is a metallic mirror. However, since a PEC boundary is lossless, care must be taken depending on the wavelength range and application one wishes to simulate since the losses in the metal can be significant. Additionally, if there are evanescent field components close to the mirror, surface waves (SPPs) can be launched at the boundary; something a PEC boundary condition will not capture.

Absorbing boundary conditions (PML)

The simulations performed in this thesis are closely tied to various experimental illumination conditions and measurement techniques. For example, dark-field scattering spectra or transmission and reflection from a metasurface. In all these cases, the incident light interacts with the scatterer and then propagates away to the far-field. Since the simulation region is finite, we need a boundary condition that does not reflect any waves. As was discussed in the previous section, simply forcing the fields to vanish at the interface will perfectly reflect the fields. What is instead done is to introduce absorbing boundary conditions, a specific implementation of which is a Perfectly Matched Layer (PML). A layer is introduced that absorbs the fields through fictitious material properties, whose parameters are chosen to attenuate electromagnetic energy. In order to minimize reflections, these material parameters are gradually ramped up spatially to give an adiabatic impedance matching [140]. This impedance matching is where the name perfectly matched layer stems from.

Periodic

If the system under study is periodic in some direction, the entire system response can be obtained by only simulating one unit cell. Importantly, periodic boundary conditions imply that *both* the structure and the electromagnetic fields are periodic. For instance, periodic boundary conditions are not suitable to describe a periodic lattice excited by a single dipole. Placing a dipole source somewhere in a simulation region with periodic boundary conditions will simulate a system with one dipole source per unit cell.

Moreover, care should be taken when the periodicity of the structure is comparable to some wavelength contained in the pulse. This can lead to the excitation of lattice modes (Bragg modes) that may be long-lived and increase the simulation time.

Symmetric and anti-symmetric

If the system has a mirror symmetry with respect to some plane, the computational resources can be significantly reduced since the simulation can be cut in half through the use of symmetric or anti-symmetric boundary conditions. For two mirror planes, the computational domain can be cut in four (Figure 3.2(a)). Note that it is not enough that the structure is mirror-symmetric, the illumination also has to be. If, for example the illumination is oblique, this breaks the mirror symmetry in the fields, although not necessarily in every direction (see example in Figure 3.2(b)).
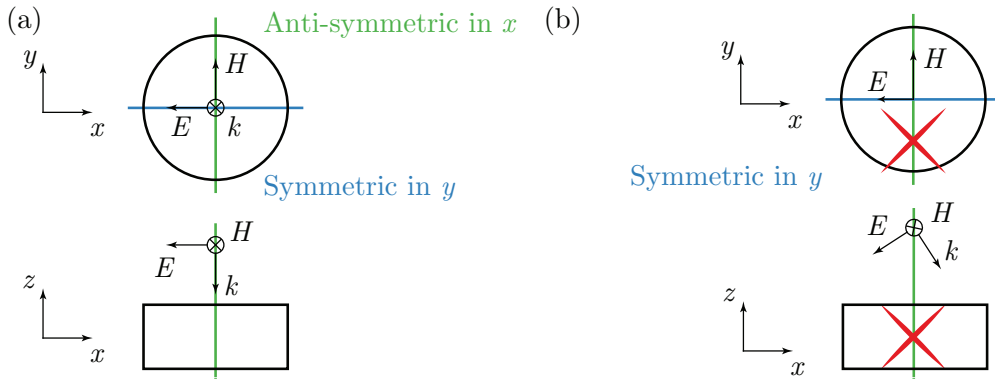
FIGURE 3.2: **Sketch of symmetric and anti-symmetric boundary conditions (a)** A cylindrically symmetric structure is illuminated from the top with E polarized along x. Both the structure and the fields have mirror symmetries in x and y, allowing two symmetry planes. **(b)** Oblique illumination breaks the mirror symmetry of the electric field in the x direction and only one symmetry plane can be used.

The names symmetric and anti-symmetric refer to the properties of the electric field on either side of the boundary, and the opposite behaviour is imposed on the magnetic field.

The FDTD method can be defined in curvilinear coordinates [142]. For example, cylindrical coordinates have been implemented in MEEP [139], but not FDTD SOLU-TIONS. A cylindrically symmetric 3D problem can thus be reduced to a 2D problem which implies a huge resource save.

3.2.4 Termination criteria

An FDTD simulation is propagated forwards in time, either to some maximum time $t_{\max}$ which is chosen in the simulation set-up, or until some desired steady state has been reached in the electromagnetic fields. For a continuous excitation (e.g. sinusoidal), the system will respond to the onset of the incident field. In this case, the steady state corresponds to when all transient system behaviour has ceased.

More common, at least in the work in this thesis, is for the incident field to be a pulse of a limited temporal width. The system response is then calculated both during the pulse propagation and in its wake. In this case, as will be discussed below, the boundary conditions are usually absorbing in at least one spatial direction and the desired steady-state corresponds to when the electromagnetic energy, U, contained in fields has reduced to below a certain threshold. This attenuation can either be achieved through absorption in the materials or through energy "leaving the simulation region" through absorption by the PML boundary conditions. Typical choices for this criterion that have been found to work well are $U/U_{\mathrm{inc}} = 10^{-5}$ or 10^{-6}, where U_{inc} is the injected electromagnetic energy.

If the criterion for termination is that the fields have been attenuated below a certain threshold, the simulation time can be greatly affected by the eigenmodes of the system. If an eigenmode with a high lifetime is excited, the response of the system will live long after the exciting pulse has passed. This fact directly translates to longer simulation times. Examples of long-lived modes include high order multipolar Mie resonances in dielectric nanoparticles or Bragg modes in periodic metasurfaces.

3.3　Analysis

As a consequence of how the FDTD method is formulated, the electric and magnetic fields have to be calculated in each spatial mesh element at each time-step. Thus, at the end of a simulation, the electric and magnetic fields are available as a function of time and their Fourier transforms contain the frequency dependent response.

3.3.1　Absorption and scattering

Scattering and absorption spectra convey very important information about a nanoparticle, such as the spectral location various resonances and the strength of their coupling to the incident wave. Therefore, these spectra are two of the most important quantities to study in the context of nanophotonics research.

　　One of the most common examples simulated in this thesis work is a nanoparticle of a certain geometrical shape illuminated by a plane wave either in free space or in the presence of a lossless substrate. In this scenario, it is possible to construct a closed surface S enclosing the particle. The *net* rate of electromagnetic energy crossing the surface is given by [126]

$$W = \int_S \mathrm{d}A\, \vec{S} \cdot \hat{n} \,, \tag{3.11}$$

where $\hat{n}$ is an outward normal vector to the surface and

$$\vec{S} = \frac{1}{2}\mathrm{Re}\{\vec{E} \times \vec{H}^*\} \,, \tag{3.12}$$

is the time-averaged Poynting vector. Here, $\vec{E}$ and $\vec{H}$ are the fields in the frequency domain obtained through Fourier transforming the temporal fields in the FDTD simulation. They are expressed in phasor notation (harmonic time-dependence) and are thus complex.

　　In order to separate absorption and scattering, one can divide the simulation region into two distinct parts (Figure 3.3). A central part (region I) containing the scatterer where $\vec{E}$ and $\vec{H}$ are the total fields, namely $\vec{E}_\mathrm{I} = \vec{E}_\mathrm{inc} + \vec{E}_\mathrm{scat}$ and analogously for the magnetic fields. In the outer part (region II), the incident wave is subtracted, leaving only the scattered fields so that $\vec{E}_\mathrm{II} = \vec{E}_\mathrm{scat}$.

　　In FDTD SOLUTIONS, this delineation is accomplished through defining the plane wave source as a "Total-Field Scattered-Field" (TFSF) source, the boundary of which is indicated as the dashed line in Figure 3.3(a).

　　To calculate the scattering, we place a closed surface S_II in the scattered field region. Since the only fields that exist in this region are the scattered fields, any net power flow through this surface will correspond to the power scattered into the far-field. Thus,

$$W_\mathrm{scat} = \int_{S_\mathrm{II}} \mathrm{d}A\, \vec{S}_\mathrm{II} \cdot \hat{n} \,. \tag{3.13}$$

In order to understand how to calculate absorption in this way, it might be helpful to assume first that the particle is lossless. In this case, there can be no net energy flow through a closed surface S_I placed in region I, since both the incident wave and the scattered wave are defined here. Loosely speaking, any energy carried into the volume by the incident wave will either exit as scattering or not interact with it. For a particle with non-zero losses, any net energy flow across the surface will thus

be directed *inward*, and be equal to the absorbed power (Poynting's theorem [127]). We have

$$W_{\text{abs}} = - \int_{S_{\text{I}}} \mathrm{d}A \, \vec{S}_{\text{I}} \cdot \hat{n} \ . \tag{3.14}$$

Note that this method of calculating absorption is applicable to any simulated system with any illumination conditions[†] since the fields that are typically monitored are the total fields. This specific construction with the two regions enables the calculation of scattering.

For the specific case of plane wave illumination, one obtains the scattering cross sections by normalizing by the incident intensity,

$$\sigma_{\text{abs}} = \frac{W_{\text{abs}}}{I_{\text{inc}}} \ , \qquad \sigma_{\text{scat}} = \frac{W_{\text{scat}}}{I_{\text{inc}}} \ , \tag{3.15}$$

where I_{inc} is the magnitude of the incident Poynting vector in units $\mathrm{W/m}^2$ (Equation (2.16)).

This method of calculating the scattering and absorption was used frequently in the work that this thesis is based on, since this work is closely tied to various optical experiments. In particular, the scattering cross section is a good way to compare to a dark-field scattering spectrum. On the other hand, a measurement of transmission through a metasurface can be well described by the extinction $\sigma_{\text{ext}} = \sigma_{\text{scat}} + \sigma_{\text{abs}}$ which can easily be obtained with this method.

In Paper I, the method was used to simulate the extinction of the silicon nanopillars in order to understand their optical response.

In Paper II, the extinction was calculated for two orthogonal circular polarizations and used to simulate the circular dichroism exhibited by the silicon nano-crescents.

In Paper IV, the scattering cross section obtained through this method was used to characterize the quasi-porous silicon nanodisks. It also served as a comparison to the total scattering obtained from the multipole decompositions of the scattered fields (see Chapter 2, and specifically Section 2.3).

In Paper V, this method was used to calculate the absorption in the hydrogenated amorphous silicon nanopillars that were periodically spaced. This illustrates the point made above, that the method of calculating absorption extends beyond simple geometries.

3.3.2 Near fields

Scattering and absorption can provide condensed spectral information on the response of a system. However, in order to understand the precise nature of the response, it can sometimes be necessary to look at the near-fields in and around the structure. These can be accessed as a function of frequency and space at the end of an FDTD simulation. In principle, all optical properties can be calculated in post-processing if all electromagnetic fields are saved. However, this requires storage of complex electric and magnetic field vectors (6 numbers each) saved in three spatial dimensions and in frequency. For fine spatial meshing and dense spectral sampling,

---

[†]The absorbed power can always be obtained this way. However, what one is typically interested in is the fraction of the incident power that has been absorbed. This is straightforward for a plane wave, but for e.g. a dipole source in the near field, this normalization can become tricky.
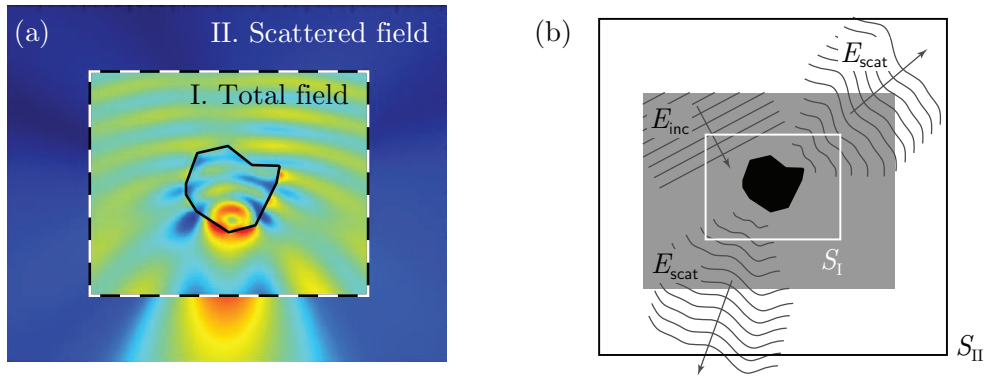
FIGURE 3.3: **Sketch of the Total Field-Scattered Field (TFSF) setup**
The simulation region is divided into two parts, a total field and a
scattered field region. **(a)** Magnitude of the electric field at a cer-
tain wavelength in both regions. **(b)** We place two closed surfaces of
integration, S_I and S_II, in the total field and scattered field regions,
respectively.

this naturally leads to prohibitively large memory and/or disk space requirements.
It is therefore important to be selective and save only the fields one actually needs.

The extraction and analysis of near-fields was also used extensively throughout
the thesis period.

In Paper I, the internal 3D fields of the silicon nanopillars was used to calculate
the electric and magnetic dipole moments and extract the polarizabilities. These
polarizabilities were then used in the Island-film model (Chapter 4) to simulate the
reflection from the metasurface.

In Paper II, the near fields were extracted and the instantaneous direction of the
electric field lines was used to interpret the circular dichroism, namely the different
scattering response for two orthogonal circular polarizations.

In Paper IV, FDTD was used to simulate the quasi-porous silicon disks. The
available electromagnetic energy density was calculated from the internal 3D elec-
tric and magnetic fields in the pores. Moreover, the fields were monitored on the
two-dimensional box surrounding the silicon particle and we used a method for
performing a multipole decomposition of the scattered fields regardless of if this
box was placed in a total field or a scattered field region (see Section 2.3 for a de-
scription of this method).

Although not included in the appended papers, the electromagnetic fields on
a closed surface obtained through FDTD have frequently been used to calculate
optical forces and torques through the use of the Maxwell stress tensor (Chapter 5)
as part of other projects during the thesis period.

3.4   Strengths and weaknesses of FDTD

A few things are worth noting about FDTD that stand in contrast to other methods
typically used, and a few of them summarize some of the points made previously
in the chapter.

+ FDTD is an intuitive method that relies on the direct solution of the Maxwell
  equations. It is very general and can be applied to all manner of geometries.

+ Since it is a time-domain method, injection of a broadband pulse makes the optical response for a spectrum of frequencies available from a *single* simulation through Fourier transforms. The broadband response of nanoparticles and metasurfaces is often of interest, making this a very useful property.

- If the desired end result is the frequency domain response, the dielectric functions cannot be directly imported from tabulated, experimental values in the frequency domain. These need to be fitted using a combination of functions (for example Drude or Lorentzian functions). The dielectric functions need to fulfil the Kramers-Kronig relations (causality) [127]. However, a combination of these functions can most often be fitted to experimental data in the spectral region of interest.

- It is not straightforward to simulate oblique plane wave incidence when the translational symmetry in the z-direction is broken by a substrate. This is because a plane wave source injects fields that have a constant in plane wavevector $\vec{k}_{\parallel}$ at all frequencies [141]. Since ω and k are related, this results in a frequency dependent incidence angle. This can be solved by performing several simulations for different angles of incidence.

Chapter 4

Island-film theory

The Maxwell equations impose certain constraints on the electric and magnetic fields at either side of the boundary between two different media. Applying vector calculus theorems allows one to identify these boundary conditions [127]. In the absence of any free charges and currents, these boundary conditions state that the tangential components of the E-field and H-field have to be continuous across the boundary. When a plane wave is incident on a flat interface, the boundary condition equations can be solved to yield the standard Fresnel coefficients for light reflection and refraction found in any Optics textbook (e.g. [43, 126, 127]).

However, if there exist idealized surface excess currents or a surface charge density precisely at the interface, the fields become discontinuous and the discontinuity is proportional to these source densities [127].

A typical metasurface is an array of nanoparticles patterned on top of such a boundary between dielectric media (typically air and glass). If the nanoparticles are small, one can model the the metasurface layer as an infinitesimally thin film of polarizable islands [144] and phrase their presence in terms of idealized surface excess quantities. This modifies the field boundary conditions, and solving those allows one to obtain new Fresnel coefficients that include contributions from the nanoparticle inclusions.

This model has been applied to model the optical response of thin layers of plasmonic particles [145–147] and a numerical implementation can be found in [148].

The above works only consider that the particles have an electric polarizability. Thus, those models are insufficient for high refractive index nanoparticles where also the magnetic dipole polarizability is significant. Here, we develop an extension of those models to also include magnetic excitations.

Paper I deals with a metasurface of silicon nanopillars placed on top of a glass substrate and illuminated from the glass side at high angles. This extended island film model was used to express the reflection from this metasurface and it proved to be a useful analytical tool for predicting the perfect absorption phenomenon.

4.1   Modified Fresnel coefficients for magnetic response

We divide space into two regions with refractive index n_1 and n_2, respectively. If we allow for idealized surface excess quantities at the interface, the boundary conditions we will use for the field components tangential to the interface are [126, 148]

$$\hat{z} \times \left(\vec{E}_2 - \vec{E}_1 \right) = \mu_0 \frac{\partial \vec{M}_\parallel^s}{\partial t} \, , \tag{4.1}$$

$$\hat{z} \times \left(\vec{H}_2 - \vec{H}_1 \right) = -\frac{\partial \vec{P}_\parallel^s}{\partial t} \, , \tag{4.2}$$

where we have chosen $\hat{z}$ as a normal vector to the interface directed into medium 1. The quantities $\vec{M}_{\parallel}^s$ and $\vec{P}_{\parallel}^s$ are surface magnetizations and surface polarizations. Note that we have chosen only to include in-plane polarization and magnetization. The choice to neglect the out-of-plane (z) components is definitely justified in the case of metasurfaces with very thin particles, such as plasmonic nanodisks studied in previous works [146, 149]. For the case of the thicker silicon nanopillars studied in Paper I, this approximation is less justified and a model including them would be preferable in terms of accuracy. However, it turns out that the response is dominated by the in-plane polarizabilities and the experiments performed are well described by this model despite the omission of the z-components.

It should be noted that there is no inherent difficulty to include also the out-of-plane response. In fact, such expressions are available for the case of only electric dipole response [144, 148]. However, including out-of-plane in addition to magnetic response would yield significantly more complicated expressions. In order to be able to draw somewhat transparent analytical conclusions, we therefore chose to restrict the analysis to in-plane dipoles.

Each nanoparticle in the metasurface has dipole polarizabilities defined such that its electric and magnetic dipole moments are

$$\vec{p} = \varepsilon_0 \overleftrightarrow{\alpha}_e \cdot \vec{E}_{\text{exc}} \,, \tag{4.3}$$

$$\vec{m} = \overleftrightarrow{\alpha}_m \cdot \vec{H}_{\text{exc}} \,. \tag{4.4}$$

where $\vec{E}_{\text{exc}}$ and $\vec{H}_{\text{exc}}$ are the electric and magnetic fields exciting the particle, respectively. We introduce a particle surface density ρ (units m^{-2}) such that the surface polarization (dipole moment per unit area) and surface magnetization can be written

$$\vec{P}_{\parallel}^s = \varepsilon_0 \rho \alpha_e^{\parallel} \vec{E}_{\text{exc}}^{\parallel} \,, \tag{4.5}$$

$$\vec{M}_{\parallel}^s = \rho \alpha_m^{\parallel} \vec{H}_{\text{exc}}^{\parallel} \,, \tag{4.6}$$

where we assumed that the nanoparticles are isotropic in-plane (cylindrically symmetric) so that the in-plane polarizability tensor is scalar.

It should be noted that if a single-particle polarizability is used in Equations (4.5) and (4.6), any inter-particle coupling is neglected. It is simply assumed that the metasurface response is a density averaged single-particle response. The metasurfaces in Paper I were made using colloidal lithography, which means that the particles have a well-defined nearest neighbour distance (set by the bead size in fabrication) while they lack any long-range order such as periodicity. The fabricated samples were sufficiently sparse so that nearest neighbour interactions were small and the no-coupling approximation was justified.

However, inter-particle coupling can easily be taken into account here by introducing an effective polarizability by either experimental fitting [146] or by using lattice sums and dipole-dipole coupling in the case of periodic arrays [150].

Note also that Equations (4.5) and (4.6) play the role of constitutive relations in this system, and in this step one could introduce magneto-electric coupling. The framework could therefore be adapted to model e.g. chiral metasurfaces.
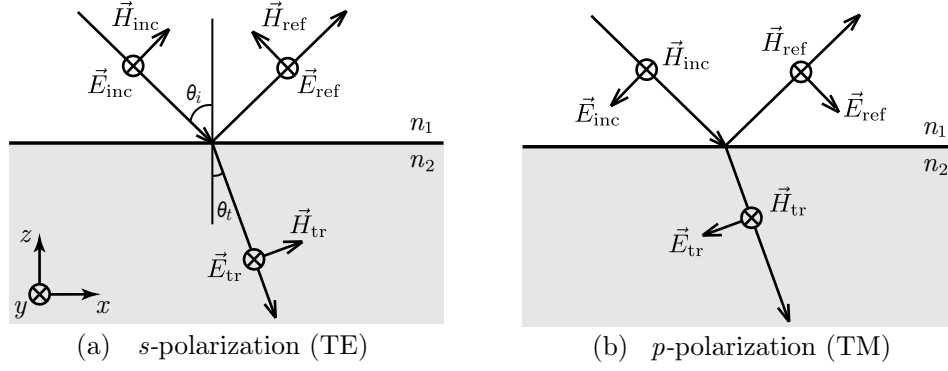
(a) *s*-polarization (TE)   (b) *p*-polarization (TM)

FIGURE 4.1: **Direction of electric and magnetic fields** The chosen convention for the direction of the electric and magnetic fields for **(a)** *s*-polarized and **(b)** *p*-polarized incidence. As usual, $\otimes$ depicts an arrow pointing away from the viewer, into the page.

With the present choices regarding the surface polarization and magnetization, the boundary conditions in Equations (4.1) and (4.2) become

$$\hat{z} \times \left(\vec{E}_2 - \vec{E}_1 \right) = -\mathrm{i}\omega\mu_0\rho\alpha_m^{\parallel}\vec{H}_{\mathrm{exc}}^{\parallel} \, , \tag{4.7}$$

$$\hat{z} \times \left(\vec{H}_2 - \vec{H}_1 \right) = \mathrm{i}\omega\varepsilon_0\rho\alpha_e^{\parallel}\vec{E}_{\mathrm{exc}}^{\parallel} \, , \tag{4.8}$$

where we have assumed a harmonic time-dependence such that $\partial/\partial t \to -\mathrm{i}\omega$.

We now consider a plane wave impinging on the interface from medium 1 so that

$$\vec{E}_{\mathrm{inc}} = \vec{E}^i \mathrm{e}^{-\mathrm{i}p_1 z} \, , \tag{4.9}$$

$$\vec{H}_{\mathrm{inc}} = \vec{H}^i \mathrm{e}^{-\mathrm{i}p_1 z} \, , \tag{4.10}$$

with analogous expressions for the reflected and transmitted fields. Here, p_1 is the z-component of the wavenumber in medium 1, i.e. $p_1 = k_1 \cos\theta_i = n_1 k_0 \cos\theta_i$. When discussing plane wave reflection and refraction at a flat interface, it is customary [43, 127] to express the polarization in a basis of s (TE) and p (TM). There are different ways to choose the direction of the unit vectors as long as E, H, k forms a right handed triad in that order. The chosen convention for the direction of the electric and magnetic fields is shown in Figure 4.1, where for example

$$\vec{E}^i(s) = E^i \hat{y} \, , \qquad \vec{E}^i(p) = -E^i (\cos\theta_i \hat{x} + \sin\theta_i \hat{z}) \, . \tag{4.11}$$

Precisely at the interface, $z = 0$, all fields are in phase and we have $\vec{E}_1 = \vec{E}_{\mathrm{inc}} + \vec{E}_{\mathrm{ref}} = \vec{E}^i + \vec{E}^r$ and $\vec{E}_2 = \vec{E}_{\mathrm{tr}} = \vec{E}^t$ and analogously for the $\vec{H}$-fields. Since the electric and magnetic fields are discontinuous across the infinitesimally thin interface, a reasonable choice for the parallel part of the exciting fields is the mean value of the fields in either medium. The boundary conditions in Equations (4.7) and (4.8) become

$$\hat{z} \times \left[\vec{E}^t - (\vec{E}^i + \vec{E}^r) \right] = \frac{-\mathrm{i}\omega\mu_0\rho\alpha_m^{\parallel}}{2} \left(\vec{H}_{\parallel}^i + \vec{H}_{\parallel}^r + \vec{H}_{\parallel}^t \right) \, , \tag{4.12}$$

$$\hat{z} \times \left[\vec{H}^t - (\vec{H}^i + \vec{H}^r) \right] = \frac{\mathrm{i}\omega\varepsilon_0\rho\alpha_e^{\parallel}}{2} \left(\vec{E}_{\parallel}^i + \vec{E}_{\parallel}^r + \vec{E}_{\parallel}^t \right) \, . \tag{4.13}$$

We can now proceed to solve these boundary conditions to obtain reflection and transmission coefficients for s-polarized (TE) and p-polarized (TM) incidence separately. For each case, the boundary conditions each yield one equation. In analogy with regular reflection, refraction and transmission, we introduce Fresnel coefficients $r^s = E^r/E^i$ and $t^s = E^t/E^i$ and analogously for p-polarization.

The solution to the boundary condition equations results in the following expressions for these modified reflection and transmission coefficients

$$
r^s = \frac{(n_1 \cos\theta_i - n_2 \cos\theta_t)\left(1 - \frac{k_0^2 \rho^2 \alpha_e^\| \alpha_m^\|}{4}\right) - \mathrm{i}k_0 n_1 n_2 \cos\theta_i \cos\theta_t \rho\alpha_m^\| + \mathrm{i}k_0 \rho\alpha_e^\|}{(n_1 \cos\theta_i + n_2 \cos\theta_t)\left(1 - \frac{k_0^2 \rho^2 \alpha_e^\| \alpha_m^\|}{4}\right) - \mathrm{i}k_0 n_1 n_2 \cos\theta_i \cos\theta_t \rho\alpha_m^\| - \mathrm{i}k_0 \rho\alpha_e^\|} ,
$$

$$(4.14)$$

$$
t^s = \frac{2n_1 \cos\theta_i \left(1 + \frac{k_0^2 \rho^2 \alpha_e^\| \alpha_m^\|}{4}\right)}{(n_1 \cos\theta_i + n_2 \cos\theta_t)\left(1 - \frac{k_0^2 \rho^2 \alpha_e^\| \alpha_m^\|}{4}\right) - \mathrm{i}k_0 n_1 n_2 \cos\theta_i \cos\theta_t \rho\alpha_m^\| - \mathrm{i}k_0 \rho\alpha_e^\|} ,
$$

$$(4.15)$$

$$
r^p = \frac{(n_2 \cos\theta_i - n_1 \cos\theta_t)\left(1 - \frac{k_0^2 \rho^2 \alpha_e^\| \alpha_m^\|}{4}\right) + \mathrm{i}k_0 n_1 n_2 \rho\alpha_m^\| - \mathrm{i}k_0 \cos\theta_i \cos\theta_t \rho\alpha_e^\|}{(n_2 \cos\theta_i + n_1 \cos\theta_t)\left(1 - \frac{k_0^2 \rho^2 \alpha_e^\| \alpha_m^\|}{4}\right) - \mathrm{i}k_0 n_1 n_2 \rho\alpha_m^\| - \mathrm{i}k_0 \cos\theta_i \cos\theta_t \rho\alpha_e^\|} ,
$$

$$(4.16)$$

$$
t^p = \frac{2n_1 \cos\theta_i \left(1 + \frac{k_0^2 \rho^2 \alpha_e^\| \alpha_m^\|}{4}\right)}{(n_2 \cos\theta_i + n_1 \cos\theta_t)\left(1 - \frac{k_0^2 \rho^2 \alpha_e^\| \alpha_m^\|}{4}\right) - \mathrm{i}k_0 n_1 n_2 \rho\alpha_m^\| - \mathrm{i}k_0 \cos\theta_i \cos\theta_t \rho\alpha_e^\|} .
$$

$$(4.17)$$

As a sanity check, one can note that these coefficients reduce to the standard Fresnel reflection and transmission coefficients (e.g. [43, 127]) in the absence of any in-plane polarizations ($\alpha_e^\| = \alpha_m^\| = 0$).

The total reflection and transmission from the metasurface is a superposition of several contributions. The first term in the numerator of the reflection coefficients is independent of the particle polarizabilities and has the form of the standard Fresnel coefficients. One can thus loosely think of it as corresponding to the contribution from the bare interface, while the other terms contain the contributions from the scattering of the electric dipoles, magnetic dipoles and their cross-term.

4.1.1 A generalized Kerker condition

As was discussed in Section 2.2, the interference between electric and magnetic dipoles can give rise to highly directional scattering. Of particular note are small particles with only electric and magnetic dipole excitations illuminated by a plane

wave where $\alpha_e = \alpha_m$ gives rise to complete destructive interference in the backward direction.

There is a clear analogy between such single particle scattering and this island-film model. In fact, if we place our metasurface film in vacuum ($n_1 = n_2 = 1$) and consider normal incidence ($\theta_i = \theta_t = 0$), the modified Fresnel reflection coefficients become

$$r^s = -r^p = \frac{\alpha_m^\parallel - \alpha_e^\parallel}{\alpha_m^\parallel + \alpha_e^\parallel} \, . \tag{4.18}$$

Note that the seemingly alarming sign difference between r^s and r^p arises naturally as a consequence of the chosen definition of the direction for the electric fields (see Figure 4.1). At normal incidence, $\vec{E}_{\mathrm{inc}}$ and $\vec{E}_{\mathrm{ref}}$ are chosen to be parallel for s polarized incidence and anti-parallel for p-polarized incidence.

From here, it is clear that $\alpha_m^\parallel = \alpha_e^\parallel$ gives rise to zero reflection in analogy with the first Kerker condition yielding zero backscattering.

For the general case of $n_1 \neq n_2$ and oblique incidence, the condition for zero reflection was derived in Paper I. Assuming that $n_2^3 \cos \theta_t - n_1^3 \cos \theta_i \neq 0$, the relation between the electric and magnetic polarizabilities should be

$$\alpha_m^\parallel = \frac{n_2 \cos \theta_t - n_1 \cos \theta_i}{n_2^3 \cos \theta_t - n_1^3 \cos \theta_i} \alpha_e^\parallel \, . \tag{4.19}$$

This relation is thus a generalized Kerker condition for this particular geometry. Note that between Paper I and this thesis, the definition of α_e is different by a factor of ε.

Chapter 5

Optical forces

The applications for the optical confinement of nanoparticles and the importance of the optical tweezer were discussed in Chapter 1. In this more technical chapter, the specific methods for the calculation of optical forces and trap stability are discussed.

5.1 Maxwell stress tensor

In Chapter 3, we used arguments based on the conservation of energy to calculate the absorption of a particle. The conservation of momentum can give rise to the same type of arguments. In loose terms, we look at the total momentum flux through a closed surface enclosing a particle. If there is a *net* flow of electromagnetic momentum across the surface, the missing momentum has to have been transferred to the particle – a force. The same way that the flow of energy is related to the Poynting vector (Equation (3.12)), one can relate the total change in momentum to the divergence of a quantity called the Maxwell Stress Tensor [127, 151], defined as[†]

$$\vec{\vec{M}} = \frac{1}{2}\varepsilon_0\varepsilon_r \mathrm{Re}\left\{\vec{E}\otimes\vec{E}^* + Z_r^2\vec{H}\otimes\vec{H}^* - \frac{1}{2}\left(|\vec{E}|^2 + Z_r^2|\vec{H}|^2\right)\mathbb{1}\right\}, \qquad (5.1)$$

where ε_r is the relative permittivity of the medium and $Z_r = \sqrt{\mu_0\mu_r/\varepsilon_0\varepsilon_r}$ is the impedance of the medium. We have also assumed a harmonic time-dependence for the fields and taken the time-average. Here, $\otimes$ denotes the dyad product or outer product. Specifically, for column vectors $\vec{u}$ and $\vec{v}$, we have $\vec{u}\otimes\vec{v} = \vec{u}\vec{v}^T$. If we put a closed surface S around a particle, the optical force experienced by that particle is given by [127, 151, 153]

$$\vec{F} = \int_S \mathrm{d}A\,\vec{\vec{M}}\cdot\hat{n}, \qquad (5.2)$$

where $\hat{n}$ is an outward unit normal to the surface S. This expression is very general, and can be applied if the total electric and magnetic fields are known on any closed surface around the particle. This follows from the fact that $\nabla\cdot\vec{\vec{M}} = 0$ in a region where there are no sources, and the surface S can thus be deformed arbitrarily provided the deformation does not hit any sources. The method is thus suitable for implementation in FDTD on a Cartesian grid, where the fields are typically monitored on box-shaped surfaces (Chapter 3).

    If the electric and magnetic fields are defined in a basis of spherical multipoles, in the language of Chapter 2, the force can be calculated analytically [153, 154]. The

---

[†]There sometimes arises discussion with regards to the definition of the momentum of light in a medium, referred to as the "Minkowski-Abraham dilemma". However, we will refrain from entering this discussion and simply employ the Minkowski definition. The interested reader is referred to a recent review [152].

time-averaged optical force in the z-direction is given by

$$
F_z = \frac{\varepsilon_0 \varepsilon_r}{2k^2} \Bigg[\sum_{\tau \ell m} \mathrm{Im} \left\{ a^*_{\tau,\ell+1,m} b_{\tau \ell m} + b^*_{\tau,\ell+1,m} a_{\tau \ell m} + 2 b^*_{\tau,\ell+1,m} b_{\tau \ell m} \right\} K_{\ell m}
$$
$$
- \sum_{\ell m} \mathrm{Re} \left\{ a^*_{1 \ell m} b_{2 \ell m} + b^*_{1 \ell m} a_{2 \ell m} + 2 b^*_{1 \ell m} b_{2 \ell m} \right\} \frac{m}{\ell(\ell+1)} \Bigg] , \qquad (5.3)
$$

where

$$
K_{\ell m} = \frac{\sqrt{\ell(\ell+1)}}{\ell+1} \sqrt{\frac{(\ell+m+1)(\ell-m+1)}{(2\ell+1)(2\ell+3)}} , \qquad (5.4)
$$

and k is the wavenumber in the medium. Similar expressions for the in-plane forces (F_x and F_y) can be found in Ref. [153].

5.2 T-matrix method

In general, the scattered field coefficients $b_{\tau \ell m}$ are related to the the incident wave via a *Transition matrix*, or T-matrix, as [125]

$$
\vec{b} = \overleftrightarrow{T} \vec{a} , \qquad (5.5)
$$

or as the explicit sum

$$
b_{\tau \ell m} = \sum_{\tau' \ell' m'} T_{\tau' \ell' m' \tau \ell m} \, a_{\tau' \ell' m'} . \qquad (5.6)
$$

The problem of determining the optical forces (and any other optical property) is reduced to finding this T-matrix for the particle of interest. The incident wave, for this thesis work, is either a plane wave or a focused laser beam.

Focused beam

A focused laser beam can be expressed in an angular spectrum representation, i.e. a superposition of plane waves. The methodology, which will not be repeated in detail here, is based on the procedure outlined by Richards and Wolf [155] and is also treated in Refs. [81, 151]. A plane wave is incident on a lens characterized by a numerical aperture (NA). The field is then transmitted through the lens and expressed in spherical coordinates on a reference sphere in the far-field, as $\vec{E}_{\mathrm{far}}(\theta, \varphi)$. The expression for the field in the focus region is obtained through wave propagation of $\vec{E}_{\mathrm{far}}(\theta, \varphi)$, namely [81, 151]

$$
\vec{E}_{\mathrm{beam}}(x, y, z) = \frac{\mathrm{i} k f \mathrm{e}^{-\mathrm{i} k f}}{2\pi} \int_0^{\theta_{\max}} \int_0^{2\pi} \vec{E}_{\mathrm{far}}(\theta, \varphi) \, \mathrm{e}^{\mathrm{i} k_z z} \mathrm{e}^{\mathrm{i}(k_y y + k_x x)} \, \sin\theta \mathrm{d}\theta \mathrm{d}\varphi , \qquad (5.7)
$$

where $k = n_t k_0$ is the wavenumber in the medium *after* the lens, f is the radius of the reference sphere and $\theta_{\max}$ is set by the numerical aperture of the lens through $\mathrm{NA} = n_t \sin\theta_{\max}$. For a sketch of the illumination geometry, see e.g. Figure 3.7 in Ref. [81].

Finally, assuming our spherical wave expansion of the incident field according to Equation (2.1),

$$\vec{E}_{\text{inc}}(\vec{r}) = \sum_{\tau\ell m} a_{\tau\ell m}\, \vec{\psi}_{\tau\ell m}^{(j)}\;, \tag{5.8}$$

we can find the expansion coefficients for the focused beam at a particular spatial location (x, y, z) through

$$a_{1\ell m}(x, y, z) = \frac{1}{j_\ell(kr)} \int_\Omega \vec{X}_{\ell m}^* \cdot \vec{E}_{\text{beam}}(x, y, z)\, \mathrm{d}\Omega\;, \tag{5.9}$$

and similarly

$$a_{2\ell m}(x, y, z) = \frac{\mathrm{i}Z_r}{j_\ell(kr)} \int_\Omega \vec{X}_{\ell m}^* \cdot \vec{H}_{\text{beam}}(x, y, z)\, \mathrm{d}\Omega\;, \tag{5.10}$$

where Z_r is the impedance of the medium after the lens. Here, $\vec{H}_{\text{beam}}$ is obtained from the Maxwell curl equation and we have used the orthogonality relations of the spherical basis functions (Appendix A).

Determining the T-matrix

As we saw in Chapter 2, the T-matrix is completely diagonal for a spherical particle and Equation (5.6) reduces to

$$b_{\tau\ell m} = t_{\tau\ell}\, a_{\tau\ell m}\;. \tag{5.11}$$

For structures other than spheres, the determination of the T-matrix is more involved. In the method outlined in Ref. [125], the surface of the particle is parametrized and the T-matrix is obtained by matching the expression of the fields on either side of that surface. For such computations, the symmetry of the particle is very important. For instance, for a particle where axial symmetry is preserved (such as a spheroid or a cylindrical disk), the T-matrix will be diagonal in the axial number m, but the response will in general mix different multipole orders ℓ as well as the different multipole types τ. Moreover, if the particle is symmetric under inversion ($r \to -r$), multipole orders with different parity will not mix. For example, electric dipoles will couple to magnetic quadrupoles, but not magnetic dipoles.

It is worth mentioning that the T-matrix is a property of the scatterer, independent of its spatial location. This means that for a calculation involving the optical forces in different parts of the focused beam, the T-matrix need only be computed once (per frequency).

5.3 Dipole approximation

For very small particles, the response is dominated by the electric dipole response. A common way to calculate the optical force experienced by such a particle is to express the dipole moment in terms of the Lorentz force on a charge q moving with a velocity $\vec{v}$, namely $\vec{F} = q\big(\vec{E}(\vec{r}) + \vec{v} \times \vec{B}(\vec{r})\big)$ [127]. Through manipulations involving the Maxwell equations (see e.g. [151]), one can write the time-averaged force as a

sum of a gradient force $\vec{F}_g$ and a radiation pressure $\vec{F}_p$ [†] [111, 151, 156], with

$$\vec{F}_g = \frac{\varepsilon_0 \varepsilon_r}{4} \mathrm{Re}\{\alpha_e\} \nabla |\vec{E}|^2 \,, \qquad \vec{F}_p = \frac{k}{c_0} \mathrm{Im}\{\alpha_e\} \vec{S} \,, \tag{5.12}$$

where $\vec{S} = \frac{1}{2}\mathrm{Re}\{\vec{E} \times \vec{H}^*\}$ is the time-averaged Poynting vector. Here, α_e is the electric dipole polarizability which defines the dipole moment in terms of the incident field according to $\vec{p} = \varepsilon_0 \varepsilon_r \alpha_e \vec{E}$. In order to get the right results, this polarizability cannot simply be a quasi-static approximation, it needs to be properly radiation corrected. However, for a spherical particle, it can be noted that it is not strictly necessary to add such corrections artifically since the polarizability can be expressed through the T-matrix elements (or Mie coefficients) as [83, 157]

$$\alpha_e = -\mathrm{i}\frac{6\pi}{k^3} t_{21} \,. \tag{5.13}$$

However, the simpler quasi-static expressions with radiation correction can sometimes be useful for analytical insights.

A similar treatment can be applied to the force on a magnetic dipole and the optical forces on particles exhibiting electric and magnetic dipole response have been treated in Refs. [123, 156]. In particular, the influence of interference between the electric and magnetic dipoles on the radiation pressure in a plane wave is discussed.

Higher order multipoles

In general, the contribution to the optical force from a certain multipole can be obtained by only including that particular scattering coefficient b in the expression for the optical force. For example, the axial optical force (F_z) on an *electric* dipole can be calculated from Equation (5.3) by only keeping b_{21m}. In other words, fixing all magnetic multipoles ($b_{1\ell m}$) and higher electric multipole orders ($b_{2\ell m}$, with $\ell > 1$) to zero. This method was used in Paper III to determine the multipolar contributions to the optical force on silicon nanoparticles. In particular, the interference between the electric and magnetic dipole excitations associated with the first Kerker condition (discussed in Chapters 1 and 2) was investigated through comparing the optical force stemming from the dipolar contributions.

5.4 Axial forces and trap stability

The total three-dimensional optical force acting on a particle is not conservative and so a proper potential cannot be defined. However, for three-dimensional optical confinement, the lateral restoring forces are much greater than the axial ones owing to the radiation pressure in the axial direction. Thus, the work required to bring the particle out of the trap along the optical axis is the limiting factor for a stable 3D trap. Therefore, in Papers III and VI, the three-dimensional trap stability was estimated by

$$W_{3D} = -\int_{z_0}^{z_r} F_z \, \mathrm{d}z \,, \tag{5.14}$$

[†]Technically, the total optical force also contains a third term proportional to $\mathrm{Im}\{\alpha_e\}\nabla \times (\vec{E} \times \vec{E}^*)$, known as the "spin-curl force". This force is associated with gradients in the polarization of the field and is typically small enough compared to the other forces to be neglected [111, 151].
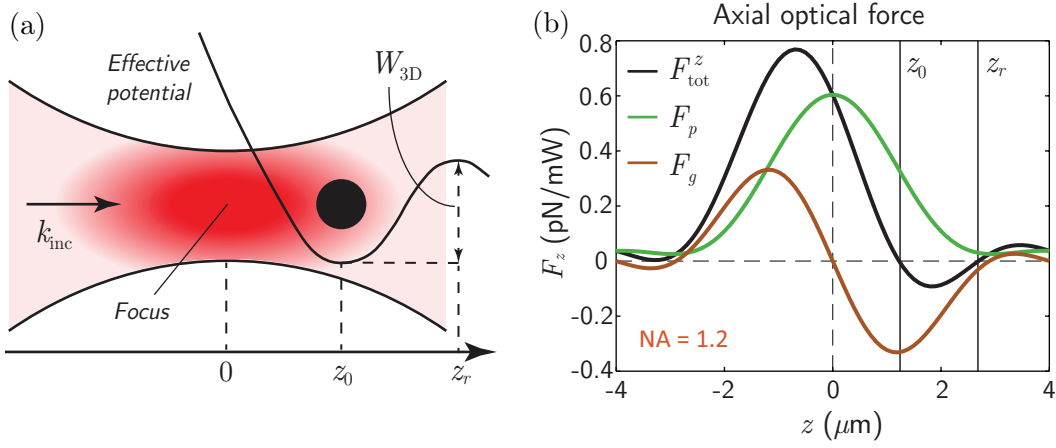
FIGURE 5.1: **Axial optical forces on a silicon sphere in a focused laser beam. (a)** Sketch of the illumination conditions. The beam propagation direction is along z, with $z = 0$ at the focus. **(b)** Axial optical force, F_z along the optical axis decomposed into radiation pressure (green) and gradient force (brown).

where z_0 is the particle equilibrium position in the trap and z_r is the location where the optical force becomes repulsive (Figure 5.1(a)).

The terms radiation pressure and gradient force are typically associated with the dipole approximation discussed the previous section. However, insight into the optical force can be gained by borrowing these expressions and extending them to deal with particles exhibiting higher order response. Consider a laser beam like the one sketched in Figure 5.1(a), where the focus is at $z = 0$. The beam intensity is symmetric in z and the radiation pressure is always directed along the optical axis. Therefore, F_p is symmetric in z. Meanwhile, as the particle is displaced from the focus, it experiences a restoring force towards regions of higher intensity (c.f. Equation (5.12)). As a result, the gradient force F_g is anti-symmetric in z.

An example of an axial force calculation is shown in Figure 5.1(b). The optical force (F_{tot}^z) was calculated using the T-matrix formalism described in Section 5.2 for a spherical silicon particle with radius $a = 127\,\text{nm}$. The medium after the lens is water ($n_t = 1.33$). The laser wavelength used is $\lambda = 1064\,\text{nm}$ and the beam is focused through a lens with numerical aperture NA = 1.2 (water-immersion objective). The total axial force is displayed in Figure 5.1(b), along with the radiation pressure and gradient forces decomposed according to

$$F_p(z) = \frac{F_{\text{tot}}^z(z) + F_{\text{tot}}^z(-z)}{2} \ , \qquad F_g(z) = \frac{F_{\text{tot}}^z(z) - F_{\text{tot}}^z(-z)}{2} \ . \tag{5.15}$$

The radiation pressure is at its strongest in the focus of the beam where the intensity is maximized. The restoring force on the other hand, is maximized where the intensity gradient is at its largest. The axial equilibrium position is thus slightly displaced downstream from the focus. The forces are normalized to the total incident power in the beam, P_{in}.

Chapter 6

Weak coupling to emitters

An introductory discussion about the coupling of subwavelength emitters to high index dielectric structures can be found in Chapter 1. This chapter is instead aimed at introducing the technical details involved in calculating the decay rate enhancement of emitters placed in the vicinity of a resonator.

The strength of coupling between an emitter and, for example, a nanoantenna can be characterized by the rate of energy transfer between the two systems. If this energy transfer occurs on time-scales that are faster than any energy dissipation, the two systems are said to be "strongly coupled". In other words, a single photon excitation can be transferred between the emitter and the nanoantenna several times before it is eventually absorbed or emitted. This problem cannot be treated by weak perturbation theory, and more sophisticated quantum models are needed (see e.g. [158]). However, a molecule or quantum dot placed near a resonant high-refractive index nanoparticle is typically weakly coupled to the electromagnetic modes of the particle and the work in this thesis relates to this weak coupling limit. In this limit, the emitter frequency is unaffected by the environment and, as it turns out in the next section, the coupling can be estimated by classical electrodynamics.

6.1 Purcell effect

In a quantum electrodynamics picture, an emitter is typically considered as a two-level system with a ground state $|g\rangle$ and excited state $|e\rangle$, separated by an energy $\hbar\omega_0$. An emitter prepared in its excited state $|e\rangle$ will couple to the optical states around it and will undergo spontaneous emission. The emitter couples to a *continuum* of modes (a continuum of emission directions). Through a quantum mechanical calculation using a weak perturbation [158], the spontaneous emission of such an emitter can be characterized by Fermi's golden rule (e.g. [81, 158])

$$\gamma = \frac{\pi\omega_0}{3\hbar\varepsilon_0}|\vec{d}|^2\rho(\vec{r}_0, \omega_0) \, ,\tag{6.1}$$

where $\vec{d}$ is the transition dipole moment associated with the transition between the two levels ($\vec{d} = \langle e|q\boldsymbol{r}|g\rangle$, where q is the charge and $\boldsymbol{r}$ is the quantum mechanical position operator). The quantity $\rho(\vec{r}_0, \omega_0)$ is called the local density of states. It is evaluated at the location $\vec{r}_0$ of the emitter and is frequency dependent. For an emitter placed in free space, the spontaneous emission is characterized by a rate

$$\gamma_0 = \frac{\omega_0^3}{3\pi\hbar\varepsilon_0 c_0^3}|\vec{d}|^2 \, .\tag{6.2}$$

However, as was realized by Purcell [77], when the emitter is brought into the proximity of a cavity, this free space decay rate gets modified since the density of states in Equation (6.1) changes.

To get a sense of the scale of this modification, it is convenient to introduce the dimensionless relative decay rate γ/γ_0. In the context of a two-level emitter coupled to a single mode in a closed resonator, this relative decay rate is called the Purcell factor F_p and is proportional to Q/V [77], where Q is the quality factor of the resonance and V is its mode volume. The concept of mode volume can be extended for coupling to multiple modes, but is in general not straightforward to define for open resonator systems, like nanoparticles [159]. If one expands the Green's function in terms of eigenmodes in the cavity, an the modified decay rate can can be found in terms of its imaginary part [80, 81, 159]

$$\frac{\gamma}{\gamma_0} = \frac{6\pi c_0}{\omega_0} \mathrm{Im}\{\hat{d} \cdot \overleftrightarrow{G}(\vec{r}_0, \vec{r}_0, \omega_0) \cdot \hat{d}\} \,, \tag{6.3}$$

where $\hat{d}$ is a unit vector in the direction of the transition dipole moment. Note that the alignment is the only property of the transition dipole moment that enters this expression. The enhancement of spontaneous decay is thus not dependent on the strength of the emitter, but is a property of the environment. This is not the case in a strongly coupled system, where the strength of the transition dipole moment is very important.

The quantum mechanical problem above can be compared to the classical problem of a radiating electric dipole [81]. The rate of energy dissipation of a current distribution inside a volume V is given by [127]

$$P = \frac{\mathrm{d}W}{\mathrm{d}t} = -\frac{1}{2}\mathrm{Re} \int_V \mathrm{d}^3r \, \vec{j}^*(\vec{r}) \cdot \vec{E}(\vec{r}) \,. \tag{6.4}$$

For a dipole with dipole moment $\vec{p}$ located at $\vec{r} = \vec{r}_0$, oscillating harmonically with frequency ω_0, we have $\vec{j}(\vec{r}) = -\mathrm{i}\omega_0 \vec{p}\,\delta^{(3)}(\vec{r} - \vec{r}_0)$, and

$$P = \frac{\omega_0}{2}\mathrm{Im}\{\vec{p}^* \cdot \vec{E}(\vec{r}_0)\} \,. \tag{6.5}$$

Note that $\vec{E}(\vec{r}_0)$ is the *total* field at the dipole location. It thus contains the direct dipole field as well as any secondary fields scattered back from an inhomogeneous environment. The total electric field due to the dipole is given in terms of the Green's function as (c.f. Equation (B.4))

$$\vec{E}(\vec{r}) = \omega_0^2 \mu_0 \, \overleftrightarrow{G}(\vec{r}, \vec{r}_0, \omega_0) \cdot \vec{p} \,, \tag{6.6}$$

where $\overleftrightarrow{G}(\vec{r}, \vec{r}_0)$ is not necessarily the homogeneous Green's function. The dissipated power becomes

$$P = \frac{\omega_0^3 \mu_0}{2}|\vec{p}|^2 \, \mathrm{Im}\{\hat{p} \cdot \overleftrightarrow{G}(\vec{r}_0, \vec{r}_0, \omega_0) \cdot \hat{p}\} \,. \tag{6.7}$$

In free space, time-averaged power radiated by the dipole is [127]

$$P^0_{\mathrm{rad}} = \frac{\omega_0^4}{12\pi\varepsilon_0 c_0^3}|\vec{p}|^2 \,. \tag{6.8}$$

Normalizing Equation (6.7) by the free-space radiation rate, we obtain

$$\frac{P}{P_{\text{rad}}^0} = \frac{6\pi c_0}{\omega_0} \operatorname{Im}\{\hat{p} \cdot \vec{\vec{G}}(\vec{r}_0, \vec{r}_0, \omega_0) \cdot \hat{p}\} \ , \tag{6.9}$$

which is an expression identical to (6.3), establishing a very useful quantum-classical analogue. In this weak coupling regime (Purcell regime), the modification to the spontaneous emission can be modelled by a classical dipole calculation [81].

6.2 Non-radiative decay

If an emitter is located in an environment with absorptive loss, some of the emitted photons will be absorbed. Seen from the outside, these absorbed photons are lost. In most practical applications, it is the enhancement of radiation to the far-field that is interesting. One therefore typically distinguishes between radiative and non-radiative decay rate enhancements for the whole system.[†] The dissipated power P in Equation (6.7) includes both radiative and non-radiative decay. We define the total decay rate enhancement as

$$F_{\text{tot}} = F_{\text{rad}} + F_{\text{nr}} = \frac{P_{\text{rad}} + P_{\text{nr}}}{P_{\text{rad}}^0} \ . \tag{6.10}$$

The non-radiative decay rate enhancement corresponds to the emission coupling to loss channels in the environment. For instance, an emitter placed in close proximity to a nanoantenna with non-zero absorption.

6.3 Calculation of the decay rate enhancements

In this thesis work, the inhomogeneous environments that the emitter couples to consists of single nanoparticles made of silicon. In this case, there is a clear boundary between the system and a surrounding homogeneous medium. Therefore, in order to determine the decay rate enhancement F_{tot} through a classical calculation, a method similar to the calculation of absorption and scattering in Section 3.3.1 can be employed (the set-up of the method is sketched in Figure 6.1). From Poynting's theorem, the total power dissipated (Equation (6.4)) can be calculated from the Poynting vector [126]. Normalizing this power to the analytical expression for P_{rad}^0 (Equation (6.8)), we obtain the total decay rate enhancement

$$F_{\text{tot}} = \frac{P}{P_{\text{rad}}^0} = \frac{1}{P_{\text{rad}}^0} \int_{S_{\text{I}}} dA\, \vec{S} \cdot \hat{n} \ , \tag{6.11}$$

where S_{I} is a small closed surface enclosing *only* the dipole source (see Figure 6.1(b)). The field on that spherical surface will be a superposition of the direct dipole field and the secondary field, scattered by the environment.

The radiative decay rate enhancement on the other hand is obtained through the net electromagnetic energy that escapes to the far-field. In other words, the power radiated through a closed surface S_{II} enclosing both the dipole source and its

---

[†]For simplicity, we restrict the discussion to emitters with internal quantum efficiency $q_i = 1$, i.e. an emitter in the excited state will always emit a photon, there are no internal non-radiative channels. In reality, what is seen by a far field observer should be characterized by a quantum yield of the whole system which takes the potential for $q_i < 1$ into account.
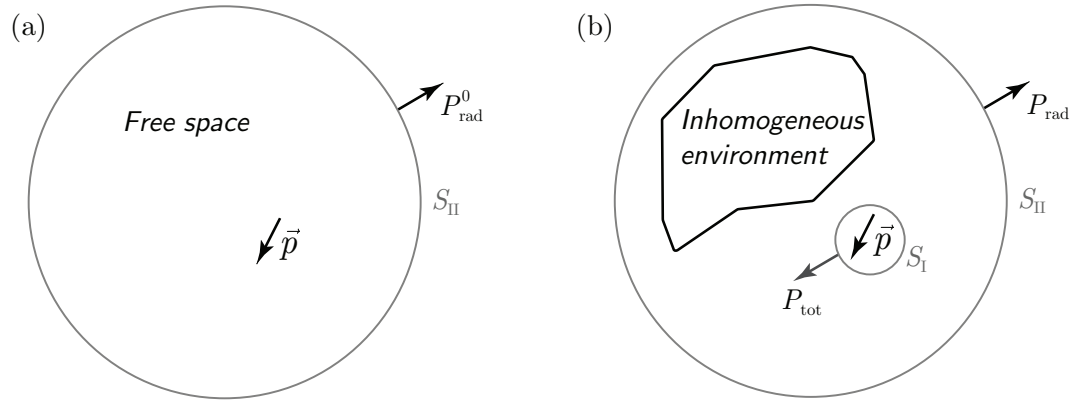
FIGURE 6.1: **Determining the decay rate enhancement of a dipolar emitter. (a)** A dipole source $\vec{p}$ in free space will radiate a power P_{rad}^0 to the far field. **(b)** The same dipole source is placed in an inhomogeneous environment. The total power dissipated is obtained from integration of the Poynting vector in a small closed surface S_{I} enclosing only the dipole. The power radiated into the far-field is obtained by integration on a surface S_{II} enclosing both the dipole source and the scatterer.

environment,

$$F_{\text{tot}} = \frac{1}{P_{\text{rad}}^0} \int_{S_{\text{II}}} \mathrm{d}A\, \vec{S} \cdot \hat{n} \ . \tag{6.12}$$

As discussed in Chapter 1, since high-refractive index dielectric nanostructures support modes of both electric and magnetic character, interest has been sparked in the Purcell effect associated with magnetic dipole transitions. The treatment in Section 6.1 can be performed in an analogous fashion for magnetic emitters (see e.g. [82]). The interaction Hamiltonian in the quantum mechanical treatment is $\boldsymbol{H}_{\text{I}}^m = -\boldsymbol{m} \cdot \boldsymbol{B}$ in place of $\boldsymbol{H}_{\text{I}}^e = -\boldsymbol{d} \cdot \boldsymbol{E}$ while the Green's function is that of a magnetic dipole, $\vec{m}$. This leads to a similar classical-quantum analogue, namely that

$$\frac{\gamma^m}{\gamma_0^m} = \frac{P^m}{P_{\text{rad}}^{0,m}} \ , \tag{6.13}$$

and the decay rate enhancement for a magnetic emitter in a given environment can be found from a classical calculation with a magnetic dipole source.

The method discussed here was used in Paper IV to determine the electric and magnetic decay rate enhancement for emitters placed inside the pores of quasi porous silicon disks. The classical dipole calculations were implemented in FDTD using an electric or a magnetic dipole source.

It should be noted that in the language of Chapter 2, the decay rate enhancement can be obtained analytically for spherical particles (see e.g. [82]). The methodology involves expressing the dipole source in terms of multipole coefficients, $b_{\tau,1,m}$ (Appendix B). The radiative decay rate enhancement can be found through a computation of the energy escaping to the far-field (similar to Appendix E). The total decay rate enhancement is obtained from a small spherical surface enclosing only the dipole source.

Chapter 7

Concluding remarks

7.1 Discussion of appended papers

The appended papers are summarized in their respective abstracts and introductions. In this section, the appended papers are discussed in a way that involves some more personal reflections.

Paper I

Large-scale silicon nanophotonic metasurfaces with polarization independent near-perfect absorption.

This paper was the result of one of the first projects where the hole-mask colloidal lithography method was used to fabricate silicon metasurfaces. The metasurfaces were illuminated in a total-internal-reflection geometry and the reflected light was measured. For a certain incident angle and light wavelength, the interference between interface reflection and scattering from magnetic and electric dipole excitation gave rise to almost complete light absorption for unpolarized light.

The effect was modelled using an extension I developed of the island-film theory wherein the magnetic response of the nanoparticles was also included. From this analytical formalism, conditions were derived for the electric and magnetic polarizabilities such that the metasurface exhibits this perfect absorption. The particle shapes were estimated from SEM images and FDTD was used to calculate the near-field distributions for a single particle in the presence of the glass interface. From these near-fields, the in-plane electric and magnetic dipole polarizabilities were calculated and used in the analytical model to obtain good agreement with experimental data.

One of the most straightforward modifications to the model from hindsight is to use the exact expressions for the electric and magnetic dipole moments (e.g. Equation (2.32) instead of Equation (2.31)). Since the particles in these metasurfaces are quite large, this modification would likely result in a better agreement with experiment while not introducing any significant complexity.

Paper II

Metasurfaces and colloidal suspensions composed of 3D chiral Si nanoresonators.

In this paper, my contributions were of a more supporting nature since the project was mainly fabrication oriented. The main result of the paper was the demonstration of a fabrication method that allows for the large-scale fabrication of metasurfaces as well as colloidal suspensions of silicon nanoparticles of a specific, well-defined, morphology. The method was applied to study structures with

three-dimensional chirality. The metasurfaces and colloidal solutions were characterized both with extinction measurements and through measurement of the circular dichroism. It was also demonstrated that the silicon particles could be optically trapped and manipulated using a laser wavelength of $\lambda = 1064$ nm.

The structures were 3D modeled from SEM pictures and then imported into the FDTD software and their optical response was calculated. Due to the low particle symmetry, the analysis of the near-fields and the origin of the circular dichroism is complicated and the paper offers a phenomenological explanation. More sophisticated modelling of the chiral response could be performed via illumination with standing waves (see e.g. [160]), isolating the electric and magnetic responses. While potentially interesting from a theoretical point of view, such a treatment would overcomplicate this particular study which is more focused on the fabrication.

Paper III

Directional scattering and multipolar contributions to optical forces on silicon nanoparticles in focused laser beams.

This paper is focused on the optical forces on silicon nanoparticles. Since optical force is all about transfer of momentum from the light beam to a particle, the direction of scattering has a major effect on the forces. Therefore, the directional scattering properties of silicon nanoparticles, in particular the first Kerker condition, was investigated in the context of optical trapping. It was found that while zero-backscattering implies an optimal radiation distribution, the overall scattering response is so large in the vicinity of the resonances that there is still considerable radiation pressure. As a result, for sphere sizes slightly larger than the "Kerker size", three-dimensional confinement is no longer possible. Moreover, the trap stability for spheroidal particles was calculated, showing a similar size dependence. The size limit for trapping of these non-spherical particles is similar to their spherical counterparts.

Paper IV

Electromagnetic energy distribution in resonant quasi porous silicon nanostructures.

This study exploits a central property of resonant high-index dielectric nanoparticles, namely that the resonantly enhanced near-fields are mostly confined to the particle interior. The most efficient coupling is thus expected for emitters placed inside the nanoantenna. A promising approach to put them there is to fabricate the nanoantenna of porous silicon, thus making it permeable. The electromagnetic energy density available in the pores was studied and interpreted as an estimate for this coupling strength. The discussion revolves around emitters of both electric and magnetic type, since the excitation of both electric and magnetic multipolar resonances in these structures promotes the coupling to normally suppressed magnetic transitions.

FDTD was used for the simulations of the dipolar decay rate enhancements. Analytical methods based on Mie theory could be employed as a complement. In particular, for small pore sizes, the FDTD method is sensitive to the meshing. In addition, the enhanced non-radiative decay rate near the edges of the pores is very sensitive to a correct fitting of the dielectric function. Although not included in the paper, I derived expressions for the total and radiative decay rate enhancements for a dipole at the center of a core-shell sphere which gave similar qualitative behaviour as Figure 5 in the paper when applied to a silicon sphere with a vacuum "pore".

Paper V

Solar harvesting based on all-dielectric perfect absorbing metasurfaces.

The concept of enhanced absorption driven by destructive interference of reflected light from silicon metasurfaces was adapted from its implementation in Paper I to a metasurface-on-a-mirror geometry. In this implementation, the transmitted light reflects back by a metallic mirror and it interferes with the direct reflection. Destructive interference concentrates the incident light into the resonant silicon nanoparticles – enhancing the absorption of the excited modes. The nanoparticles composing the metasurface were composed of hydrogenated amorphous silicon and were contacted at the top and bottom by transparent conductive oxides. This design allows the conversion of the absorbed light energy to a photocurrent: a solar cell. The multipolar modes and the interference criterion was tuned to lie in a spectral region where the intrinsic silicon absorption is low, increasing the absorption overlap with the solar spectrum.

This study was a collaboration with a research group at Delft University in The Netherlands with more experience in solar cell research. Their expertise was instrumental in proposing the design of a realistic device based on this geometry. They provided insights in material choices and their data on the optical properties of those materials as well as simulation methods for theoretically predicting the extracted photocurrent.

Paper VI

Thermal effects and trap stability for nanoparticle spheres in an optical trap.

Since the demonstration that metallic nanoparticles with plasmonic properties can be stably trapped in 3D, there has been enormous interest in applications thereof. Combining the unique properties of plasmonic nanoparticles with optical manipulation is an attractive prospect. Similarly, interest has arisen for the optical trapping and manipulation of resonant high-index dielectric nanoparticles. In the quest for a small probe particle to measure nanoscopic forces or temperatures or a handle for performing work on the nanoscale, the material of the particle is very important. One needs a strong optical response but with a minimal influence on the environment. In particular, the photothermal heating associated with metallic particles can be problematic for biological or sensitive chemical applications.

This work aims to make a material comparison for optical trapping of nanoparticles at a few commonly employed laser wavelengths in optical tweezer research. It is intended to function as a useful guide for the material choice for a specific application. To see the materials compared side-by-side and simulated in identical conditions will hopefully prove helpful.

7.2 Outlook

Resonant dielectric nanoparticles are a promising platform for engineering light-matter interactions at the nanoscale. The field has matured in the last decade as researchers have mapped out many useful applications. This thesis has focused on a few different aspects of the research field. The interesting resonant properties of single particles were studied in terms of near-field coupling to subwavelength emitters as well as for optical trapping. The behaviour of collections of particles was studied in terms of metasurfaces with enhanced absorption or chiral response.

Research in plasmonics exploded with the advent of reproducible colloidal fabrication methods and a wealth of opportunities opened up. The same might be expected for silicon and other high-index dielectric structures. Fabrication methods (such as the one discussed in Paper II) that enable fabrication of colloidal suspensions of high-index dielectric particles will be instrumental in the years to come.

The optical trapping and confinement of silicon or other high-index dielectric particles has not been explored in exhausting detail. It is clear (e.g. from Paper III and VI) that the trapping laser energy needs to be lower than that of any of the Mie resonances in a silicon sphere in order for three-dimensional confinement to be possible. However, trapping with a low energy laser beam while using other light sources to probe and interact with the rich resonance structure could provide interesting opportunities.

The coupling between subwavelength emitters and the resonant response of high-index nanoparticles is very promising for a multitude of applications. The architecture of a permeable porous nanoantenna discussed in Paper IV could find use as a sensor. In particular, the reduced emission quenching associated with the lower optical loss in silicon compared to metallic nanoparticles is crucial in this scenario. This is particularly important for the magnetic dipole emission enhancement where quenching is almost absent even for very short distances between emitter and nearby interfaces. For example, one could envision exploiting the magnetic dipole transition in Eu^{3+} along with its affinity to bind to fluoride ions for use as a type of fluorine sensor.

It is my hope that my contributions will be useful for research to come and that I have made meaningful additions to our overall understanding in terms of *"Optimization of resonant all-dielectric nanoparticles for optical manipulation and light management."*

Appendices

Appendix A

Spherical basis functions

Due to various conventions used in different books and articles in the literature, there can sometimes arise confusion as to what one uses. This is especially true for normalization. The objective of this appendix is to give the definitions of the spherical functions that are utilized in the main thesis text, without making said text unreadable.

Angular part

In this thesis, the conventions for the spherical harmonics, both scalar and vector, follow that of Jackson [127]. The scalar spherical harmonics are given by

$$Y_{\ell m}(\theta, \varphi) = \sqrt{\frac{2\ell + 1}{4\pi} \frac{(\ell - m)!}{(\ell + m)!}} P_\ell^m(\cos\theta) \mathrm{e}^{\mathrm{i}m\varphi} \ , \tag{A.1}$$

where $P_\ell^m(\cos\theta)$ are associated Legendre functions. From these, the vector spherical harmonics are defined as

$$\vec{X}_{\ell m}(\theta, \varphi) = \frac{1}{\sqrt{\ell(\ell + 1)}} \vec{L} Y_{\ell m}(\theta, \varphi) \ , \tag{A.2}$$

where $\vec{L}$ is the angular momentum operator,

$$\vec{L} = -\mathrm{i}(\vec{r} \times \nabla) = -\mathrm{i}\left(\hat{\varphi} \frac{\partial}{\partial \theta} - \frac{\hat{\theta}}{\sin\theta} \frac{\partial}{\partial \varphi} \right) \ . \tag{A.3}$$

For reference, the vector spherical harmonics are explicitly (in all their normalized glory) given by

$$\begin{aligned} \vec{X}_{\ell m}(\theta, \varphi) = {} & \sqrt{\frac{2\ell + 1}{4\pi\ell(\ell + 1)}} \sqrt{\frac{(\ell - m)!}{(\ell + m)!}} \\ & \times \left(\frac{m P_\ell^m(\cos\theta)}{\sin\theta} \hat{\theta} - \mathrm{i} \frac{\partial P_\ell^m(\cos\theta)}{\partial \theta} \hat{\varphi} \right) \mathrm{e}^{\mathrm{i}m\varphi} \ , \end{aligned} \tag{A.4}$$

One thing worth noting in Eq. (A.4) is that it has no radial component. This is useful in various calculations since $\hat{r} \times (\hat{r} \times$ and $\hat{r}\cdot$ are commonplace.

The vector spherical harmonics are ortho-normalized with respect to integration over a solid angle. That is to say,

$$\int_S \mathrm{d}\Omega \, \vec{X}_{\ell'm'}^* \cdot \vec{X}_{\ell m} = \delta_{\ell\ell'}\delta_{mm'} \ , \tag{A.5}$$

and

$$\int_S \mathrm{d}\Omega \left(\hat{r} \times \vec{X}^*_{\ell'm'}\right) \cdot \left(\hat{r} \times \vec{X}_{\ell m}\right) = \delta_{\ell\ell'}\delta_{mm'} \, , \tag{A.6}$$

as well as,

$$\int_S \mathrm{d}\Omega \, \vec{X}^*_{\ell'm'} \cdot \left(\hat{r} \times \vec{X}_{\ell m}\right) = 0 \, . \tag{A.7}$$

Radial part

The radial part of the wave equation is solved by the spherical functions of various types (spherical Bessel functions j_ℓ, spherical Neumann functions n_ℓ and spherical Hankel functions $h_\ell^{(1,2)}$). There is usually less variation in the notation for these functions, so the definitions are easy to find elsewhere (e.g. in Jackson [127]).

Which of these spherical functions should be used is determined on physical grounds by the boundary conditions of the problem at hand. For example, scattered fields need to behave as outgoing spherical waves at infinity and if the incident field is for example a plane wave it needs to be well-behaved at the origin. The spherical functions we will use for this are

$$j_\ell(x) \qquad \text{Regular at the origin} \, , \tag{A.8}$$

$$\left(j_\ell(x) + \mathrm{i}n_\ell(x) = \right) h_\ell^{(1)}(x) \qquad \text{Outgoing spherical wave at infinity} \, . \tag{A.9}$$

For certain expressions (such as the Mie coefficients), it is useful to introduce the Riccati-Bessel functions, given by

$$\psi_\ell(x) = x j_\ell(x) \, , \tag{A.10}$$

$$\xi_\ell(x) = x h_\ell^{(1)}(x) \, . \tag{A.11}$$

The radial functions have useful so-called Wronski determinants [127], or Wronskians, defined by $W(f,g) = fg' - gf'$. We have

$$j_\ell(x)\left[h_\ell^{(1)}(x)\right]' - h_\ell^{(1)}(x)j_\ell'(x) = \frac{\mathrm{i}}{x^2} \, , \tag{A.12}$$

which leads to

$$\psi_\ell(x)\xi_\ell'(x) - \xi_\ell(x)\psi_\ell'(x) = \mathrm{i} \, . \tag{A.13}$$

Field basis functions

From the definitions above, we can now write the full form of the basis functions for the electric and magnetic fields. Here, the notation deviates somewhat from Jackson's book but rather follows Miljković *et al.* [154] which in turn is based on

Waterman's definitions [125]. The basis functions are given explicitly by

$$\vec{\psi}_{1\ell m} = z_\ell(kr)\vec{X}_{\ell m}(\theta, \varphi) \,,$$
$$\vec{\psi}_{2\ell m} = \mathrm{i}\frac{z_\ell(kr)}{kr}\sqrt{\ell(\ell+1)}Y_{\ell m}(\theta, \varphi)\hat{r}$$
$$+ \frac{1}{kr}\left[kr\,z_\ell(kr)\right]'\hat{r}\times\vec{X}_{\ell m}(\theta, \varphi) \,, \tag{A.14}$$

where z_ℓ is one of the spherical functions (j_ℓ or $h_\ell^{(1)}$). In the expression for $\vec{\psi}_{2\ell m}$, the prime indicates differentiation with respect to the argument in the brackets (here, it is with respect to kr). Note that the wave number in the radial functions is the wave number in the medium, $k = \sqrt{\varepsilon_r\mu_r}k_0 = \sqrt{\varepsilon_r\mu_r}\omega/c_0$, where μ_r is most often unity (for non-magnetic materials).

The choice of radial function in these basis functions will be indicated with a superscript. So $\vec{\psi}_{\tau\ell m}^{(j)}$ means regular basis functions, $z_\ell = j_\ell$ and $\vec{\psi}_{\tau\ell m}^{(h)}$ correspond to outgoing basis functions with $z_\ell = h_\ell^{(1)}$.

These basis functions fulfil the important and useful relation

$$\vec{\psi}_{\bar{\tau}\ell m} = \frac{1}{k}\nabla\times\vec{\psi}_{\tau\ell m} \,, \tag{A.15}$$

where $\tau = 1$ or 2 and $\bar{\tau}$ is the opposite of τ, i.e. $\bar{1} = 2$ and $\bar{2} = 1$. When used in the definition of the *electric field*, $\tau = 1$ are the magnetic multipoles while $\tau = 2$ are the electric ones.

Appendix B

Expansion coefficients for dipole sources

Sometimes confusion arises with regards to normalization of dipole moments. This is especially true for dipole sources placed in a homogeneous medium other than vacuum. In order to get the normalization correct for an electric dipole, for instance, we can compare the electric fields given by Eq. (2.2) in the main thesis text with those of an electric dipole in a homogeneous medium with $\mu = \mu_0 \mu_r$ and $\varepsilon = \varepsilon_0 \varepsilon_r$.

For a z-polarized electric dipole at the origin, the quantum numbers are $\ell = 1$ and $m = 0$ and in order to determine the expansion coefficient b_{210}, it is sufficient to look at the radial part of the electric fields. The radial fields from the spherical wave expansion in Eq. (2.2) are

$$
\begin{aligned}
\hat{r} \cdot \vec{E}_{\mathrm{d}}(\vec{r}) &= b_{210} \, \hat{r} \cdot \vec{\psi}_{210}^{(h)} \\
&= b_{210} \left(\mathrm{i} \frac{h_1^{(1)}(kr)}{kr} \sqrt{2} Y_{10}(\theta, \varphi) \right) \\
&= b_{210} \sqrt{\frac{3}{2\pi}} \frac{\mathrm{e}^{\mathrm{i}kr}}{k^2 r^2} \left(\frac{1}{kr} - \mathrm{i} \right) \cos\theta \,,
\end{aligned}
\tag{B.1}
$$

where it is important that $k = \sqrt{\mu_0 \mu_r \varepsilon_0 \varepsilon_r} \, \omega$ is the wavenumber in the medium.

On the other hand, the electric field in this homogeneous medium from a current distribution $\vec{j}$ is in general given by [161]

$$
\vec{E}(\vec{r}) = \mathrm{i}\omega\mu_0\mu_r \int \vec{\vec{G}}_h(\vec{r}, \vec{r}') \cdot \vec{j}(\vec{r}') \, \mathrm{d}^3 r' \,,
\tag{B.2}
$$

for any point in space (other than specifically when there are sources at $\vec{r}$, such that the fields diverge). Here, the homogeneous Green's function $\vec{\vec{G}}_h$ is explicitly given by [161]

$$
\vec{\vec{G}}_h(\vec{r}, \vec{r}') = \left(\frac{k^2 R^2 + \mathrm{i}k^2 R^2 - 1}{k^2 R^2} \mathbb{1} + \frac{3 - 3\mathrm{i}kR - k^2 R^2}{k^2 R^2} \hat{R} \otimes \hat{R} \right) \frac{\mathrm{e}^{\mathrm{i}kR}}{4\pi R} \,,
\tag{B.3}
$$

where $\vec{R} = \vec{r} - \vec{r}'$, k is the wavenumber in the medium and $\mathbb{1}$ is the unit dyad. The $\otimes$ denotes the dyad product (or vector outer product, $\vec{u} \otimes \vec{v} = \vec{u}\vec{v}^T$ for *column* vectors $\vec{u}, \vec{v}$).

If we assume an electric dipole with harmonic time-dependence at the origin oriented along the z-axis, we have $\vec{p} = p_z \hat{z}$ and the current distribution is $\vec{j}(\vec{r}') = -\mathrm{i}\omega\vec{p}\,\delta^{(3)}(\vec{r}')$. Then

$$
\vec{E}(\vec{r}) = \omega^2 \mu_0 \mu_r \, \vec{\vec{G}}_h(\vec{r}, 0) \cdot \vec{p} \,.
\tag{B.4}
$$

The radial part of this field is

$$\hat{r} \cdot \vec{E}(\vec{r}) = \omega^2 \mu_0 \mu_r \, p_z \frac{\mathrm{e}^{\mathrm{i}kr}}{2\pi kr^2} \cos\theta \left(\frac{1}{kr} - \mathrm{i} \right) . \tag{B.5}$$

Comparing the expressions in Eqns. (B.5) and (B.1), we find

$$b_{210} = \frac{k^3}{\sqrt{6\pi\varepsilon_0\varepsilon_r}} p_z . \tag{B.6}$$

Similarly, for in-plane dipoles,

$$b_{21,\pm1} = \frac{k^3}{\sqrt{6\pi\varepsilon_0\varepsilon_r}} \frac{\mp p_x + \mathrm{i}p_y}{\sqrt{2}} . \tag{B.7}$$

A similar comparison between the fields generated by a z-polarized magnetic dipole with magnetic dipole moment m_z yields

$$b_{110} = \mathrm{i}Z_r \frac{k^3}{\sqrt{6\pi}} m_z . \tag{B.8}$$

with the impedance of the medium $Z_r = \sqrt{\mu_0\mu_r/\varepsilon_0\varepsilon_r}$.

Appendix C

Multipole decomposition, arbitrary integration surface

Scattering coefficients

The total electric field outside the particle is a superposition of the incident field and the scattered field. As such it has the same general form as Equation (2.1), namely

$$\vec{E} = \vec{E}_{\text{inc}} + \vec{E}_{\text{sc}} = \sum_{\tau=1}^{2}\sum_{\ell m} a_{\tau\ell m}\vec{\psi}_{\tau\ell m}^{(j)} + b_{\tau\ell m}\vec{\psi}_{\tau\ell m}^{(h)} \; . \tag{C.1}$$

It is also possible to express the field outside a spherical surface (which will later be deformed to be arbitrary) enclosing a particle through what is called the "Extinction theorem", as [125]

$$\vec{E}(\vec{r}) = \vec{E}_{\text{inc}}(\vec{r}) + \nabla \times \int_{S'} \text{d}S' \left[\hat{n}' \times \vec{E}(\vec{r}') \right] \cdot \overleftrightarrow{G}(\vec{r}, \vec{r}')$$
$$+ \frac{\text{i}Z_r}{k}\nabla \times \nabla \times \int_{S'} \text{d}S' \left[\hat{n}' \times \vec{H}(\vec{r}') \right] \cdot \overleftrightarrow{G}(\vec{r}, \vec{r}') \; , \tag{C.2}$$

where $\hat{n}'$ denotes the unit normal vector to the surface S', Z_r is the impedance of the medium, k is the wavenumber in the medium and $\overleftrightarrow{G}(\vec{r}, \vec{r}')$ is the isotropic Green's tensor that can be separated into longitudinal and transverse parts $\overleftrightarrow{G} = \overleftrightarrow{G}_L + \overleftrightarrow{G}_T$ with $\nabla \times \overleftrightarrow{G}_L = 0$. Note that the curl operations in Equation (C.2) act with respect to the coordinate $\vec{r}$. We thus only need the transverse part for Equation (C.2), which can be expressed in terms of the ψ basis functions (Appendix A) as [132]

$$\overleftrightarrow{G}_T(\vec{r}, \vec{r}') = -\text{i}k\sum_{\tau\ell m}(-1)^m \, \vec{\psi}_{\tau\ell m}(\vec{r}) \otimes \vec{\psi}_{\tau\ell,-m}(\vec{r}') \; , \tag{C.3}$$

where the outgoing basis functions ($h_\ell^{(1)}$ radial dependence) should be used at the larger of r and r', and regular basis functions (j_ℓ radial dependence) at the smaller. In the case of the scattered field from a particle, we are interested in the fields where $r > r'$, so we use

$$\overleftrightarrow{G}_T(\vec{r}, \vec{r}') = -\text{i}k\sum_{\tau\ell m}(-1)^m \, \vec{\psi}_{\tau\ell m}^{(h)}(\vec{r}) \otimes \vec{\psi}_{\tau\ell,-m}^{(j)}(\vec{r}') \; . \tag{C.4}$$

By using the interrelation for the basis functions, Equation (A.15), namely

$$\nabla \times \vec{\psi}_{\tau\ell m} = k\vec{\psi}_{\bar{\tau}\ell m} \; , \tag{C.5}$$

we can perform the necessary curl operations in Equation (C.2). This then allows us to compare allows us to compare Equations (C.1) and (C.2) in order to identify the coefficients for the scattered fields. The magnetic scattering coefficients are

$$b_{1\ell m} = (-1)^m k^2 \int_S \mathrm{d}S \left[-\mathrm{i}\vec{\psi}_{1\ell,-m}^{(j)} \cdot (\hat{n} \times \vec{E}) + Z_r \vec{\psi}_{2\ell,-m}^{(j)} \cdot (\hat{n} \times \vec{H}) \right] , \qquad \text{(C.6)}$$

and the electric ones are

$$b_{2\ell m} = (-1)^m k^2 \int_S \mathrm{d}S \left[-\mathrm{i}\vec{\psi}_{2\ell,-m}^{(j)} \cdot (\hat{n} \times \vec{E}) + Z_r \vec{\psi}_{1\ell,-m}^{(j)} \cdot (\hat{n} \times \vec{H}) \right] . \qquad \text{(C.7)}$$

Reshaping the integration surface

The two expressions for the scattering coefficients above can be combined into

$$b_{\tau\ell m} = (-1)^m k^2 \int_S \mathrm{d}S \left[-\mathrm{i}\vec{\psi}_{\bar{\tau}\ell,-m}^{(j)} \cdot (\hat{n} \times \vec{E}) + Z_r \vec{\psi}_{\tau\ell,-m}^{(j)} \cdot (\hat{n} \times \vec{H}) \right] , \qquad \text{(C.8)}$$

and using $\vec{a} \cdot (\vec{b} \times \vec{c}) = \vec{b} \cdot (\vec{c} \times \vec{a})$, we can write it as

$$b_{\tau\ell m} = \int_S \mathrm{d}\vec{S} \cdot \vec{F} , \qquad \text{(C.9)}$$

where $\mathrm{d}\vec{S} = \hat{n}\mathrm{d}S$ and

$$\vec{F} = (-1)^m k^2 \left[-\mathrm{i}\vec{E} \times \vec{\psi}_{\bar{\tau}\ell,-m}^{(j)} + Z_r \vec{H} \times \vec{\psi}_{\tau\ell,-m}^{(j)} \right] . \qquad \text{(C.10)}$$

The divergence theorem (Gauss' theorem) tells us that

$$\int_S \mathrm{d}\vec{S} \cdot \vec{F} = \int_V \mathrm{d}V \, \nabla \cdot \vec{F} , \qquad \text{(C.11)}$$

where V is the volume enclosed by our surface S. If we can show that $\vec{F}$ is divergence free in a region without free sources, we hence know that we can deform the integration surface however we want, provided this deformation does not hit any sources. By using $\nabla \cdot (\vec{a} \times \vec{b}) = \vec{b} \cdot (\nabla \times \vec{a}) - \vec{a} \cdot (\nabla \times \vec{b})$ we write

$$\nabla \cdot \vec{F} = -\mathrm{i} \left(\vec{\psi}_{\bar{\tau}\ell,-m}^{(j)} \cdot (\nabla \times \vec{E}) - \vec{E} \cdot (\nabla \times \vec{\psi}_{\bar{\tau}\ell,-m}^{(j)}) \right)$$
$$+ Z_r \left(\vec{\psi}_{\tau\ell,-m}^{(j)} \cdot (\nabla \times \vec{H}) - \vec{H} \cdot (\nabla \times \vec{\psi}_{\tau\ell,-m}^{(j)}) \right) . \qquad \text{(C.12)}$$

In a homogeneous and isotropic region without free sources, the Maxwell equations involving curl for a harmonic time-dependence are

$$\nabla \times \vec{E} = \mathrm{i}\omega\mu_0\mu_r \vec{H} , \qquad \text{(C.13)}$$
$$\nabla \times \vec{H} = -\mathrm{i}\omega\varepsilon_0\varepsilon_r \vec{E} . \qquad \text{(C.14)}$$

Again using the curl relation of the basis functions, Equation (C.5), we get that

$$\nabla \cdot \vec{F} = \vec{\psi}_{\bar{\tau}\ell,-m}^{(j)} \cdot \vec{H} \left[\omega\mu_0\mu_r - kZ_r \right] + \vec{\psi}_{\tau\ell,-m}^{(j)} \cdot \vec{E} \left[\mathrm{i}k - \mathrm{i}Z_r\omega\varepsilon_0\varepsilon_r \right] = 0 . \qquad \text{(C.15)}$$

Appendix D

Expansion coefficients for a plane wave

The derivation of $a_{\tau\ell m}$ in terms of the basis functions $\vec{\psi}_{\tau\ell m}$ (Appendix A) is similar to the one in Bohren and Huffman [126], except the plane wave here has an arbitrary direction and polarization and the basis functions are different.

The procedure [132] is to start with the expression for a general plane wave

$$\vec{A} = \vec{E}_0 e^{i\vec{k}\cdot\vec{r}}\,, \tag{D.1}$$

and express it in a series of spherical basis functions (regular at the origin) as

$$\vec{A} = \sum_{\tau\ell m} a_{\tau\ell m} \vec{\psi}_{\tau\ell m}^{(j)}\,. \tag{D.2}$$

Then, the sought coefficients are given through

$$j_\ell(kr)a_{1\ell m} = \int d\Omega \vec{X}_{\ell m}^* \cdot \vec{A}\,, \tag{D.3}$$

and

$$j_\ell(kr)a_{2\ell m} = \int d\Omega \vec{X}_{\ell m}^* \cdot \left[i\hat{k}\times\vec{A}\right]\,. \tag{D.4}$$

One can perform these integrals [132] with the aid of the spherical wave expansion of the scalar homogeneous Green's function [127]

$$G_h(\vec{r},\vec{r}') = \frac{e^{ik|\vec{r}-\vec{r}'|}}{4\pi|\vec{r}-\vec{r}'|} = ik \sum_{\ell m} j_\ell(kr_<)h_\ell^{(1)}(kr_>)Y_{\ell m}^*(\theta',\varphi')Y_{\ell m}(\theta,\varphi)\,, \tag{D.5}$$

rewritten for a source far away. One also needs explicit expressions for the vector spherical harmonics in terms of scalar spherical harmonics, $Y_{\ell m}$, from Equation (A.2). The result is

$$a_{1\ell m} = 4\pi i^\ell \sum_{j=-1}^{1} (-1)^{m+j} Y_{\ell,-m-j}(\hat{k}) F_{\ell m}^j [\hat{e}_j^* \cdot \vec{E}_0]\,, \tag{D.6}$$

$$a_{2\ell m} = 4\pi i^{\ell+1} \sum_{j=-1}^{1} (-1)^{m+j} Y_{\ell,-m-j}(\hat{k}) F_{\ell m}^j \left[\hat{e}_j^* \cdot (\hat{k}\times\vec{E}_0)\right]\,, \tag{D.7}$$

where the sum over j runs over the 3 orthonormal ($\hat{e}_j^* \cdot \hat{e}_i = \delta_{ij}$) polarization unit vectors

$$\hat{e}_{\pm 1} = \frac{\hat{x} \mp i\hat{y}}{\sqrt{2}} \ , \qquad \hat{e}_0 = \hat{z} \ , \tag{D.8}$$

and the the spherical harmonic $Y(\hat{k})$ is interpreted as evaluated at the angles defined by the incident plane wave direction, $\hat{k}$. The numbers $F_{\ell m}^j$ are coefficients generated by the angular momentum operator of Equation (A.2). They are

$$F_{\ell m}^0 = \frac{m}{\sqrt{\ell(\ell+1)}} \ , \qquad F_{\ell m}^{\pm 1} = \sqrt{\frac{(\ell \mp m)(\ell \pm m + 1)}{2\ell(\ell+1)}} \ . \tag{D.9}$$

Although the derivation is absent, the final expressions can be found in [128].

A circularly polarized plane wave along the z-axis

The common application of Mie theory, specifically the scattering by a spherical particle in a plane wave, is a completely spherically symmetric problem. Due to this symmetry, the direction of the incident wave can be chosen freely.

In fact, the above expressions become particularly easy when the plane wave is incident along the z-axis and is circularly polarized (say along $\hat{e}_+$). Then

$$\vec{A} = E_0 \hat{e}_+ e^{ikz} \ , \tag{D.10}$$

and $\hat{k} = \hat{z}$ is defined by $\theta = 0, \varphi = 0$, and the expression for the magnetic coefficients becomes

$$a_{1\ell m} = 4\pi i^\ell (-1)^{m+1} Y_{\ell,-m-1}(0,0) \sqrt{\frac{(\ell-m)(\ell+m+1)}{2\ell(\ell+1)}} E_0 \ . \tag{D.11}$$

The spherical harmonic is (Equation (A.1))

$$Y_{\ell,-m-1}(0,0) = \sqrt{\frac{2\ell+1}{4\pi}} \sqrt{\frac{(\ell+m+1)!}{(\ell-m-1)!}} P_\ell^{-m-1}(1) \ . \tag{D.12}$$

The associated Legendre functions $P_{\ell'}^{m'}(x)$ for $x = \pm 1$ ($\theta = 0, \pi$) are only non-zero for $m' = 0$ and they are normalized such that $P_{\ell'}^0(x) = 1$ [126, 127], which means here that $-m - 1 = 0$ or that $m = -1$ is the only azimuthal number that gives a non-zero contribution. Summarizing, we have the notably more simple coefficients

$$a_{1\ell m} = i^\ell \sqrt{2\pi(2\ell+1)} E_0 \, \delta_{m,-1} \ , \tag{D.13}$$

and $\hat{k} \times \hat{e}_+ = i\hat{e}_+$ yields

$$a_{2\ell m} = -i^\ell \sqrt{2\pi(2\ell+1)} E_0 \, \delta_{m,-1} \ . \tag{D.14}$$

An x-polarized plane wave along the z-axis

Similarly, for a plane wave propagating along the z-axis with a linear polarization in the x-direction, namely

$$\vec{A} = E_0 \hat{x} e^{ikz} \,, \tag{D.15}$$

the same type of analysis as in the previous section can be made. Perhaps unsurprisingly, such a plane wave is a superposition of the two in-plane circular polarizations $\hat{e}_\pm$. In this case, only $m = \pm 1$ give non-zero contribution and we end up with

$$a_{1\ell m} = i^\ell \sqrt{2\pi(2\ell + 1)} E_0 \frac{\delta_{m,+1} + \delta_{m,-1}}{\sqrt{2}} \,, \tag{D.16}$$

and

$$a_{2\ell m} = -i^\ell \sqrt{2\pi(2\ell + 1)} E_0 \frac{\delta_{m,+1} - \delta_{m,-1}}{\sqrt{2}} \,. \tag{D.17}$$

Appendix E

Energy flow for fields in spherical multipole basis

We assume that the electromagnetic fields are written in a spherical multipole basis, in a superposition of regular and outgoing fields, according to Equation (2.1), namely that

$$\vec{E} = \vec{E}_r + \vec{E}_o \,, \tag{E.1}$$

where the regular fields are expressed in terms of the a-coefficients as

$$\vec{E}_r = \sum_{\tau\ell m} a_{\tau\ell m} \vec{\psi}^{(j)}_{\tau\ell m} \,, \qquad \vec{H}_r = -\frac{\mathrm{i}}{Z_r} \sum_{\tau\ell m} a_{\tau\ell m} \vec{\psi}^{(j)}_{\bar{\tau}\ell m} \,, \tag{E.2}$$

and the b-coefficients encode the outgoing fields with

$$\vec{E}_o = \sum_{\tau\ell m} b_{\tau\ell m} \vec{\psi}^{(h)}_{\tau\ell m} \,, \qquad \vec{H}_o = -\frac{\mathrm{i}}{Z_r} \sum_{\tau\ell m} b_{\tau\ell m} \vec{\psi}^{(h)}_{\bar{\tau}\ell m} \,, \tag{E.3}$$

where $\tau = 1$ or 2 and $\bar{\tau}$ is the opposite of τ, i.e. $\bar{1} = 2$ and $\bar{2} = 1$. Moreover, $Z_r = \sqrt{\varepsilon_0\varepsilon_r/\mu_0\mu_r}$ is the impedance of the medium. The magnetic fields have been obtained through the Maxwell equation for harmonic fields, $\nabla \times \vec{E} = \mathrm{i}\omega\mu_0\mu_r\vec{H}$.

Perhaps the most common case is that the known "source" field is the regular field (e.g. an incident plane wave) and the scattering is outgoing. However, the following treatment can be considered more general. For example, if the source is an electric dipole at the center of a sphere, this source is contained in the b-coefficients inside the sphere instead. Provided that one can find the b-coefficients outside the sphere, the energy flowing to the far-field can be obtained in the same way. While keeping this in mind, we focus on the common case of scattering by an incoming source wave, since it is easier to follow.

Given that we have some way to determine the b-coefficients outside some spherical surface enclosing all scatterers, we can find out how much energy is flowing to the far-field through integration of the Poynting vector of the outgoing field (see Section 3.3.1), namely

$$W_o = \int_S R^2 \mathrm{d}\Omega \, \vec{S}_o \cdot \hat{r} \,, \tag{E.4}$$

where the radius R of the sphere S can be arbitrary as long as there are no sources outside it. The (time-averaged) Poynting vector $\vec{S}_o$ is given by

$$\vec{S}_o = \frac{1}{2}\mathrm{Re}\left\{ \vec{E}_o \times \vec{H}_o^* \right\} \,. \tag{E.5}$$

We substitute the fields above with their spherical wave expansions to get

$$W_o = \frac{k}{2\mu_0\mu_r\omega}\text{Re}\sum_{\ell m}\sum_{\ell' m'}\int_S R^2 d\Omega \left[\text{i}\left(b_{1\ell m}\vec{\psi}_{1\ell m}^{(h)} + b_{2\ell m}\vec{\psi}_{2\ell m}^{(h)}\right)\right.$$
$$\left. \times \left(b_{1\ell' m'}^*\vec{\psi}_{2\ell' m'}^{*\,(h)} + b_{2\ell' m'}^*\vec{\psi}_{1\ell' m'}^{*\,(h)}\right)\right]\cdot\hat{r}\,, \qquad\qquad (\text{E.6})$$

where we note that the basis functions are evaluated at $r = R$. We focus on these terms one by one and use the definition of the basis functions (Appendix A). We have

- The term involving $b_{1\ell m}b_{1\ell' m'}^*$:

$$\left(\vec{\psi}_{1\ell m}^{(h)} \times \vec{\psi}_{2\ell' m'}^{*\,(h)}\right)\cdot\hat{r} = \left(\vec{\psi}_{2\ell' m'}^{*\,(h)} \times \hat{r}\right)\cdot\vec{\psi}_{1\ell m}^{(h)}$$
$$= \left(\frac{1}{kR}\xi_{\ell'}'^*(kR)(\hat{r}\times\vec{X}_{\ell' m'}^*)\times\hat{r}\right)\cdot\left(h_\ell^{(1)}(kR)\vec{X}_{\ell m}\right)$$
$$= \frac{1}{k^2 R^2}\xi_{\ell'}'^*(kR)\xi_\ell(kR)\vec{X}_{\ell' m'}^*\cdot\vec{X}_{\ell m}\,,$$

where ξ_ℓ are the Riccati-Hankel functions (Appendix A) and where we have used that $(\hat{r}\times\vec{X}_{\ell m})\times\hat{r} = \vec{X}_{\ell m}$, since $\vec{X}_{\ell m}$ has no radial component.

The two middle terms in Equation (E.6) turn out to be proportional to either $(\hat{r}\times\vec{X}_{\ell m})\cdot\vec{X}_{\ell' m'}$ or $(\hat{r}\times\vec{X}_{\ell' m'})\cdot\vec{X}_{\ell m}$ and will thus vanish upon integration on $d\Omega$ due to the orthogonality relation in Equation (A.7) and the last term will be very similar to the first. We combine the two non-zero terms and perform the integration on $d\Omega$. Using the orthogonality relation in Equation (A.5), we obtain Kroenecker deltas and the sums over ℓ' and m' collapse, leaving

$$W_o = \frac{1}{2k\mu_0\mu_r\omega}\text{Re}\sum_{\ell m}\text{i}\left[|b_{1\ell m}|^2\,\xi_\ell'^*(kR)\xi_\ell(kR) - |b_{2\ell m}|^2\xi_\ell'(kR)\xi_\ell^*(kR)\right]. \qquad (\text{E.7})$$

Now, we rewrite the ξ_ℓ's in terms of the Riccati-Bessel functions, namely

$$\xi_\ell(x) = \psi_\ell(x) - \text{i}\chi_\ell(x)\,, \qquad\qquad (\text{E.8})$$

where $\psi_\ell(x) = xj_\ell(x)$ and $\chi_\ell(x) = -xy_\ell(x)$. If any radiation is to escape to the far-field, we need to have a non-absorbing medium, so in this last step we assume that k is real. With that, we realize that both ψ_ℓ and χ_ℓ are real for real arguments [126] and we can take the real part without risk. Moreover, we can utilize a Wronskian similar to Equation (A.13) eventually leaving us with

$$W_o = \frac{1}{2k\mu_0\mu_r\omega}\sum_{\ell m}|b_{1\ell m}|^2 + |b_{2\ell m}|^2\,. \qquad\qquad (\text{E.9})$$

Bibliography

1. Bharadwaj, P., Deutsch, B. & Novotny, L. Optical Antennas. *Advances in Optics and Photonics* **1,** 438–483 (2009).

2. Agio, M. & Alù, A. *Optical antennas* ISBN: 978-1-107-01414-5 (Cambridge University Press, 2013).

3. Fredriksson, H. *et al.* Hole–Mask Colloidal Lithography. *Advanced Materials* **19,** 4297–4302 (2007).

4. Pendry, J. B. Negative Refraction Makes a Perfect Lens. *Physical Review Letters* **85,** 3966–3969 (2000).

5. Smith, D. R., Padilla, W. J., Vier, D. C., Nemat-Nasser, S. C. & Schultz, S. Composite Medium with Simultaneously Negative Permeability and Permittivity. *Physical Review Letters* **84,** 4184–4187 (2000).

6. Smith, D. R., Pendry, J. B. & Wiltshire, M. C. K. Metamaterials and Negative Refractive Index. *Science* **305,** 788–792 (2004).

7. Barnes, W. L., Dereux, A. & Ebbesen, T. W. Surface plasmon subwavelength optics. *Nature* **424,** 824–830 (2003).

8. Maier, S. A. *Plasmonics: Fundamentals and Applications* ISBN: 978-0-387-33150-8 (Springer, 2007).

9. Schuller, J. A. *et al.* Plasmonics for extreme light concentration and manipulation. *Nature Materials* **9,** 193–204 (2010).

10. Stockman, M. I. *et al.* Roadmap on plasmonics. *Journal of Optics* **20,** 043001 (2018).

11. Chen, H., Shao, L., Li, Q. & Wang, J. Gold nanorods and their plasmonic properties. *Chemical Society Reviews* **42,** 2679–2724 (2013).

12. Englebienne, P. Use of colloidal gold surface plasmon resonance peak shift to infer affinity constants from the interactions between protein antigens and antibodies specific for single or multiple epitopes. *Analyst* **123,** 1599–1603 (1998).

13. McFarland, A. D. & Van Duyne, R. P. Single Silver Nanoparticles as Real-Time Optical Sensors with Zeptomole Sensitivity. *Nano Letters* **3,** 1057–1062 (2003).

14. Anker, J. N. *et al.* Biosensing with plasmonic nanosensors. *Nature Materials* **7,** 442–453 (2008).

15. Liu, N., Tang, M. L., Hentschel, M., Giessen, H. & Alivisatos, A. P. Nanoantenna-enhanced gas sensing in a single tailored nanofocus. *Nature Materials* **10,** 631–636 (2011).

16. Kneipp, K. *et al.* Single Molecule Detection Using Surface-Enhanced Raman Scattering (SERS). *Physical Review Letters* **78,** 1667–1670 (1997).

17. Xu, H., Bjerneld, E. J., Käll, M. & Börjesson, L. Spectroscopy of Single Hemoglobin Molecules by Surface Enhanced Raman Scattering. *Physical Review Letters* **83,** 4357–4360 (1999).

18. Atwater, H. A. & Polman, A. Plasmonics for improved photovoltaic devices. *Nature Materials* **9,** 205–213 (2010).

19. Aieta, F. *et al.* Aberration-Free Ultrathin Flat Lenses and Axicons at Telecom Wavelengths Based on Plasmonic Metasurfaces. *Nano Letters* **12,** 4932–4936 (2012).

20. Ni, X., Emani, N. K., Kildishev, A. V., Boltasseva, A. & Shalaev, V. M. Broadband Light Bending with Plasmonic Nanoantennas. *Science* **335,** 427–427 (2012).

21. Yu, N. *et al.* A Broadband, Background-Free Quarter-Wave Plate Based on Plasmonic Metasurfaces. *Nano Letters* **12,** 6328–6333 (2012).

22. Karimi, E. *et al.* Generating optical orbital angular momentum at visible wavelengths using a plasmonic metasurface. *Light: Science & Applications* **3,** e167 (2014).

23. Huang, L. *et al.* Three-dimensional optical holography using a plasmonic metasurface. *Nature Communications* **4,** 2808 (2013).

24. Svedendahl, M., Verre, R. & Käll, M. Refractometric biosensing based on optical phase flips in sparse and short-range-ordered nanoplasmonic layers. *Light: Science & Applications* **3,** e220 (2014).

25. Lee, Y., Kim, S.-J., Park, H. & Lee, B. Metamaterials and Metasurfaces for Sensor Applications. *Sensors* **17** (2017).

26. Holloway, C., Kuester, E., Baker-Jarvis, J. & Kabos, P. A double negative (DNG) composite medium composed of magnetodielectric spherical particles embedded in a matrix. *IEEE Transactions on Antennas and Propagation* **51,** 2596–2603 (2003).

27. Zhao, Q., Zhou, J., Zhang, F. & Lippens, D. Mie resonance-based dielectric metamaterials. *Materials Today* **12,** 60–69 (2009).

28. Jahani, S. & Jacob, Z. All-dielectric metamaterials. *Nature Nanotechnology* **11,** 23–36 (2016).

29. Popa, B.-I. & Cummer, S. A. Compact Dielectric Particles as a Building Block for Low-Loss Magnetic Metamaterials. *Physical Review Letters* **100,** 207401 (20 2008).

30. Mie, G. Beiträge zur Optik trüber Medien, speziell kolloidaler Metallösungen. *Annalen der physik* **330,** 377–445 (1908).

31. Lewin, L. The electrical constants of a material loaded with spherical particles. *Journal of the Institution of Electrical Engineers - Part III: Radio and Communication Engineering* **94,** 65–68 (1947).

32. Fenollosa, R., Meseguer, F. & Tymczenko, M. Silicon Colloids: From Microcavities to Photonic Sponges. *Advanced Materials* **20,** 95–98 (2008).

33. Evlyukhin, A. B. *et al.* Demonstration of magnetic dipole resonances of dielectric nanospheres in the visible region. *Nano Letters* **12,** 3749–3755 (2012).

34. Evlyukhin, A. B., Reinhardt, C., Seidel, A., Luk'yanchuk, B. S. & Chichkov, B. N. Optical response features of Si-nanoparticle arrays. *Physical Review B* **82,** 045404 (2010).

35. García-Etxarri, A. *et al.* Strong magnetic response of submicron Silicon particles in the infrared. *Optics Express* **19,** 4815–4826 (2011).

36. Green, M. A. Self-consistent optical parameters of intrinsic silicon at 300 K including temperature coefficients. *Solar Energy Materials and Solar Cells* **92,** 1305–1310 (2008).

37. Staude, I. *et al.* Tailoring Directional Scattering through Magnetic and Electric Resonances in Subwavelength Silicon Nanodisks. *ACS Nano* **7,** 7824–7832 (2013).

38. Luk'yanchuk, B. S., Voshchinnikov, N. V., Paniagua-Domínguez, R. & Kuznetsov, A. I. Optimum Forward Light Scattering by Spherical and Spheroidal Dielectric Nanoparticles with High Refractive Index. *ACS Photonics* **2,** 993–999 (2015).

39. Kerker, M., Wang, D.-S. & Giles, C. L. Electromagnetic scattering by magnetic spheres. *Journal of the Optical Society of America* **73,** 765–767 (1983).

40. Geffrin, J. M. *et al.* Magnetic and electric coherence in forward- and back-scattered electromagnetic waves by a single dielectric subwavelength sphere. *Nature Communications* **3,** 1171 (2012).

41. Fu, Y. H., Kuznetsov, A. I., Miroshnichenko, A. E., Yu, Y. F. & Luk'yanchuk, B. Directional visible light scattering by silicon nanoparticles. *Nature Communications* **4,** 1527 (2013).

42. Person, S. *et al.* Demonstration of Zero Optical Backscattering from Single Nanoparticles. *Nano Letters* **13,** 1806–1809 (2013).

43. Hecht, E. *Optics, 4th Edition* ISBN: 1-292-02157-8 (Pearson, 2014).

44. Yu, N. & Capasso, F. Flat optics with designer metasurfaces. *Nature Materials* **13,** 139–150 (2014).

45. Pfeiffer, C. & Grbic, A. Metamaterial Huygens' Surfaces: Tailoring Wave Fronts with Reflectionless Sheets. *Physical Review Letters* **110,** 197401 (2013).

46. Monticone, F., Estakhri, N. M. & Alù, A. Full Control of Nanoscale Optical Transmission with a Composite Metascreen. *Physical Review Letters* **110,** 203903 (2013).

47. Decker, M. *et al.* High-Efficiency Dielectric Huygens' Surfaces. *Advanced Optical Materials* **3,** 813–820 (2015).

48. Yu, N. *et al.* Light Propagation with Phase Discontinuities: Generalized Laws of Reflection and Refraction. *Science* **334,** 333–337 (2011).

49. Lin, D., Fan, P., Hasman, E. & Brongersma, M. L. Dielectric gradient metasurface optical elements. *Science* **345,** 298–302 (2014).

50. Ding, F., Pors, A. & Bozhevolnyi, S. I. Gradient metasurfaces: a review of fundamentals and applications. *Reports on Progress in Physics* **81,** 026401 (2018).

51. Alaee, R., Filter, R., Lehr, D., Lederer, F. & Rockstuhl, C. A generalized Kerker condition for highly directive nanoantennas. *Optics Letters* **40,** 2645–2648 (2015).

52. Pors, A., Andersen, S. K. H. & Bozhevolnyi, S. I. Unidirectional scattering by nanoparticles near substrates: generalized Kerker conditions. *Optics Express* **23,** 28808–28828 (2015).

53. Liu, W. & Kivshar, Y. S. Generalized Kerker effects in nanophotonics and meta-optics. *Optics Express* **26,** 13085–13105 (2018).

54. Zograf, G. P. *et al.* Resonant Nonplasmonic Nanoparticles for Efficient Temperature-Feedback Optical Heating. *Nano Letters* **17,** 2945–2952 (2017).

55. Fattal, D., Li, J., Peng, Z., Fiorentino, M. & Beausoleil, R. G. Flat dielectric grating reflectors with focusing abilities. *Nature Photonics* **4,** 466–470 (2010).

56. Aieta, F., Kats, M. A., Genevet, P. & Capasso, F. Multiwavelength achromatic metasurfaces by dispersive phase compensation. *Science* **2,** aaa2494 (2015).

57. Zhou, Y. *et al.* Multilayer Noninteracting Dielectric Metasurfaces for Multiwavelength Metaoptics. *Nano Letters* **18,** 7529–7537 (2018).

58. Lawrence, M., Barton, D. R. & Dionne, J. A. Nonreciprocal Flat Optics with Silicon Metasurfaces. *Nano Letters* **18,** 1104–1109 (2018).

59. Chong, K. E. *et al.* Polarization-Independent Silicon Metadevices for Efficient Optical Wavefront Control. *Nano Letters* **15,** 5369–5374 (2015).

60. Ra'di, Y., Sounas, D. L. & Alù, A. Metagratings: Beyond the Limits of Graded Metasurfaces for Wave Front Control. *Physical Review Letters* **119,** 067404 (6 2017).

61. Arbabi, A., Horie, Y., Bagheri, M. & Faraon, A. Dielectric metasurfaces for complete control of phase and polarization with subwavelength spatial resolution and high transmission. *Nature Nanotechnology* **10,** 937–943 (2015).

62. Fan, W., Yan, B., Wang, Z. & Wu, L. Three-dimensional all-dielectric metamaterial solid immersion lens for subwavelength imaging at visible frequencies. *Science Advances* **2** (2016).

63. Wiecha, P. R., Lecestre, A., Mallet, N. & Larrieu, G. Pushing the limits of optical information storage using deep learning. *Nature Nanotechnology* **14,** 237–244 (2019).

64. García-Cámara, B., Gómez-Medina, R., Sáenz, J. J. & Sepúlveda, B. Sensing with magnetic dipolar resonances in semiconductor nanospheres. *Optics Express* **21,** 23007–23020 (2013).

65. Yavas, O., Svedendahl, M., Dobosz, P., Sanz, V. & Quidant, R. On-a-chip Biosensing Based on All-Dielectric Nanoresonators. *Nano Letters* **17,** 4421–4426 (2017).

66. Yavas, O., Svedendahl, M. & Quidant, R. Unravelling the Role of Electric and Magnetic Dipoles in Biosensing with Si Nanoresonators. *ACS Nano, Article ASAP*, acsnano.9b00572 (2019).

67. Krasnok, A., Caldarola, M., Bonod, N. & Alú, A. Spectroscopy and Biosensing with Optically Resonant Dielectric Nanostructures. *Advanced Optical Materials* **6,** 1701094 (2018).

68. Baranov, D. G. *et al.* All-dielectric nanophotonics: the quest for better materials and fabrication techniques. *Optica* **4,** 814–825 (2017).

69. Abbarchi, M. *et al.* Wafer Scale Formation of Monocrystalline Silicon-Based Mie Resonators via Silicon-on-Insulator Dewetting. *ACS Nano* **8,** 11181–11190 (2014).

70. Kuznetsov, A. I., Miroshnichenko, A. E., Fu, Y. H., Zhang, J. & Luk'yanchuk, B. Magnetic light. *Scientific Reports* **2,** 492 (2012).

71. Chen, H.-T., Taylor, A. J. & Yu, N. A review of metasurfaces: physics and applications. *Reports on Progress in Physics* **79,** 076401 (2016).

72. Kuznetsov, A. I., Miroshnichenko, A. E., Brongersma, M. L., Kivshar, Y. S. & Luk'yanchuk, B. Optically resonant dielectric nanostructures. *Science* **354,** aag2472 (2016).

73. Liu, W. & Kivshar, Y. S. Multipolar interference effects in nanophotonics. *Philosophical Transactions of the Royal Society A: Mathematical, Physical and Engineering Sciences* **375,** 20160317 (2017).

74. Kruk, S. & Kivshar, Y. Functional Meta-Optics and Nanophotonics Governed by Mie Resonances. *ACS Photonics* **4,** 2638–2649 (2017).

75. Staude, I. & Schilling, J. Metamaterial-inspired silicon nanophotonics. *Nature Photonics* **11,** 274–284 (2017).

76. Yang, Y., Zenin, V. A. & Bozhevolnyi, S. I. Anapole-Assisted Strong Field Enhancement in Individual All-Dielectric Nanostructures. *ACS Photonics* **5,** 1960–1966 (2018).

77. Purcell, E. M. *Spontaneous emission probabilities at radio frequencies* in *Physical Review* **69** (1946), 681–681.

78. Rolly, B., Bebey, B., Bidault, S., Stout, B. & Bonod, N. Promoting magnetic dipolar transition in trivalent lanthanide ions with lossless Mie resonances. *Physical Review B* **85,** 245432 (2012).

79. Schmidt, M. K. *et al.* Dielectric antennas - a suitable platform for controlling magnetic dipolar emission. *Optics Express* **20,** 13636–13650 (2012).

80. Baranov, D. G., Savelev, R. S., Li, S. V., Krasnok, A. E. & Alù, A. Modifying magnetic dipole spontaneous emission with nanophotonic structures. *Laser & Photonics Reviews* **11,** 1600268 (2017).

81. Novotny, L. & Hecht, B. *Principles of Nano-Optics* ISBN: 978-0-521-83224-3 (Cambridge University Press, 2006).

82. Zambrana-Puyalto, X. & Bonod, N. Purcell factor of spherical Mie resonators. *Physical Review B* **91,** 195422 (19 2015).

83. Stout, B., Devilez, A., Rolly, B. & Bonod, N. Multipole methods for nanoantennas design: applications to Yagi-Uda configurations. *Journal of the Optical Society of America B* **28,** 1213–1223 (2011).

84. Rolly, B., Stout, B. & Bonod, N. Boosting the directivity of optical antennas with magnetic and electric dipolar resonant particles. *Optics Express* **20,** 20376–20386 (2012).

85. Albella, P. *et al.* Low-Loss Electric and Magnetic Field-Enhanced Spectroscopy with Subwavelength Silicon Dimers. *The Journal of Physical Chemistry C* **117,** 13573–13584 (2013).

86. Bakker, R. M. *et al.* Magnetic and Electric Hotspots with Silicon Nanodimers. *Nano Letters* **15,** 2137–2142 (2015).

87. Bouchet, D. *et al.* Enhancement and Inhibition of Spontaneous Photon Emission by Resonant Silicon Nanoantennas. *Physical Review Applied* **6,** 064016 (6 2016).

88. Sanz-Paz, M. *et al.* Enhancing Magnetic Light Emission with All-Dielectric Optical Nanoantennas. *Nano Letters* **18,** 3481–3487 (2018).

89. Caldarola, M. *et al.* Non-plasmonic nanoantennas for surface enhanced spectroscopies with ultra-low heat conversion. *Nature Communications* **6,** 7915 (2015).

90. Staude, I. *et al.* Shaping Photoluminescence Spectra with Magnetoelectric Resonances in All-Dielectric Nanoparticles. *ACS Photonics* **2,** 172–177 (2015).

91. Regmi, R. *et al.* All-Dielectric Silicon Nanogap Antennas To Enhance the Fluorescence of Single Molecules. *Nano Letters* **16,** 5143–5151 (2016).

92. Li, J., Verellen, N. & Van Dorpe, P. Enhancing Magnetic Dipole Emission by a Nano-Doughnut-Shaped Silicon Disk. *ACS Photonics* **4,** 1893–1898 (2017).

93. Rutckaia, V. *et al.* Quantum Dot Emission Driven by Mie Resonances in Silicon Nanostructures. *Nano Letters* **17,** 6886–6892 (2017).

94. Capretti, A., Lesage, A. & Gregorkiewicz, T. Integrating Quantum Dots and Dielectric Mie Resonators: A Hierarchical Metamaterial Inheriting the Best of Both. *ACS Photonics* **4,** 2187–2196 (2017).

95. Greffet, J. J. *et al.* Diamond particles as nanoantennas for nitrogen-vacancy color centers. *arXiv:1107.0502* (2011).

96. Zalogina, A. S. *et al.* Purcell effect in active diamond nanoantennas. *Nanoscale* **10,** 8721–8727 (2018).

97. Canham, L. *Handbook of porous silicon* (Springer, 2014).

98. Staude, I., Pertsch, T. & Kivshar, Y. S. All-Dielectric Resonant Meta-Optics Lightens up. *ACS Photonics, Article ASAP,* acsphotonics.8b01326 (2019).

99. Baranov, D. G., Wersäll, M., Cuadra, J., Antosiewicz, T. J. & Shegai, T. Novel Nanostructures and Materials for Strong Light–Matter Interactions. *ACS Photonics* **5,** 24–42 (2018).

100. Burns, J. A., Lamy, P. L. & Soter, S. Radiation forces on small particles in the solar system. *Icarus* **40,** 1 –48. ISSN: 0019-1035 (1979).

101. Ashkin, A. Acceleration and Trapping of Particles by Radiation Pressure. *Physical Review Letters* **24,** 156–159 (1970).

102. Ashkin, A., Dziedzic, J. M., Bjorkholm, J. E. & Chu, S. Observation of a single-beam gradient force optical trap for dielectric particles. *Optics Letters* **11,** 288–290 (1986).

103. Finer, J. T., Simmons, R. M. & Spudich, J. A. Single myosin molecule mechanics: piconewton forces and nanometre steps. *Nature* **368,** 113–119 (1994).

104. Neuman, K. C. & Nagy, A. Single-molecule force spectroscopy: optical tweezers, magnetic tweezers and atomic force microscopy. *Nature Methods* **5,** 491–505 (2008).

105. Wang, M., Yin, H., Landick, R., Gelles, J. & Block, S. Stretching DNA with optical tweezers. *Biophysical Journal* **72,** 1335 –1346 (1997).

106. Fazal, F. M. & Block, S. M. Optical tweezers study life under tension. *Nature Photonics* **5,** 318–321 (2011).

107. Chu, S., Bjorkholm, J. E., Ashkin, A. & Cable, A. Experimental Observation of Optically Trapped Atoms. *Physical Review Letters* **57,** 314–317 (1986).

108. Toyabe, S., Sagawa, T., Ueda, M., Muneyuki, E. & Sano, M. Experimental demonstration of information-to-energy conversion and validation of the generalized Jarzynski equality. *Nature Physics* **6,** 988–992 (2010).

109. Blickle, V. & Bechinger, C. Realization of a micrometre-sized stochastic heat engine. *Nature Physics* **8,** 143–146 (2012).

110. Svoboda, K. & Block, S. M. Optical trapping of metallic Rayleigh particles. *Optics Letters* **19,** 930–932 (1994).

111. Lehmuskero, A., Johansson, P., Rubinsztein-Dunlop, H., Tong, L. & Käll, M. Laser Trapping of Colloidal Metal Nanoparticles. *ACS Nano* **9,** 3453–3469 (2015).

112. Ni, W., Ba, H., Lutich, A. A., Jäckel, F. & Feldmann, J. Enhancing Single-Nanoparticle Surface-Chemistry by Plasmonic Overheating in an Optical Trap. *Nano Letters* **12,** 4647–4650 (2012).

113. Šiler, M., Ježek, J., Jákl, P., Pilát, Z. & Zemánek, P. Direct measurement of the temperature profile close to an optically trapped absorbing particle. *Optics Letters* **41,** 870–873 (2016).

114. Andrén, D. *et al.* Probing Photothermal Effects on Optically Trapped Gold Nanorods by Simultaneous Plasmon Spectroscopy and Brownian Dynamics Analysis. *ACS Nano* **11,** 10053–10061 (2017).

115. Šípová, H., Shao, L., Odebo Länk, N., Andrén, D. & Käll, M. Photothermal DNA Release from Laser-Tweezed Individual Gold Nanomotors Driven by Photon Angular Momentum. *ACS Photonics* **5,** 2168–2175 (2018).

116. Rings, D., Schachoff, R., Selmke, M., Cichos, F. & Kroy, K. Hot Brownian Motion. *Physical Review Letters* **105,** 090604 (9 2010).

117. Andres-Arroyo, A., Wang, F., Toe, W. J. & Reece, P. Intrinsic heating in optically trapped Au nanoparticles measured by dark-field spectroscopy. *Biomedical Optics Express* **6,** 3646–3654 (2015).

118. Andres-Arroyo, A., Gupta, B., Wang, F., Gooding, J. J. & Reece, P. J. Optical Manipulation and Spectroscopy Of Silicon Nanoparticles Exhibiting Dielectric Resonances. *Nano Letters* **16,** 1903–1910 (2016).

119. Shilkin, D. A., Lyubin, E. V., Shcherbakov, M. R., Lapine, M. & Fedyanin, A. A. Directional Optical Sorting of Silicon Nanoparticles. *ACS Photonics* **4,** 2312–2319 (2017).

120. Zaza, C. *et al.* Size-Selective Optical Printing of Silicon Nanoparticles through Their Dipolar Magnetic Resonance. *ACS Photonics* **0,** *Article ASAP*, acsphotonics.8b01619 (2019).

121. Lehmuskero, A., Ogier, R., Gschneidtner, T., Johansson, P. & Käll, M. Ultrafast Spinning of Gold Nanoparticles in Water Using Circularly Polarized Light. *Nano Letters* **13,** 3129–3134 (2013).

122. Li, M., Lohmüller, T. & Feldmann, J. Optical Injection of Gold Nanoparticles into Living Cells. *Nano Letters* **15,** 770–775 (2015).

123. Nieto-Vesperinas, M., Gomez-Medina, R. & Saenz, J. J. Angle-suppressed scattering and optical forces on submicrometer dielectric particles. *Journal of the Optical Society of America A* **28,** 54–60 (2011).

124. Sáenz, J. J. Laser tractor beams. *Nature Photonics* **5,** 514–515 (2011).

125. Waterman, P. C. Symmetry, Unitarity, and Geometry in Electromagnetic Scattering. *Physical Review D* **3,** 825–839 (1971).

126. Bohren, C. F. & Huffman, D. R. *Absorption and scattering of light by small particles* ISBN: 0-471-05772-X (John Wiley & Sons, 1983).

127. Jackson, J. D. *Classical electrodynamics* ISBN: 047130932X (Wiley, 1999).

128. Johansson, P., Xu, H. & Käll, M. Surface-enhanced Raman scattering and fluorescence near metal nanoparticles. *Physical Review B* **72,** 035427 (2005).

129. Paniagua-Domínguez, R. *et al.* Generalized Brewster effect in dielectric metasurfaces. *Nature Communications* **7,** 10362 (2016).

130. García-Cámara, B., de la Osa, R. A., Saiz, J. M., González, F. & Moreno, F. Directionality in scattering by nanoparticles: Kerker's null-scattering conditions revisited. *Optics Letters* **36,** 728–730 (2011).

131. Grahn, P, Shevchenko, A & Kaivola, M. Electromagnetic multipole theory for optical nanomaterials. *New Journal of Physics* **14,** 093033 (2012).

132. Johansson, P. *Unpublished notes*.

133. Miroshnichenko, A. E. *et al.* Nonradiating anapole modes in dielectric nanoparticles. *Nature Communications* **6,** 8069 (2015).

134. Alaee, R., Rockstuhl, C. & Fernandez-Corbaton, I. An electromagnetic multipole expansion beyond the long-wavelength approximation. *Optics Communications* **407,** 17 –21 (2018).

135. Dubovik, V. & Tugushev, V. Toroid moments in electrodynamics and solid-state physics. *Physics Reports* **187,** 145 –202 (1990).

136. Savinov, V., Fedotov, V. A. & Zheludev, N. I. Toroidal dipolar excitation and macroscopic electromagnetic properties of metamaterials. *Physical Review B* **89,** 205112 (2014).

137. Baranov, D. G., Verre, R., Karpinski, P. & Käll, M. Anapole-Enhanced Intrinsic Raman Scattering from Silicon Nanodisks. *ACS Photonics* **5,** 2730–2736 (2018).

138. Kane, Y. Numerical solution of initial boundary value problems involving Maxwell's equations in isotropic media. *IEEE Transactions on Antennas and Propagation* **14,** 302–307 (1966).

139. Oskooi, A. F. *et al.* Meep: A flexible free-software package for electromagnetic simulations by the FDTD method. *Computer Physics Communications* **181,** 687 –702 (2010).

140. Rumpf, R. *EE 5337: Computational Electromagnetics* The University of Texas at El Paso. http://emlab.utep.edu/ee5390cem.htm.

141. Lumerical. *FDTD Solutions, Knowledge base* https://kb.lumerical.com/index.html.

142. Taflove, A. & Hagness, S. C. *Computational electrodynamics: the finite-difference time-domain method* ISBN: 1-58053-832-0 (Artech house, 2005).

143. Gedney, S. D. Introduction to the Finite-Difference Time-Domain (FDTD) Method for Electromagnetics. *Synthesis Lectures on Computational Electromagnetics* **6,** 1–250 (2011).

144. Bedeaux, D. & Vlieger, J. *Optical properties of surfaces* ISBN: 1860944507 (World Scientific, 2004).

145. Mendoza-Galván, A. *et al.* Optical response of supported gold nanodisks. *Optics Express* **19,** 12093–12107 (2011).

146. Svedendahl, M., Johansson, P. & Käll, M. Complete Light Annihilation in an Ultrathin Layer of Gold Nanoparticles. *Nano Letters* **13,** 3053–3058 (2013).

147. Ogier, R., Fang, Y., Käll, M. & Svedendahl, M. Near-Complete Photon Spin Selectivity in a Metasurface of Anisotropic Plasmonic Antennas. *Physical Review X* **5,** 041019 (2015).

148. Lazzari, R. & Simonsen, I. GranFilm: a software for calculating thin-layer dielectric properties and Fresnel coefficients. *Thin Solid Films* **419,** 124–136 (2002).

149. Svedendahl, M. & Käll, M. Fano Interference between Localized Plasmons and Interface Reflections. *ACS Nano* **6,** 7533–7539 (2012).

150. Thongrattanasiri, S., Koppens, F. H. L. & García de Abajo, F. J. Complete Optical Absorption in Periodically Patterned Graphene. *Physical Review Letters* **108,** 047401 (2012).

151. Jones, P. H., Maragò, O. M. & Volpe, G. *Optical tweezers* ISBN: 978-1-107-05116-4 (Cambridge University Press, 2015).

152. Pfeifer, R. N. C., Nieminen, T. A., Heckenberg, N. R. & Rubinsztein-Dunlop, H. *Colloquium*: Momentum of an electromagnetic wave in dielectric media. *Reviews of Modern Physics* **79,** 1197–1216 (2007).

153. Barton, J. P., Alexander, D. R. & Schaub, S. A. Theoretical determination of net radiation force and torque for a spherical particle illuminated by a focused laser beam. *Journal of Applied Physics* **66,** 4594–4602 (1989).

154. Miljković, V. D., Pakizeh, T., Sepulveda, B., Johansson, P. & Käll, M. Optical Forces in Plasmonic Nanoparticle Dimers. *The Journal of Physical Chemistry C* **114,** 7472–7479 (2010).

155. Richards, B & Wolf, E. Electromagnetic diffraction in optical systems, II. Structure of the image field in an aplanatic system. *Proceedings of the Royal Society of London. Series A. Mathematical and Physical Sciences* **253,** 358–379 (1959).

156. Nieto-Vesperinas, M., Sáenz, J. J., Gómez-Medina, R. & Chantada, L. Optical forces on small magnetodielectric particles. *Optics Express* **18,** 11428–11443 (2010).

157. Doyle, W. T. Optical properties of a suspension of metal spheres. *Physical Review B* **39,** 9852–9858 (1989).

158. Scully, M. O. & Zubairy, M. S. *Quantum optics* 1997.

159. Koenderink, A. F. On the use of Purcell factors for plasmon antennas. *Optics Letters* **35,** 4208–4210 (2010).

160. Bernal Arango, F., Coenen, T. & Koenderink, A. F. Underpinning Hybridization Intuition for Complex Nanoantennas by Magnetoelectric Quadrupolar Polarizability Retrieval. *ACS Photonics* **1,** 444–453 (2014).

161. Johansson, P. Electromagnetic Green's function for layered systems: Applications to nanohole interactions in thin metal films. *Physical Review B* **83,** 195408 (2011).